

Fourier transform rheology of complex, filled rubber materials

Zur Erlangung des akademischen Grades eines

DOKTORS DER NATURWISSENSCHAFTEN

(Dr. rer. nat.)

von der KIT-Fakultät für Chemie und Biowissenschaften

des Karlsruher Instituts für Technologie (KIT)

genehmigte

DISSERTATION

von

Lukas Schwab

aus

Landau in der Pfalz

KIT-Dekan: Prof. Dr. Willem Klopper

Referent: Prof. Dr. Manfred Wilhelm

Korreferent: Prof. Dr. Dr. Christian Friedrich

Tag der mündlichen Prüfung: 12.02.2016

Diese Arbeit wurde in der Zeit vom 01. Dezember 2011 bis zum 05. Januar 2016 am Institut für Technische Chemie und Polymerchemie des Karlsruher Instituts für Technologie (KIT) unter Anleitung von Prof. Dr. Manfred Wilhelm durchgeführt. Diese Arbeit basiert auf Vorarbeiten aus der von mir erstellten Diplomarbeit [121]. Teile dieser Arbeit wurden bereits in einem von mir verfassten [157] und einem von mir mitverfassten [21] Artikel in Fachzeitschriften veröffentlicht. Daher unterliegen einige der in dieser Arbeit verwendeten Graphiken dem Urheberrecht des jeweiligen Verlages und wurden mit dessen Einverständnis verwendet.

Hiermit versichere ich, dass ich die von mir vorgelegte Arbeit selbständig verfasst habe, dass ich die verwendeten Quellen und Hilfsmittel vollständig angegeben und die Stellen der Arbeit, die anderen Werken im Wortlaut oder dem Sinn nach entnommen sind, entsprechend kenntlich gemacht habe.

Karlsruhe, den 21. März 2016

Lukas Schwab

Nomenclature

| | |
|-----------------------------|--|
| α | Parameter for temperature dependence of χ , Eq. 2.31 |
| β | Parameter for temperature dependence of χ |
| γ | Strain, Eq. 2.2 |
| γ_0 | Strain amplitude, Eq. 2.5 |
| γ_{DP} | Strain of viscous dash pot in Maxwell model, Eq. 2.8 |
| γ_{\min} | Minimum strain amplitude for the onset of the scaling law $I_{3/1} \propto \gamma_0^2$ |
| γ_S | Strain of elastic spring in Maxwell model, Eq. 2.8 |
| $\dot{\gamma}$ | Shear rate, time derivative of the strain |
| δ | Loss angle, Eq. 2.10 |
| ε_0 | Dynamic strain in tension experiments |
| ε_{AB} | Interaction energy in copolymers between monomer A and monomer B according to the Flory-Huggins theory, Eq. 2.30 |
| $\varepsilon_{\text{stat}}$ | Static strain in tension experiments |
| η | Viscosity, Eq. 2.4 |
| η_0 | Viscosity of unfilled polymer |
| $[\eta]$ | Intrinsic viscosity |
| Θ | Angular deflection |
| θ | Scattering angle |
| λ | Deformation ratio, $\lambda = \varepsilon_0 + 1$ |
| ν_{AC} | Frequency of electrical current |
| ν | Frequency, $\nu = \omega/2\pi$ |
| $\rho(\vec{r})$ | Difference in electron density in a block copolymer |

| | |
|---------------------|---|
| σ | Stress, Eq. 2.1 |
| σ_0 | Extrapolated DC-conductivity |
| σ_{AC} | AC-conductivity |
| σ_{DP} | Stress of viscous dash pot in Maxwell model, Eq. 2.9 |
| σ_{\min} | Fatigue limit, stress value below which no fatigue is observed |
| σ_P | Standard deviation of parameter P |
| σ_S | Stress of elastic spring in Maxwell model, Eq. 2.9 |
| τ | (Longest) relaxation time of a polymer, determined by the cross over of G' and G'' |
| Φ | Volume fraction of monomer A in a diblock copolymer |
| ϕ | Volume fraction of carbon black in compounds |
| ϕ_c | Percolation threshold, Eq. 2.24 |
| ϕ_{eff} | Effective filler volume fraction |
| ϕ_m | Maximum packing fraction of a filler in a compound, Eqs. 6.3 and 6.4 |
| χ | Flory-Huggins interaction parameter, Eq. 2.30 |
| ω | Angular frequency |
| A | Area of a geometry in a rheological experiment |
| A | Coefficient in the mathematical description of $I_{3/1}(\gamma_0)$ in the SAOS and the MAOS regime, Eq. 2.23. |
| $A(\vec{q})$ | Scattering amplitude |
| a_i | Coefficients of Taylor series expression of G^* , Eq. 2.14 |
| a_T | Horizontal shift factor for master curve according to the WLF-equation (Eq. 5.7) |
| b | Proportionality factor in fit for conductivity as function of filler volume fraction, Eq. 6.1 |
| b_i | Coefficients in power series for the expression of $\eta(\phi)$, Eq. 2.26. |
| b_T | Vertical shift factor for master curve according to the WLF-equation (Eq. 5.7) |
| BCC | A phase morphology of body centered cubic oriented spheres in a block copolymer |
| C_1, C_2 | Empirical parameters for WLF-equation (Eq. 5.7) |

Nomenclature

| | |
|-------|--|
| c | Critical exponent for the change of a material property close to the percolation threshold ϕ_c , Eq. 2.24 |
| CB | Carbon black |
| COAN | Oil adsorption number of crushed sample |
| CPS | A phase morphology of close packed spheres in a block copolymer |
| d | Scaling exponent in the mathematical description of $I_{3/1}(\gamma_0 = 0.32, \phi)$, Eq. 6.2 |
| DCBS | <i>N,N</i> -dicyclohexyl-2-benzothiazole sulfenamide |
| DIB | 1,3-Diisopropenyl benzene |
| DIS | Disordered phase morphology in a block copolymer |
| DRI | Differential refractive index |
| DSC | Dynamic scanning calorimetry |
| E_0 | Young's modulus of an elastomer at small deformations |
| E' | Elastic part of Young's modulus |
| E'' | Viscous part of Young's modulus |
| E^* | Complex Young's modulus |
| EPDM | Ethylene-propylene-diene-monomer rubber |
| F | Force |
| f | Shape factor, Eq. 2.28 |
| FCC | face centered cubic symmetry |
| FT | Fourier Transform |
| G | Shear modulus, Eq. 2.3 |
| G' | Storage modulus, Eq. 2.12 |
| G'' | Loss modulus, Eq. 2.12 |
| G^* | Complex shear modulus, Eqs. 2.11 and 2.12 |
| GYR | A bicontinuous, cubic (gyroid) phase morphology in a block copolymer |
| h | Distance between the two geometry parts in a rheological measurement |

| | |
|--------------|--|
| HEX | A phase morphology of hexagonal oriented cylinders in a block copolymer |
| $I_{n/1}$ | Relative intensity of the n th higher harmonic contribution, Eq. 2.18 |
| $I(\vec{q})$ | Scattering intensity |
| $I(\nu)$ | Frequency dependent intensity of a FT magnitude spectrum |
| k_B | Boltzmann's constant, $k_B = 1.380\,66 \cdot 10^{-23} \text{ J K}^{-1}$ |
| L | Long period |
| l | Length of monomer unit |
| LAM | A lamellar phase morphology in a block copolymer |
| LAOS | Large amplitude oscillatory shear |
| LVE | Linear viscoelastic |
| M | Torque |
| M_0 | Minimum torque in curing curve |
| M_{max} | Maximum torque in curing curve |
| M^* | Complex torque |
| M_n | Number averaged molecular weight |
| M_w | Weight averaged molecular weight |
| m | Scaling exponent of $I_{3/1}(\gamma_0)$ for CB filled rubber |
| MAOS | Medium amplitude oscillatory shear |
| MPEB | 1,3-Di[1-(methylphenyl)ethenyl] benzene |
| N | Degree of polymerization |
| N_f | Fatigue life, i.e. number of cycles until material failure occurs by fatigue |
| n | Architecture of block copolymer, $(A-B)_n$ |
| NR | Natural rubber |
| NSA | Nitrogen surface area of carbon black |
| NVE | Nonlinear viscoelastic |
| OAN | Oil adsorption number of a carbon black grade |

| | |
|-----------------------|--|
| P | Material parameter, which is influenced by the filler volume fraction, such as electrical conductivity or shear modulus |
| $P(\vec{q})$ | Form factor |
| PDI | Polydispersity index |
| PDMS | Polydimethylsiloxane |
| PEB | 1,3-Bis(1-phenylethenyl) benzene |
| phr | Parts per hundred parts of rubber by weight |
| PI | Polyisoprene |
| PS | Polystyrene |
| Q | Q-parameter, Eq. 2.21 |
| Q_0 | Intrinsic nonlinearity, Eq. 2.22 |
| \vec{q} | Scattering vector |
| R | R Ratio, relation between minimum to maximum deformation/stress during a cycle of a fatigue measurements |
| $\langle R_G \rangle$ | Radius of gyration |
| \vec{r} | Position vector |
| $S(\vec{q})$ | Structure factor |
| SAOS | Small amplitude oscillatory shear |
| SAXS | Small angle X-Ray scattering |
| SBR | Styrene-butadiene rubber, E-SBR is made by radical emulsion polymerization and S-SBR made by anionic solution polymerization |
| <i>s</i> -BuLi | <i>sec</i> -butyllithium |
| SEC | Size exclusion chromatography, also called gel permeation chromatography |
| SIS | Poly(styrene- <i>b</i> -isoprene- <i>b</i> -styrene) |
| $\tan \delta$ | Loss tangent, Eq. 2.13 |
| TPE | Thermoplastic elastomer, see Section 2.3 |
| T | Temperature |

| | |
|------------------|--|
| T_g | Glass transition temperature of a polymer |
| T_{ref} | Reference temperature of a master curve, Eq. 5.7 |
| t | Time |
| t_0 | Time from the start of the measurement to the torque minimum in a curing curve |
| t_{90} | Time in curing curve until the torque increased by 90% of the maximum increase |
| TBBS | <i>N-tert</i> -Butylbenzothiazole-2-sulphenamide |
| TEM | Transmission electron microscopy |
| U_{RMS} | Root mean square of the AC voltage |
| X | Amplification factor, Eq. 2.29 |
| x | Deflection of a body |
| x_m | Critical value in the mathematical description of $I_{3/1}(\gamma_0 = 0.32, \phi)$, Eq. 6.2 |
| Z | Number of nearest neighbor monomer units to a copolymer configuration cell in the Flory Huggins theory, Eq. 2.30 |

Zusammenfassung

Kautschuk ist eine wichtige Materialklasse mit einem breiten Anwendungsgebiet, von Reifen über Dämpfer und Dichtungen bis hin zu elektrischen Isolationen. Im Fokus der hier vorgestellten Arbeit lagen zwei wichtige Arten dieser Materialklasse: rußgefüllte Kautschuke und thermoplastische Elastomere.

Thermoplastische Elastomere bestehen aus einem thermoplastischen und einem elastomeren Polymer, die phasensepariert sind. In dieser Arbeit wurden Poly(styrol-*b*-isopren-*b*-stryrol) Copolymere als Modellsysteme ausgewählt. Zunächst wurden diese mittels anionischer Polymerisation synthetisiert. Dazu wurden drei verschiedene Syntheserouten getestet: die Verwendung eines bifunktionellen Initiators, die Kopplung von lebenden Diblockanionen und die sequentielle Polymerisation. Die sequentielle Polymerisation erwies sich dabei als beste Möglichkeit zum Erreichen eines hohen Anteils an Triblockcopolymeren. Das rheologische Verhalten der so hergestellten Proben wurde mit Hilfe der Fourier-Transformations-Rheologie (FT-Rheologie) untersucht. Dabei zeigte sich, dass die relative Intensität des dritten harmonischen Obertons, $I_{3/1}$, in einem weiten Bereich unabhängig von der Anregungsfrequenz und der Messtemperatur ist.

Als zweites System wurde rußgefüllter Styrol-Butadien-Kautschuk (SBR) untersucht. Dabei konzentrierte sich die Arbeit zunächst auf den Einfluss des Füllstoffgehaltes und der Partikelform des Rußes auf die nichtlinearen, viskoelastischen Eigenschaften des unvernetzten Kautschuks. Es zeigte sich, dass der Einfluss des Rußes auf $I_{3/1}$ bei mittleren Scheramplituden ($0.1 < \gamma_0 < 0.5$) am stärksten ausgeprägt ist. Bei einer Scheramplitude von $\gamma_0 = 0.32$ führte die Erhöhung des Volumenanteils an Ruß der Sorte N339 von $\phi = 0$ auf $\phi = 0.215$ zu einem zehnmal höheren Wert von $I_{3/1}$. Der Einfluss der Partikelform auf $I_{3/1}$ konnte auf die unterschiedliche Struktur der Rußpartikel zurückgeführt werden. Je größer die Oberfläche des Rußpartikels, desto mehr Wechselwirkungen zwischen Polymer und Füllstoff sind möglich und desto höher war der nichtlineare

Anteil an der Schubspannung. Neben dem unvernetzten Kautschuk wurden auch der Verlauf des Vulkanisationsprozesses, sowie die vernetzten Kautschuke mit Hilfe der FT-Rheologie untersucht. Bei den vernetzten Kautschuken zeigte sich eine hohe Abhängigkeit des rheologischen Verhaltens von der mechanischen Beanspruchung während der Vulkanisation. Je höher diese Beanspruchung war, desto geringer war der linear viskoelastische Bereich des untersuchten Kautschukes.

Ein weiteres Forschungsgebiet dieser Arbeit war die Verwendung der FT-Rheologie bei der Untersuchung der Langzeitstabilität von vulkanisierten Kautschuken. Die dauerhafte mechanische Beanspruchung der Proben bei gleichzeitiger thermischer Alterung führte zu einem kontinuierlichen Anstieg von $I_{3/1}$ bei gleichzeitiger Abnahme des Speichermoduls G' .

In der hier vorliegenden Arbeit werden die vielfältigen Möglichkeiten der FT-Rheologie bei der mechanischen Charakterisierung von komplexen, gefüllten und ungefüllten Kautschuken aufgezeigt. Basierend auf diesen Erkenntnissen ergeben sich zahlreiche neue zukünftige Anwendungsgebiete dieser Methode im Bereich der Kautschuktechnologie.

Contents

| | |
|--|-------------|
| Nomenclature | II |
| Zusammenfassung | VIII |
| 1. Motivation | 1 |
| 2. Theory | 5 |
| 2.1. Shear rheology | 5 |
| 2.1.1. The fundamental principles of oscillatory shear rheology | 5 |
| 2.1.2. Fourier transform rheology | 10 |
| 2.2. Filled elastomers | 15 |
| 2.2.1. Carbon black as filler in rubber materials | 15 |
| 2.2.2. Composition and structure of rubber compounds | 17 |
| 2.2.3. Rheology of filled rubber under LAOS | 19 |
| 2.3. Thermoplastic Elastomers and phase separation in block copolymers | 25 |
| 3. Performance of a rubber rheometer under LAOS | 28 |
| 3.1. Comparison with open gap geometry rheometer | 31 |
| 3.2. Investigation of the peak in $I_{3/1}$ at small strain amplitudes | 34 |
| 3.3. Comparison of the V50 with an RPA 2000 rheometer | 40 |
| 3.3.1. Experimental approach | 40 |
| 3.3.2. Results | 41 |
| 4. Synthesis of thermoplastic elastomers | 46 |
| 4.1. Choice of model system | 46 |

| | |
|--|------------|
| 4.2. Anionic polymerization of triblock copolymers | 47 |
| 4.2.1. General considerations | 48 |
| 4.2.2. Synthetic pathways used for the anionic synthesis of triblock copolymers | 49 |
| 5. FT rheology of thermoplastic elastomers | 58 |
| 5.1. Samples | 58 |
| 5.2. Rheological measurements | 63 |
| 6. FT-Rheology of carbon black filled solution SBR | 69 |
| 6.1. Influence of carbon black on unvulcanized rubber | 69 |
| 6.1.1. Measurement of the electrical percolation threshold by dielectric relaxation spectroscopy | 71 |
| 6.1.2. Curing tests | 73 |
| 6.1.3. SAOS frequency tests | 74 |
| 6.1.4. LAOS strain amplitude tests | 79 |
| 6.2. Influence of carbon black on vulcanized rubber | 92 |
| 6.2.1. Rheology during the isothermal vulcanization | 94 |
| 6.2.2. FT-Rheology of vulcanized rubber | 98 |
| 7. Evaluation of FT-Rheology for the quantification of fatigue in filled rubber materials | 103 |
| 7.1. Theoretical background | 103 |
| 7.2. Samples | 106 |
| 7.3. Results | 107 |
| 7.3.1. Tension measurements | 107 |
| 7.3.2. Torsion measurements | 110 |
| 8. Conclusion and Outlook | 114 |
| Bibliography | 122 |
| Appendix | 133 |

| | |
|--|------------|
| A. Experimental part | 134 |
| A.1. Anionic polymerization | 134 |
| A.1.1. Reactants and solvents | 134 |
| A.1.2. Synthesis of poly(styrene- <i>b</i> -isoprene- <i>b</i> -styrene) triblock copolymers | 135 |
| A.2. Instrumentation | 136 |
| B. Samples and analytical results | 139 |
| B.1. Commercial thermoplastic polymers | 139 |
| B.2. Thermoplastic elastomers | 140 |
| B.3. Unvulcanized, carbon black filled S-SBR | 145 |
| B.4. Vulcanized, carbon black filled S-SBR for fatigue measurements | 145 |
| B.5. Unvulcanized, carbon black filled E-SBR | 146 |
| Publications | 149 |

1. Motivation

After the invention of sulfur based vulcanization by Charles Goodyear [1] and its technical improvement by Thomas Hancock [2] in the 1840s, rubber materials became important industrial products. In the early times of rubber products, natural rubber (NR) was the only rubber material used. It consists of polyisoprene (PI) with a very high content (99.9%) of the 1,4-*cis*-isomer [3]. As a product of natural origin, NR contains several other ingredients (up to 6 wt%) such as proteins, phospholipids and inorganic salts, which have a great impact on the properties of the rubber material [3]. The exact composition of a NR latex depends on many factors including the clone of the rubber tree *Hevea brasiliensis* (today approximately 50 different clones are used), the climate, soil, and seasonal effects [4]. This resulted in the introduction of a classification system for NR grades, the so called technical grades, which is mainly based on their oil resistance and mechanical properties, e.g. hardness, compression set and tensile strength [5].

Synthetic rubbers became important during World War II when the demand for rubber products, especially tires, increased and the supply of NR was limited [6, Chapter 1.2]. Since this time, the demand for rubbers, both synthetic and natural, increased. Today, more than 28 Mt rubber is produced per year (2014), of which 40% is NR [7].

Today, vulcanized rubber products are used in a wide range of applications including tires, conveyor belts, shock absorbers, pipes, hoses and electrical insulation [8]. For most applications, the addition of additives is needed to achieve the necessary properties. The addition of solid fillers has a large impact on the mechanical behavior as they are able to reinforce rubbers, i.e. to improve their viscoelastic and failure properties [9]. Fillers, such as carbon black (hereinafter: CB) and silica, with a high surface area (usually above $10 \text{ m}^2 \text{ g}^{-1}$) are able to increase the Mooney viscosity, the hardness [10, Chapter 3], and improve the stretch to failure [11]. The origin of this improvement is attributed to interactions between the filler particles and the surrounding rubber polymer [12].

The mechanical behavior of rubber materials is an important parameter for their processing and their eventual application. The mechanical properties of heterogeneous rubber compounds received less attention in the literature compared to those of thermoplastics [13] and many issues are still unresolved [12, 14, 15]. The complex structure of vulcanized rubber materials results in nonlinear viscoelastic behavior already at low strain amplitudes, especially relative to unfilled polymers [16]. These nonlinear mechanical effects do not only have a great influence on the processing behavior [12], but also on the final application.

In tire industry, the rolling resistance, wet grip and wear resistance of a tire are often plotted in a so called ‘Magic Triangle’ [17], which is illustrated in Fig. 1.1 for two different fillers. The three properties are all influenced by the filler used in the respective compound and often the improvement of one of the properties results in the curtailing of the other two [17, pp. 95–96][18, p. 921]. Facing high energy prices, new state regulations require labels with information on rolling resistance of tires to encourage fuel economy [19, 20]. This is only one reason why further improvement of the used compounds is needed in rubber technology. This calls for the use of sophisticated and precise methods to determine the physical properties and structural change in rubber materials [21]. Despite this fact, instruments with simplistic testing approaches such as the Mooney rheometer are still common today and remain the accepted instruments for standard testing in the rubber industry [16].

Large amplitude oscillatory shear (LAOS) was found to be a versatile tool for determining the nonlinear viscoelastic properties of soft matter and complex fluids. Numerous approaches for the analysis of these measurements were proposed, including Fourier transform rheology (FT-Rheology) [22]. FT-Rheology was already applied for the investigation of many different complex systems such as dispersions [23], nanocomposites [24] or polymer melts with different topologies [25]. The high stiffness of filled rubber compounds requires the use of special rubber rheometers with closed, pressurized geometries for reliable measurements at high dynamic strain amplitudes [12, 26]. Leblanc

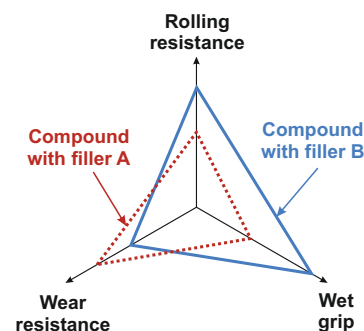


Figure 1.1.: ‘Magic triangle’ of the three most important properties in tire technology: rolling resistance, wet grip, and wear resistance. All of these properties are influenced by the added filler, and often one property can only be improved, when the others are curtailed.

et al. [27] used a modified rubber rheometer for the investigation of rubber compounds with FT-Rheology and proved the utility of these technique in numerous studies (e.g. [12, 28–30]).

In this work, the effect of CB on the nonlinear properties of styrene-butadiene rubber (SBR) was studied with a rubber rheometer that has the capability for FT-Rheology built in. By systematically varying the content and particle size of the filler, the influence of the polymer-filler interface was investigated as well as the influence of external material parameters like the measurement temperature on compounds relevant for the tire industry (Section 6.1). These compounds included a sulfur based vulcanization system, which enabled the measurement of the nonlinear rheological properties during the vulcanization process as well as the probing of the vulcanized samples by FT-Rheology, in addition to measurements on the unvulcanized material (Section 6.2). Thus the influence of the covalent polymer network could be studied in detail.

In order to perform reliable measurements in the nonlinear viscoelastic regime, the capability of the instrument used must be confirmed. This was done by comparing the results on various polymer melts measured on the rubber rheometer with results from a high-end open gap rheometer, which is typically used for nonlinear measurements. This enabled a comparison on the special features of the instrument design (Chapter 3). Additionally, the results on CB filled, unvulcanized SBR were compared with those already published by Leblanc et al. [12], who measured the same samples on a different rubber rheometer (Section 3.3).

The previously mentioned investigations are all focused on the properties of the compounds under shear flow, which is important to understand the processing behavior of CB filled rubbers. The long term stability is also an important issue for rubber materials. Therefore, the influence of mechanical aging, the so called fatigue life, of these material was also studied with FT-Rheology to test the usefulness of this highly sensitive technique for stability measurements (Chapter 7).

Rubber compounds necessitate a covalent network structure for end applications. This structure prevents the flow of the material and causes the high elasticity of the materials. At the same time, this covalent structure hinders the reuse and recycling of rubber products and is thus responsible for a growing volume of rubber waste [8]. This encouraged research on alternative materials that combine the advantages of rubber (high elasticity, large elongation at break, long fatigue life) with those of thermoplastic polymer melts (good processability, easy to recycle). This research

eventually led to the development of so called thermoplastic elastomers (TPEs) in the 1960s [31]. TPEs are complex, heterogeneous materials and consist of a thermoplastic and a rubber phase. They are already widely used commercially, but are still not fully understood [32].

Therefore, the nonlinear mechanical properties of these materials were also studied in this work (Chapter 5). Triblock copolymers of styrene and isoprene were used as a TPE model system, especially due to its structural similarity to CB filled elastomers. The TPEs were synthesized by anionic polymerization techniques and the synthesis was optimized (Chapter 4).

In the following, first the theoretical background of FT-Rheology, TPEs and the rheology of filled rubbers is given, including a short discussion on the structure of CB and filled rubber compounds (Chapter 2). Then the rubber rheometer used in this work is evaluated for nonlinear measurements and some features special to rubber rheometers are examined (Chapter 3). Afterwards, the choice of the TPE model polymer, poly(styrene-*b*-isoprene-*b*-styrene) (SIS), is explained (Section 4.1). In Section 4.2 the different approaches used for the anionic polymerization of these model systems and the corresponding synthetic results are discussed. This is followed by the rheological characterization of these TPE materials under LAOS in Chapter 5. The rheological characterization of CB filled SBR is the focus of the second half of this study. In Chapter 6 unvulcanized samples are investigated (Section 6.1), followed by the study of the vulcanization process and the vulcanized products with FT-Rheology (Section 6.2). Eventually, the application of FT-Rheology for research on the longterm stability of vulcanized rubber materials was tested in Chapter 7.

2. Theory

2.1. Shear rheology

2.1.1. The fundamental principles of oscillatory shear rheology

In this section a short introduction to the basic concepts of shear rheology is given and the important variables that are used in the following chapters are introduced. A more detailed elaboration can be found in rheological textbooks, e.g. [33–37].

Rheology is the science of flow and deformation of matter with a focus on the fundamental relations between force and deformation in materials under simple deformations [35, p. 1].

An example of a shear deformation is depicted in Fig. 2.1, where the sample is located between two parallel plates with area A . A force F is applied on the upper plate tangential to its surface, which

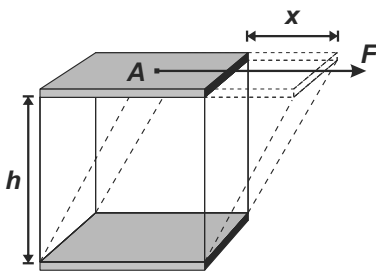


Figure 2.1.: Two plate model of a shear deformation. A force F is applied on the upper geometry part with the area A , which results in a deflection x (or vice versa) of the upper geometry part in a distance h from the lower geometry part.

results in a deflection x . Both, the deflection x and the force F do not only depend on the sample material, they are also influenced by the type of geometry used for the measurement, such as cone and plate, parallel plate or Couette geometry (Fig. 2.2), and its dimensions (e.g. diameter, distance between upper and lower geometry). Hence rheological measurements are usually interpreted in terms of two variables that are independent of the geometry, the stress σ and the strain γ . The stress σ (Eq. 2.1) is defined as the applied force normalized to the area of the geometry part where the torque is measured, A , and the strain (Eq. 2.2) is defined as the deflection x divided by the

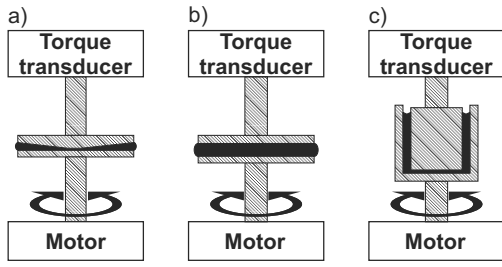


Figure 2.2.: Scheme of different geometries in a strain controlled rheometer: a) Cone-plate, b) parallel plate, c) Couette geometry. The lower part of the geometry is connected to the motor that applies a defined deformation to the sample material (black) and the upper part of the geometry is connected to a torque transducer, which measures the corresponding mechanical response.

distance between the upper and the lower geometry parts, h .

$$\sigma \equiv \frac{F}{A} \quad (2.1)$$

$$\gamma \equiv \frac{x}{h} \quad (2.2)$$

In rotational measurements, two set-ups are commonly used: controlled stress and controlled strain instruments [35, Chapter 8]. In a controlled stress instrument, a torque M is applied on one part of the geometry and the measured quantity is the deflection Θ of the same geometry part due to the applied torque. They are often limited in their response at short times, because the measurements can be influenced by the inertia of the rotor, if this influence is not corrected [35, Chapter 8]. In the second set-up, a controlled strain (also called controlled rate) instrument, a defined deflection is applied on one part (usually the lower) of the geometry and the resulting torque is measured on the other geometry part. Strain-controlled instruments have the advantage that the measured sample response, the torque M , is mechanically decoupled from the applied torque of the motor needed for the defined deflection [38]. This makes them better suited for measurements of nonlinear mechanical material properties. The nonlinear viscoelastic behavior of the investigated materials is the main focus of this work and consequently only controlled strain instruments are used in this study.

A constitutive equation is the fundamental mathematical relation between stress and strain for a sample material [35, Chapter 1]. Two simple constitutive models are Hooke's law (Eq. 2.3) for ideal elastic materials and Newton's law (Eq. 2.4) for ideal viscous materials.

$$\text{ideal elastic materials:} \quad \sigma = G\gamma \quad (2.3)$$

$$\text{ideal viscous materials:} \quad \sigma = \eta\dot{\gamma} \quad (2.4)$$

According to Hooke's law, the shear stress σ of ideal elastic materials is directly proportional to the shear strain γ . The constant of proportionality, G , is a material constant and is called the shear modulus. For ideal viscous materials such as water, Newton's law states that the stress is proportional to the time derivative of γ , the shear rate $\dot{\gamma}$. The constant of proportionality is the viscosity η .

In oscillatory measurements, a sinusoidal strain $\gamma(t)$ is applied with strain amplitude γ_0 and angular frequency ω_1 (Eq. 2.5). The resulting stress is in-phase with the strain for ideal elastic materials but $\pi/2$ out-of-phase for materials that follow Newton's law (Eqs. 2.6 and 2.7 respectively).

$$\gamma(t) = \gamma_0 \sin(\omega_1 t) \quad (2.5)$$

$$\text{ideal elastic materials: } \sigma(t) = G\gamma(t) = G\gamma_0 \sin(\omega_1 t) \quad (2.6)$$

$$\text{ideal viscous materials: } \sigma(t) = \eta\dot{\gamma}(t) = \eta\gamma_0\omega_1 \cos(\omega_1 t) = \eta\gamma_0\omega_1 \sin(\omega_1 t + \pi/2) \quad (2.7)$$

Most materials (e.g. polymer melts, dispersions) are neither ideal elastic nor ideal viscous and show intermediate behavior instead. Therefore, such materials are called viscoelastic.

In rheological models the ideal elastic contribution is depicted as a spring with Hookean behavior and the ideal viscous contribution is depicted as a dash pot with Newtonian behavior. Viscoelastic behavior is often described by a combination of these and other elements. The rheological behavior of polymer melts at high temperatures for example is often approximated by the so called Maxwell model, which is depicted in Fig. 2.3. In this model, a Hookean spring and a Newtonian dash pot are connected in series. The total strain applied on the material, γ , (Eq. 2.8) is given as the sum of the strains in both elements, the spring (γ_S) and the dash pot (γ_{DP}). The stress in the spring and the dash pot (σ_S and σ_{DP} ,

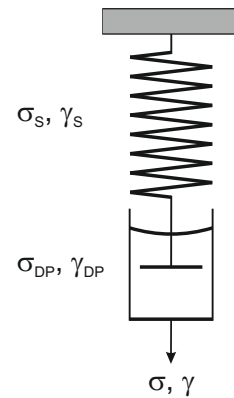


Figure 2.3.: Scheme of Maxwell model with elastic spring and viscous dash pot combined in line

respectively) is the same and equal to the total stress, σ (Eq. 2.9).

$$\gamma = \gamma_S + \gamma_{DP} \quad (2.8)$$

$$\sigma = \sigma_S = \sigma_{DP} \quad (2.9)$$

Under oscillatory shear, this results in a stress, which is also sinusoidal, but out-of-phase to the strain by a phase angle δ (loss angle) between 0 and $\pi/2$ (Eq. 2.9). The resulting shear modulus G^* is complex and a function of the angular frequency ω_1 . The stress can be separated into a part in-phase with the excitation that reflects the elastic properties (the energy stored in the material) and a part $\pi/2$ out-of-phase that reflects the viscous properties (the energy dissipated in the material) as can be seen from Eq. 2.11. The complex shear modulus can be separated in an elastic modulus (also called storage modulus) G' and a viscous modulus (also called loss modulus) G'' (Eq. 2.12). The relation between viscous and elastic modulus is expressed as the loss tangent, $\tan \delta$ (Eq. 2.13).

$$\sigma(t) = G^* \gamma_0 \sin(\omega_1 t + \delta) \quad 0 < \delta < \pi/2 \quad (2.10)$$

$$\begin{aligned} \sigma(t) &= G^* \gamma_0 \sin(\omega_1 t)(\cos \delta) + G^* \gamma_0 \cos(\omega_1 t) \sin(\delta) \\ &= G' \gamma_0 \sin(\omega_1 t) + G'' \gamma_0 \cos(\omega_1 t) \end{aligned} \quad (2.11)$$

$$G^* = G' + iG'' \quad (2.12)$$

$$\frac{G''}{G'} = \frac{G^* \sin(\delta)}{G^* \cos(\delta)} = \tan \delta \quad (2.13)$$

Up to this point, the shear modulus was treated as a complex material function that depends only on the applied frequency and the temperature T . This is only true, under the assumption that the applied deformation does not change the structure of the material under investigation. There are many kinds of possible structural changes caused by large deformations, including the orientation of chains in polymer melts [22], the orientation of anisotropic particles in a suspension [22][35, Chapter 10.3], the deformation of droplets in emulsions [23], and the break up of agglomerates in dispersions [35, Chapter 10.7] to name a few. In these and other cases, the shear modulus is a function of the applied strain amplitude. The absolute value of the complex shear modulus, $|G^*|$, of a linear polystyrene melt (PS-1) with a (weight averaged) molecular weight $M_w = 292 \text{ kg mol}^{-1}$

as a function of γ_0 is shown in Fig. 2.4. At low strain amplitudes, $|G^*|$ is independent of γ_0 . With

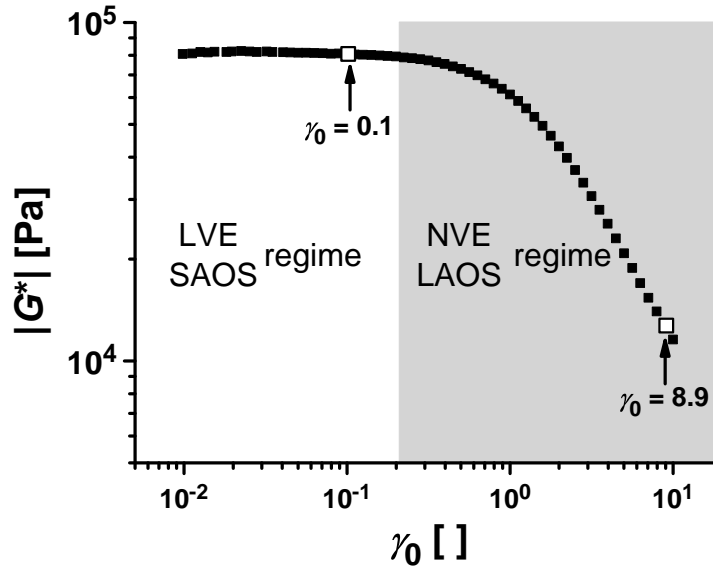


Figure 2.4.: Absolute value of the complex modulus, $|G^*|$, of a linear polystyrene melt (PS-1, $M_w = 292 \text{ kg mol}^{-1}$, $T = 190 \text{ }^\circ\text{C}$, $\omega_1/2\pi = 0.5 \text{ Hz}$, measured on the V50 rubber rheometer) as a function of strain amplitude γ_0 . In the linear viscoelastic (LVE) or small amplitude oscillatory shear (SAOS) regime the modulus is independent of the strain amplitude. In the nonlinear viscoelastic (NVE) or large amplitude oscillatory shear (LAOS) regime the modulus is decreasing with increasing γ_0 . The marked strain amplitudes are used in Fig. 2.5.

increasing strain amplitude, the modulus starts to decrease due to the orientation and stretching of the polymer chains caused by the mechanical force [39]. The amplitude range in which $|G^*|$ is constant is called the linear viscoelastic (LVE) or small amplitude oscillatory shear (SAOS) regime. The range in which $|G^*|$ is a function of γ_0 is called nonlinear viscoelastic (NVE) or large amplitude oscillatory shear (LAOS) regime. In most cases, there is no clear border between the LVE and the NVE regime. Instead, the influence of the shear amplitude is continuously increasing, i.e. the definition of the constant value of $|G^*|$ in the LVE regime depends on the users decision based on the instruments sensitivity (for example a deviation of less than 10 % from the mean value).

In order to analyze the nonlinear stress in the LAOS regime, many different mathematical approaches have been developed [22], such as the analysis of the strain amplitude dependent storage and loss modulus ($G'(\gamma_0)$ and $G''(\gamma_0)$, respectively) [12, 40, 41], Fourier transform rheology (FT-Rheology) [42], Lissajous figures, characteristic functions [43], stress decomposition [44], Chebyshev polynomial representation [45], and quarter cycle integration [28] to name some of the most important ones. The following chapter will explain one of these methods, FT-Rheology, which was used

in this work, in more detail.

2.1.2. Fourier transform rheology

In order to analyze the nonlinear rheological behavior of a material, an analytical expression for the strain amplitude dependence of the modulus is assumed. Material functions of polymer melts, such as the steady shear viscosity or the shear modulus G^* , often show a power law dependence on the deformation in the NVE regime and generally G^* can be described by a Taylor series (Eq. 2.14) [42, 46], where the coefficients a_i are all complex numbers.

$$\text{general case:} \quad G^* = a_0 + a_1\gamma + a_2\gamma^2 + a_3\gamma^3 + a_4\gamma^4 + \dots \quad (2.14)$$

$$\text{isotropic material, oscillatory shear:} \quad G^* = a_0 + a_2\gamma^2 + a_4\gamma^4 + \dots \quad (2.15)$$

all a_i are complex numbers

In the special case of isotropic materials and for oscillatory shear excitation, the complex modulus is independent of the direction of the deformation, i.e. G^* is only a function of the absolute value of γ . Thus the mathematical expression for the modulus Eq. 2.14 can be simplified to Eq. 2.15, because this assumption is already fulfilled by a Taylor series with even multiples of the strain γ only [47]. Consequently, the shear stress in measurements with oscillatory excitation can usually be described by a function of the shear amplitude and the odd multiples of the angular frequency ω_1 (Eq. 2.16).

$$\begin{aligned} \sigma &= G^* \gamma_0 e^{i(\omega_1 t)} \quad \text{with } \gamma = \gamma_0 e^{i(\omega_1 t)} \\ &= \left[a_0 + a_2 \gamma_0^2 + a_4 \gamma_0^4 + \dots \right] \gamma_0 e^{i(\omega_1 t)} \\ &= \left[a_0 + a_2 \gamma_0^2 e^{i(2\omega_1 t)} + a_4 \gamma_0^4 e^{i(4\omega_1 t)} + \dots \right] \gamma_0 e^{i(\omega_1 t)} \\ &= a_0 \gamma_0 e^{i(\omega_1 t)} + a_2 \gamma_0^3 e^{i(3\omega_1 t)} + a_4 \gamma_0^5 e^{i(5\omega_1 t)} + \dots \end{aligned} \quad (2.16)$$

The Fourier transform of this function results in two spectra: a magnitude spectrum and a corresponding phase spectrum [48]. The frequency dependent intensity of the magnitude spectrum, $I(\nu)$, depends on the sample size, the geometry used, and so on. In order to compare results of

different experiments, different samples, and to increase the relative reproducibility of the measurements, the intensity of the spectra $I(\nu)$ is normalized to the intensity at the excitation frequency $\nu_1 = \omega_1/2\pi$, $I(\nu_1)$ [22]. Thus, a spectrum of relative intensities is obtained. This spectrum has a peak at ν_1 , which is called the fundamental peak, but also peaks at the odd multiples of ν_1 , the higher harmonic contributions, which indicate the nonlinear viscoelastic behavior. For anisotropic samples, Eq. 2.14 has to be used instead of Eq. 2.15 to express G^* in Eq. 2.16 and the stress is a function of the even multiples of ν_1 in these cases, too. The same is true, if an asymmetric excitation is used, such as tension or compression experiments with an additional static strain (see Chapter 7), and if the excitation is not perfectly sinusoidal.

Based on Eq. 2.16, the intensities of the peaks should follow the relation given below:

$$I(n\nu_1) \propto \gamma_0^n \quad (2.17)$$

For FT-Rheology, the peak intensities of the magnitude spectra and/or their corresponding phases are, either directly or in form of derived parameters, correlated with structural parameters of the material under investigation. Van Dusschoten and Wilhelm [49] improved the sensitivity of torque transducers by applying an on-the-fly averaging algorithm, the so called oversampling, a technique well known from NMR-spectroscopy, in a way that FT-Rheology became a readily available tool for analyzing the nonlinear rheological behavior of complex fluids such as dispersions [50], foams [51], colloidal gels [52], or nanocomposites [24]. Leblanc and coworkers [12, 27–30] also used FT-Rheology for the investigation of various filled and unfilled elastomers (see Section 2.2.3). Most of these works used the relative intensity of the higher harmonic contribution at three times the excitation frequency ν_1 , $I_{3/1}$ (Eq. 2.18), because this is the most intense higher harmonic contribution at a given strain amplitude and excitation frequency.

$$I_{3/1} \equiv \frac{I(3\nu_1)}{I(\nu_1)} \quad (2.18)$$

The technique of FT-Rheology is further illustrated in Fig. 2.5 for the example of PS-1. In oscillatory shear experiments a sinusoidal strain $\gamma(t) = \gamma_0 \sin(\nu_1 t)$, with the strain amplitude γ_0 and the excitation frequency ν_1 , is applied on the sample. When the strain amplitude is within the SAOS

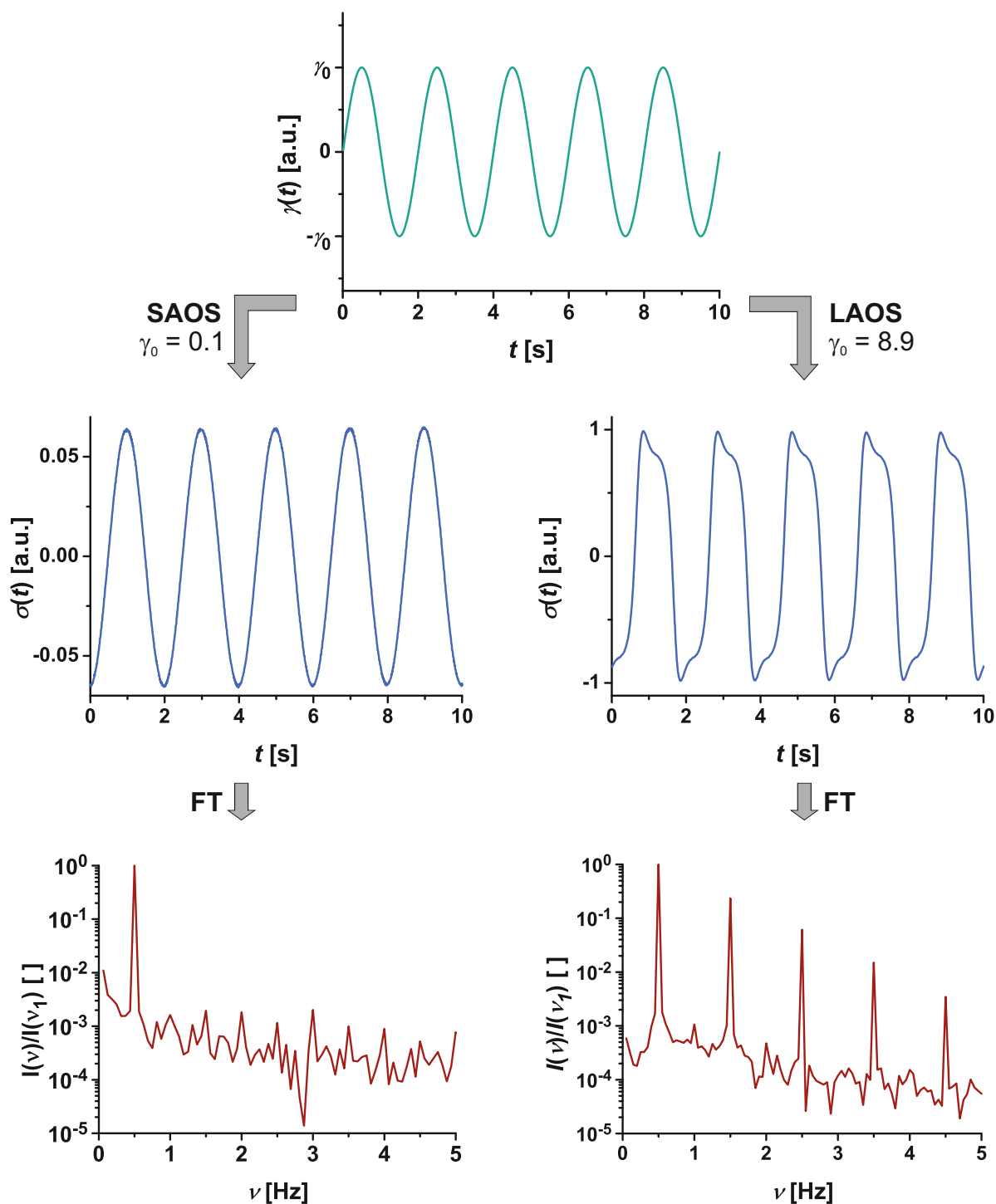


Figure 2.5.: Principle of FT-Rheology: A sinusoidal strain is applied on the sample with excitation frequency ν_1 and strain amplitude γ_0 . If small amplitude oscillatory shear (SAOS) is used, i.e. γ_0 is within the LVE regime ($\gamma_0 = 0.1$), the resulting stress signal is a single sinusoidal one (except for noise) and the (normalized) magnitude spectra of its Fourier transform has a peak at ν_1 only. When large amplitude oscillatory shear (LAOS) is applied instead ($\gamma_0 = 8.9$), the stress signal is periodically but not a single sinusoidal signal and the magnitude spectra reveals additional contributions at the odd multiples of ν_1 . (PS-1, $T = 190^\circ\text{C}$, $\nu_1 = 0.5$ Hz, measured on the V50 rubber rheometer)

regime ($\gamma_0 = 0.1$, Fig. 2.4), the resulting stress signal is also sinusoidal and the magnitude spectrum of its Fourier transform has only one peak at the excitation frequency ($\nu_1 = 0.5$ Hz). If the applied strain amplitude is within the LAOS regime ($\gamma_0 = 8.9$), the resulting stress response is still periodic but not a single sinusoidal signal. In the magnitude spectrum, additional peaks are visible at odd multiples of the excitation frequency, i.e. the higher harmonic contributions. The intensities in the presented spectra are already normalized to the respective intensity at the excitation frequency.

In order to interpret and quantify the nonlinear viscoelastic behavior of the material under shear deformation, nonlinear variables such as the relative third higher harmonic contribution $I_{3/1}$ are extracted from the magnitude spectra and plotted as a function of strain amplitude.

Figure 2.6 shows $I_{3/1}(\gamma_0)$ for PS-1, which displays some common features of $I_{3/1}(\gamma_0)$ found in measurements of various polymeric materials.

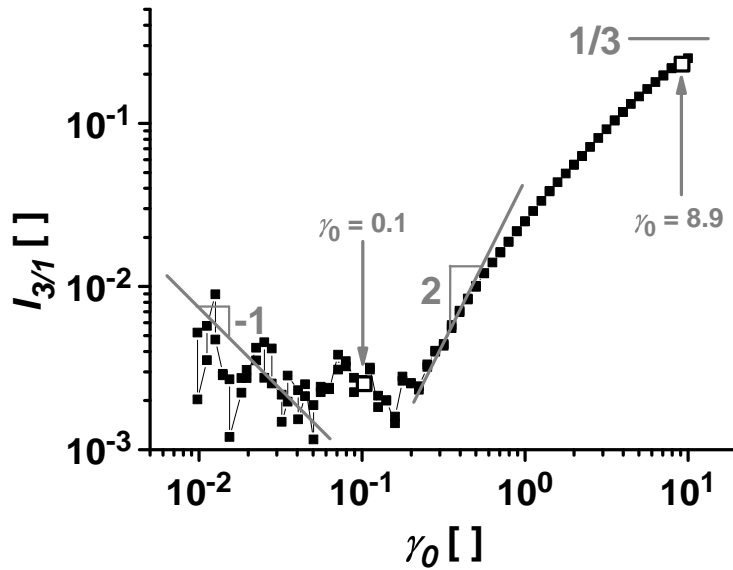


Figure 2.6.: Relative third higher harmonic contribution $I_{3/1}(\gamma_0)$ of a polystyrene melt (PS-1), the marked points correspond to the amplitudes used in Fig. 2.5. At small amplitudes $I_{3/1}$ is proportional to γ_0^{-1} , at medium amplitudes proportional to γ_0^2 and at very high amplitudes it approaches a value of $1/3$ ($T = 190^\circ\text{C}$, $\omega_1/2\pi = 0.5$ Hz, measured with the V50 rubber rheometer).

At small strain amplitudes, i.e. in the SAOS regime, the nonlinear contributions are below the sensitivity limit of the torque transducer and only the value of the fundamental peak is measurable. Therefore, the magnitude of $I(3\nu_1)$ is governed by instrumental noise, which has a constant average value and hence is independent of the strain amplitude, whereas $I(\nu_1) \propto \gamma_0$ according to Eq. 2.17.

As a result, $I_{3/1}$ is decreasing with a slope of -1 in the double logarithmic plot (Eq. 2.19).

$$\text{SAOS: } I_{3/1} = \frac{I(3\nu_1)}{I(\nu_1)} \propto \frac{\text{constant}}{\gamma_0^1} \propto \gamma_0^{-1} \quad (2.19)$$

At intermediate strain amplitudes, when $I(3\nu_1)$ is within the measurable range of the transducer, $I_{3/1}$ is according to Eq. 2.17 proportional to γ_0^2 (Eq. 2.20). The range of strain amplitudes, for which the latter scaling law is valid, is called the medium amplitude oscillatory shear (MAOS) [53].

$$\text{MAOS: } I_{3/1} \propto \frac{\gamma_0^3}{\gamma_0^1} = \gamma_0^2 \quad (2.20)$$

Hyun and Wilhelm [53] defined two new parameters, the Q-parameter (Q , Eq. 2.21) and the intrinsic nonlinearity Q_0 (Eq. 2.22), both derived from $I_{3/1}$. The latter one is independent of the strain amplitude and only a function of the excitation frequency.

$$Q \equiv \frac{I_{3/1}}{\gamma_0^2} \quad (2.21)$$

$$Q_0 \equiv \lim_{\gamma_0 \rightarrow 0} Q = \lim_{\gamma_0 \rightarrow 0} \frac{I_{3/1}}{\gamma_0^2} \quad (2.22)$$

As a consequence of the described scaling laws in the SAOS and the MAOS regime, $I_{3/1}(\gamma_0)$ can be described by Eq. 2.23.

$$I_{3/1}(\gamma_0) = A\gamma_0^{-1} + Q_0\gamma_0^2 \quad (2.23)$$

At very high γ_0 , for shear thinning materials such as most polymer melts, maximum shear thinning behavior is reached when the viscosity is inverse proportional to the absolute value of the shear rate. In this case the stress signal is a step function [42] and $I_{3/1}$ should reach a maximum value of $1/3$ at very high amplitudes.

These are features expected for all shear thinning materials, when the modulus can be described by Eq. 2.15. For more applications of FT-Rheology see the review article of Hyun et al. [22] and the references mentioned therein.

2.2. Filled elastomers

2.2.1. Carbon black as filler in rubber materials

Carbon black (hereinafter: CB) is one of the most prominent fillers used for elastomers [54, 55]. It consists of elemental carbon in form of small particles with colloidal size [56]. In contrast to the term “soot”, which refers to the unwanted byproduct of the incomplete combustion or pyrolysis of materials that contain carbon, “carbon black” is produced under controlled conditions for commercial applications [57]. Two main chemical processes are used for the production of CB: the thermal-oxidative decomposition (i.e. incomplete combustion) and the thermal decomposition of hydrocarbons of various sources such as natural gas, coal tar and crude oil [56, Chapter 1]. By the choice of the production process and the conditions used, the size of the gained CB can be controlled [56, Chapter 1]. Today, the most important production process for CB is the so called furnace black process, which uses thermal-oxidative decomposition of liquid hydrocarbons [57, 58]. In this process, the feedstock is typically coal tar oils and crude oil fractions with a high content of aromatic hydrocarbons [58]. This feedstock is preheated and then sprayed into a flame of natural gas, together with preheated process air. Thereby, spherical particles of carbon (called primary particles) with a diameter of 10 nm to 90 nm are initially formed, which partially fuse together in the further course of the process [10, Chapter 4.1] and finally form complex three-dimensional structures, the so called aggregates [59, 60]. In a certain distance from the feedstock injection point, water is injected into the reactor to quench the produced particles, to stop further reactions and to cool down the smoke [56, Chapter 1]. The mixture of process air and CB is then filtered and the solid particles are recovered [10, Chapter 4.1]. More details of this and other processes used for the production of CB can be found in the literature, e.g. [10, 56]. The basic structure of a CB aggregate is shown in Fig. 2.7.

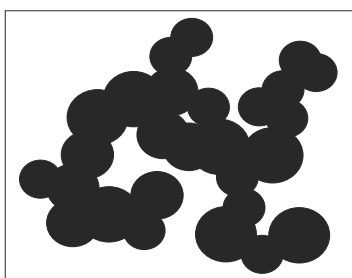


Figure 2.7.: Structure of a CB aggregate. The aggregate has a typical diameter of 100 nm to 300 nm and consist of many spherical primary particles fused together during the production process.

The produced CB is composed of more than 97 % elemental carbon [57] in graphite modification, i.e. the carbon atoms have an sp^2 -hybridization. In contrast to the crystalline graphite, only a few layers of carbon (usually up to five layers) are stacked in an ordered structure and thus the single crystalline areas are generally smaller than 2 nm [58]. The hydrogen to carbon ratio of CB is below 0.05 [57]. On the surface of the CB, functional groups containing oxygen are found, such as hydroxyl and carboxyl groups, lactones, ketones and quinones [10, Chapter 4.1], but if no special after-treatment is done, the oxygen content in CB aggregates is below 1 % [57].

The aggregates are the smallest dispersible unit of CB [56, Chapter 3.3] and they have a typical diameter of 100 nm to 300 nm [10, Chapter 4.1]. The specific surface area of CB is usually measured by nitrogen adsorption using the BET (Brunauer, Emmet and Teller) method and given as nitrogen surface areas, NSA, in $m^2 g^{-1}$ [61]. The adsorption of iodine is also used as measure of the CB surface area [62]. The complex three-dimensional structure of the aggregates is measured by the adsorption of a low viscous fluid, such as dibutylphthalate or epoxidized sunflower oils, and the result (in mL oil per 100 g of CB) is given (depending on the details of the measurement) as oil adsorption number (OAN) [63] or oil adsorption number of the crushed sample (COAN) [64].

Based on these different physical properties, CB is classified into different grades by a standard of ASTM International [65]. The grade name consists of four characters: a letter and three numbers. The letter indicates the influence of the CB on the curing kinetics of a rubber compound. Grades with the letter “N” have no significant influence on the curing rate, in contrast to grades with the letter “S”, which reduce the curing rate when mixed into a rubber [65]. The second character, i.e. the first number of the grade name, is related to the NSA. The lower the digit, the higher the NSA, for example the number “1” corresponds to an NSA of $121 m^2 g^{-1}$ to $150 m^2 g^{-1}$, whereas the number “6” indicates an NSA of $33 m^2 g^{-1}$ to $39 m^2 g^{-1}$ [65]. According to the standard classification, the last two characters are “arbitrarily assigned digits”, i.e. depending on the measured OAN and the iodine adsorption number various different groups are defined with no direct relation between the value of the numbers in the grade name and the actually measured adsorption numbers [65].

Physical interactions between the CB aggregates during storage can cause the flocculation of these aggregates and larger CB agglomerates are formed, which can be broken down into aggregates by mechanical forces [56, Chapter 3.3].

2.2.2. Composition and structure of rubber compounds

A rubber is a polymer with a glass transition temperature T_g below 0 °C that is or can be chemically cross-linked [6, Chapter 2.1]. After cross-linking (also called curing or vulcanization), these materials can not flow. Rubber materials can typically be stretched by more than twice their original length when external forces are applied and return nearly completely to their original length after the external force is released [66], i.e. they are very elastic.

For the improvement of certain properties of vulcanized rubbers, solid fillers are often added to the polymer before vulcanization. These fillers can be classified into reinforcing and non-reinforcing fillers.

In non-reinforcing fillers, physical interactions between the filler and the polymer are negligible and they are used to dilute the polymer matrix, i.e. to reduce the cost of the compound, or to reduce the tackiness (the stickiness) of the rubber [6, Chapter 3.1].

In composites with reinforcing fillers, physical interactions between the polymer and the particle surface result in the increase of the viscosity and modulus of the rubber and improve their mechanical properties such as the abrasion resistance, hardness, or tearing resistance [6, Chapter 3.1]. For a strong reinforcing effect, the filler needs a surface chemistry that enables the physical interactions with the polymer molecules and a large specific surface area. The two most important reinforcing fillers are CB and high-structure silica [54, 59, 67]. Due to its polar surface covered with silanol and hydroxyl groups, silica usually needs surface modification or additional organosilane additives to improve the interactions with the mostly apolar rubber chains [68]. The structure of CB is discussed in the previous section (Section 2.2.1).

Beside these solid fillers, commercial rubber materials usually contain many other additives [69]. Low viscous molecules can act as process oils (e.g. fatty acids) to enhance the processability or plasticizers (e.g. mineral oils, phthalates) to reduce the glass transition temperature of the compound [6, Chapter 3.3]. Aging properties are improved by adding anti-oxidants (such as substituted phenoles or diarylamines) and ozone protection additives (e.g. paraffin wax, *p*-phenylenediamines) [6, Chapter 3.4]. For the cross-linking reaction, a typical vulcanization system in a rubber material consists of elemental sulfur mixed with activators (ZnO_2 and stearic acid) and accelerators (sulfenamides, thiazoles, and so on) to increase the rate of the cross-linking [6, Chapter 3.2]. The

composition of a rubber compound is usually defined in complex recipes and the amount of each constituent is given as phr, i.e. parts per hundred parts of rubber by weight. An example for such a recipe is given in Table B.2 for one of the samples used in this work.

The addition of all these ingredients results in a heterogeneous and complex structure of the rubber compound. In the following, only the effect of solid, reinforcing fillers to a rubbery polymer is described in more detail, due to their tremendous effect on the rheological behavior of the compound [10, Chapter 1].

The physical interactions between the surface of the reinforcing filler and the polymer chains result in a polymer layer around the particles, in which the polymer chains have a reduced chain mobility [70]. This layer, the bound rubber, can also connect different CB aggregates and thereby a three-dimensional polymer–filler network is formed. Some rubber molecules, the occluded rubber, are partly shielded from external forces in the voids of filler particles and lead to an additional, strain-independent contribution to the modulus of the compound [55]. In Fig. 2.8 the structure of a rubber filled with CB is illustrated.

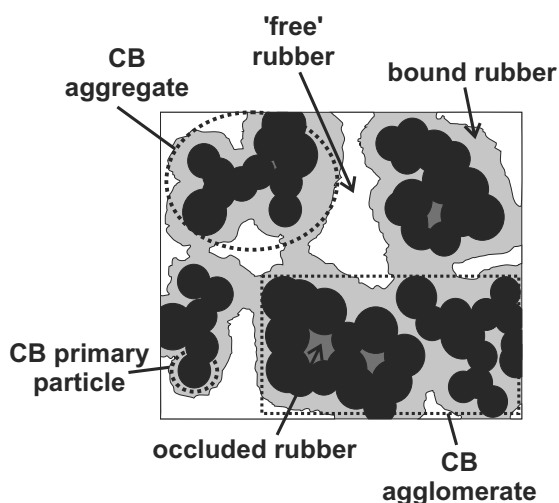


Figure 2.8.: Structure of a rubber filled with CB. Aggregates are the smallest dispersible unit in the compound and consist of spherical primary particles. An agglomerate is a group of CB aggregates, which are connected by physical interactions and can be broken into aggregates by mechanical force. Due to physical interactions some polymer chains are partly adsorbed on the filler surface. They form a rubber layer, the bound rubber, with reduced chain mobility around the particles, which also connects different CB aggregates. Thereby a physical 3D-network is formed. Polymer chains that are partly shielded from external forces by nearby CB aggregates form the occluded rubber.

The flocculation of CB aggregates into agglomerates eventually leads to the formation of a filler–filler network. The spatial extent of this network through the compound is increasing with increasing filler volume fraction and at a certain volume fraction, the percolation threshold ϕ_c , the network is spanning throughout the sample [71]. The presence of such a network drastically changes various material properties P , such as the storage modulus G' , the viscosity η , or the electrical DC-conductivity σ_{DC} . The change of the property P as function of the filler volume fraction can

often be described by a scaling law with the critical scaling exponent c [24, 72, 73].

$$P \propto (\phi - \phi_c)^c \quad (2.24)$$

The DC-conductivity of an insulating rubber (e.g. SBR) is for example increased by several orders of magnitude, when a conductive filler such as CB is added with a volume fraction above ϕ_c [73]. The reason for this high conductivity is the continuous filler–filler network, which forms conductive paths through the compound [71].

The value of ϕ_c is influenced by many parameters, such as the morphology and electrical properties of the particles, the matrix polymer, and the mixing process [56, Chapter 8.1], as well as the filler dispersion [74]. Also the anisotropy of the filler particles has a large influence on ϕ_c , which is the reason why carbon nanotubes have a much lower percolation threshold than CB (1 wt% and 8.75 wt%, respectively for the electrical percolation threshold [75]). The percolation threshold also depends on the choice of the investigated parameter P . The electrical percolation threshold of filled compounds is often higher than the rheological percolation threshold [75, 76]

2.2.3. Rheology of filled rubber under LAOS

Since the beginning of the twentieth century, filler particles, especially CB, are added into (vulcanized) rubber materials to enhance their mechanical properties [6, Chapter 3.1][10, Chapter 1.1]. A schematic graph of the shear modulus of a filled, vulcanized rubber as function of strain amplitude is shown in Fig. 2.9. There are three additional, filler induced effects on the modulus of a polymer network, which can be divided into strain-independent influences and strain dependent ones. Another important effect observed in filled elastomers is the dynamic stress softening, which is also called the Mullins effect. These topics will be introduced in the next sections. For a more detailed discussion on the rheology of filled rubber materials see the literature, e.g. [6, 12, 77, 78].

Strain-independent filler influence on the modulus

The first additional effect of the filler on the shear modulus is based on its hydrodynamic influence. Solid fillers increase the viscosity of fluids, which includes polymer melts, because they disturb the flow in the matrix [79]. Mathematically this was first explained by the viscosity law of Einstein

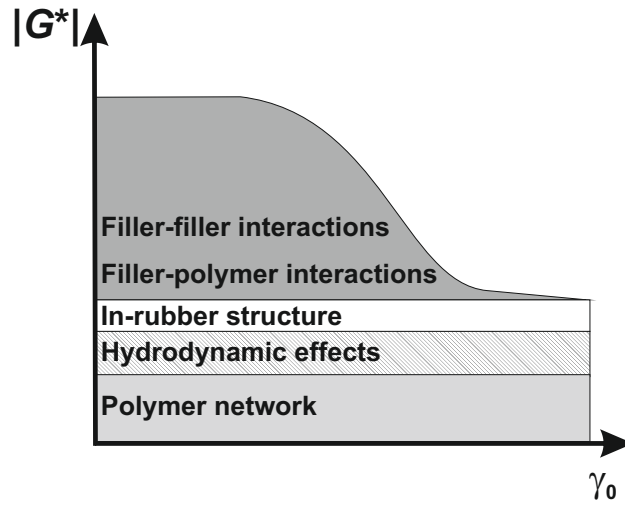


Figure 2.9.: Idealized influence of a reinforcing filler on the shear modulus of a (vulcanized) rubber. The hydrodynamic influence of the filler and its in-rubber structure (occluded + bound rubber) result in a strain-independent increase of the modulus. Filler-filler and filler-polymer interactions contribute to an additional increase of the modulus, which is diminished at larger strain amplitudes, due to the break up of the network structure (based on [10, 55]).

(Eq. 2.25) [34, Chapter 2.5.2], which describes the viscosity of a matrix $\eta(\phi)$ as a function of the filler concentration.

$$\eta(\phi) = \eta_0 (1 + 2.5\phi) \quad (2.25)$$

In this formula, η_0 is the viscosity of the unfilled matrix and ϕ is the filler volume fraction. This formula is only valid for the addition of hard, spherical particles and no effect of the particle size, their size distribution or interaction between the particles is included. Based on this work, $\eta(\phi)$ of more complex systems and at higher filler volume fractions is often described with a power series (Eq. 2.26), where the coefficients b_i depend on the actual system under investigation [80, Chapter 3.3.4.3].

$$\eta(\phi) = \eta_0 \left(1 + b_1\phi + b_2\phi^2 + b_3\phi^3 + \dots \right) \quad (2.26)$$

The linear term of such kind of equations describes the effect of single particles on the viscosity, the quadratic term adds interactions between two particles, and so on [81].

Depending on the shape of the particles, the volume fractions considered, and the assumptions made for the calculation, different parameters b_i were reported for Eq. 2.26 [10, Chapter 5]. This concept was for example adapted by Guth and Gold, who included the mutual disturbance caused by pairs of spherical particles in a laminar flow [79]. They reported values of 2.5 for b_1 and 14.1

for b_2 and found Eq. 2.27 applicable for the viscosity of various high molecular materials [79].

$$\text{spherical particles: } \eta(\phi) = \eta_0 (1 + 2.5\phi + 14.1\phi^2) \quad (2.27)$$

It was also found, that the principle of Eq. 2.26 could be applied to describe other material functions of rubber compounds, such as the Young's modulus E^* and the shear modulus G^* . In such compounds, the filler particles perturb the stresses and strains in the system when external forces are applied and thereby increase the elastic energy, which leads to a stiffening of the compound [81]. With Eq. 2.27, it is possible to describe the increase of the modulus with increasing filler volume fractions up to $\phi = 0.1$. At higher volume fractions the formation of a filler-filler network results in an increase of the modulus, which is higher than the one predicted by Eq. 2.27 [55]. For these higher filler concentration, Guth extended the model by interpreting the CB agglomerates as rod like particles and found Eq. 2.28 to describe the enhanced stiffness [81].

$$\text{rod-like particles: } E(\phi) = E (1 + 0.67f\phi + 1.62f^2\phi^2) \quad (2.28)$$

The shape factor f accounts for the anisotropic shape of the particles and is the length of the particle divided by its width [81].

Mullins and Tobin [82] found that the structure of the CB, which is neither a perfect sphere nor a rod, is an important parameter in this consideration. According to their research, Eq. 2.27 is appropriate to describe the Young's modulus of compounds filled with large, more spherical blacks, whereas compounds containing small, highly structured fillers are better described by Eq. 2.28 (for $\phi \leq 0.15$) [82]. They concluded in their work, that the influence of the filler on the modulus is limited to an amplification of the strain present in the deformable rubber matrix, which can be described by a strain amplification factor X (Eq. 2.29) [82].

$$\eta(\phi) = \eta_0 X \quad (2.29)$$

Recently, more complex theoretical approaches, such as the network junction theory [83], were used to calculate the amplification factor X .

Up to now, only the hydrodynamic effect of solid fillers on the rheological properties of rubber compounds was discussed. Another influence on the shear modulus independent of the strain amplitude is the so called in-rubber structure. The occluded rubber in the voids of the complex CB particles is partly shielded from the applied deformation [55, 84]. Additionally, some rubber chains are adsorbed on the filler surface and partly immobilized (bound rubber). Both, the occluded and the bound rubber act like an additional filler rather than like free polymer chains [10, Chapter 5.1.7]. This effect can be included into the description of the modulus by considering an effective filler volume fraction, ϕ_{eff} , rather than the actual CB filler volume fraction, ϕ , in the equation used for calculating the material functions (Eqs. 2.25 to 2.29).

Strain-dependent filler influence on the modulus

In dynamic strain amplitude tests it was found, that the shear modulus of filled elastomers is decreasing drastically already at strain amplitudes of a few percent [85]. This effect is usually referred to as dynamic stress-softening or Payne effect, after A. R. Payne, who published a series of papers [86, 87] on this effect in the 1960's. Payne found a decrease of $|G^*|$ by more than a decade for natural rubber compounds containing up to $\phi = 0.38$ CB with high surface area (high abrasion furnace CB), when the strain amplitude was increased from 0.001 to 0.1 [86]. He could also show that the type of CB used and its concentration in the rubber play a crucial role for the decrease of the modulus [86]. Aranguren et al. [88] studied the effect of the silica concentration on the dynamic shear modulus of a linear polydimethylsiloxane (PDMS) melt and found a similar influence of the filler volume fraction on the decrease of the shear modulus, as well as additional influences of the silica surface chemistry and the molecular weight of the PDMS. They attributed the Payne effect to the formation of a filler-polymer network. This network has three different contributions: a) direct bridges of single polymer chains adsorbed to two different particles, b) primary entanglements between two polymer chains adsorbed to different particles and c) secondary entanglements involving non-adsorbed PDMS chains [88].

Besides the contribution of the filler-polymer network, another proposed mechanisms for the dynamic strain softening considers the filler-filler network [10, Chapter 5.1.10]. A model, first developed by Kraus, considers an agglomeration process of the filler network caused by van-der-

Waals forces between the particles and a deagglomeration, due to the mechanical stress applied to the material [41]. In this framework, both processes are dynamic and have a certain rate with different rate constants. The model assumes a plateau of the storage modulus at low strain amplitudes and one at high strain amplitudes, both also found in experiments [41]. At rest and very low strain amplitudes, the rates for agglomeration and deagglomeration are equal and their strain dependencies are modeled with a power law [41]. The dynamic formation and destruction of the CB network results in an additional term for the loss modulus [41]. This model captures the strain amplitude dependence of the storage modulus well and predicts a peak of G'' when G' starts to decrease, which is also observed for vulcanized rubber compounds. However, it fails to predict the vertical asymmetry of this peak [10, Chapter 5.1.10]. Therefore, different improvements of this model were proposed, such as different strain exponents for the agglomeration and deagglomeration, an additional exponential decay of the loss modulus or including aggregate flocculation [10, Chapter 5.1.10]. This and other theories using a filler-filler network are only reasonable for filler volume fractions above or close to the percolation threshold. However, the Payne effect is also seen for compounds with lower contents of CB, so other mechanisms must also be included.

For a more elaborated review of different theoretical models for the Payne effect, the interested reader is referred to the literature, e.g. [10, 41].

Dynamic stress softening, Mullins effect

When filled elastomers are subjected to large amplitudes in a cyclic manner, the measured stress during the first cycle is usually larger than in the following cycles. After a few cycles, the material responses coincide during the following cycles [89]. When the extension exceeds the previous maximum deformation, the stress-strain response of the material corresponds to the monotonous uniaxial tension response [89]. This effect is often referred to as dynamic strain softening or the Mullins effect [90]. Many different physical interpretations have been proposed, which all involve changes in the microstructure of the compound. Diani et al. [89] summarized the most important ones in a comprehensive review. The possible interpretations include the rupture of chains from the filler surface, the break up of CB agglomerates, and the slipping of polymer chains over the surface of the filler. Layers of glassy polymer around the particles, which dynamically form bridges

with a certain lifetime, are also proposed as possible reasons for the Mullins effect [85, 91, 92].

FT rheology of filled elastomers

Despite the fact that filled elastomers show a strong decrease of the shear modulus with increasing strain amplitude (Payne effect), the measured values of nonlinear contributions to rubber materials were often found to be low and the stress response sinusoidal [16, 92, 93]. Therefore, it was concluded by the authors that this is a special feature of filled rubber materials, which would allow the interpretation of the mechanical properties in terms of linear parameters (such as G' and G'') even in the NVE regime [16, 92, 93].

Leblanc et al. [27] modified a standard rubber rheometer to capture the raw data of the stress and the strain signal and analyzed them with FT-rheology. They conducted a series of studies on many different rubber systems including unfilled rubber [27], CB filled rubber materials [12, 28, 29, 94, 95], and thermoplastic vulcanizates [96]. They found that the third higher harmonic contribution is important for rubber materials above strain amplitudes $\gamma_0 = 1$ and they could separate the nonlinear response in a superposition of two components [29]. The first of these components was attributed to the nonlinear contribution of the rubber matrix, which was assumed to be independent of the filler volume fraction and which increased monotonically with the strain amplitude [29]. The second component in the work of Leblanc et al. [29] is the nonlinear contribution of the filler to the material response, which had a maximum at a strain amplitude $\gamma_0 \approx 2$. Their interpretation for this filler dependent behavior was that the interactions between the rubber and the filler phase increase with strain amplitude and cause the increase of $I_{3/1}$ but above a critical strain amplitude these interactions are modified and the nonlinear contribution caused by the filler starts to vanish when γ_0 is further increased [29]. This is consistent with findings for the viscosity in suspensions, which often show a Newtonian plateau at low shear stresses and a second Newtonian plateau at very high shear stress [35, Chapter 10]. Between these two regimes with linear viscoelastic behavior, a nonlinear viscoelastic regime is found, where the viscosity is decreasing with increasing stress [35, Chapter 10]. For a silica filled compound Leblanc and Nijman [97] found similar behavior of the third higher harmonic contribution and variations during different steps of the mixing and silanization process could be observed.

2.3. Thermoplastic Elastomers and phase separation in block copolymers

The main reason for the mechanical properties of elastomers is their covalent three-dimensional network structure. The drawback of this network is that vulcanized rubbers can not be processed or reshaped after cross-linking. Also their composition can not be changed afterwards and the reclaiming of these elastomers necessitates the destruction of the vulcanized structure [8, 98]. Thus the combination of the elastic properties of elastomers and the processability of thermoplastics (in extrusion, injection molding, film blowing, etc.) is an interesting field of research, which resulted in the development of a completely new class of polymeric materials since the mid 1960's, the so called thermoplastic elastomers (TPEs) [31].

Today there are many different types of TPEs, which are all composed of a phase-separated system with one phase being a rubber like polymer and the other a thermoplastic one [32]. The mechanical behavior of a TPE depends strongly on the actual temperature in relation to the glass transition temperature of the rubber, $T_{g,R}$, and the one of the thermoplastic phase, $T_{g,T}$ ($T_{g,R} < T_{g,T}$). At temperatures between $T_{g,R}$ and $T_{g,T}$, the material is elastic like a vulcanized rubber. At temperatures higher than $T_{g,T}$, a TPE behaves like a polymer melt and can easily be processed. Below $T_{g,R}$ a TPE is a brittle material. The three major types of TPEs are blends, dynamically vulcanized rubber-plastic alloys (thermoplastic vulcanizates, TPVs), and block copolymers [99, Chapter 2].

Blends and TPVs are very similar in structure. They both consist of a mixture of a rubber and a thermoplast. The thermoplastic part typically forms the continuous phase [99, Chapter 2]. The major difference between the two types of TPEs is that in the TPV, the rubber particles are cross-linked during the melt-mixing of the two phases (dynamic vulcanization) [100, 101]. An important TPV is the so called thermoplastic olefin, a mixture of cross-linked EPDM (ethylene-propylene-diene monomer) rubber dispersed in polypropylene, which has a wide range of application in the automotive and construction industry.[100]

Block copolymers are the oldest type of TPEs [31]. In this kind of polymers, the thermoplastic and the rubber part are covalently bound together in a polymer chain. Thus the two different components can not phase separate on a macroscopic scale and only microphase separation is

possible [102].

The phase behavior of $(A-B)_n$ block copolymers composed of the two monomers A and B is based on the relation between entropic and enthalpic effects. The entropy of such polymers is determined by the polymerization stoichiometry (namely their overall degree of polymerization N), the architecture of the chains (represented by n), and their composition (i.e. the volume fraction Φ of polymer A), whereas the enthalpic contribution is given by the A–B segment-segment (Flory-Huggins) interaction parameter χ [103]. The interaction parameter χ is defined as [104, Chapter 13]:

$$\chi = \frac{Z}{k_B T} \left(\varepsilon_{AB} - \frac{(\varepsilon_{AA} - \varepsilon_{BB})}{2} \right) \quad (2.30)$$

where Z is the number of closest neighboring monomer units to a monomer unit within the copolymer configuration cell, k_B is the Boltzmann constant, ε_{AB} the interaction energy per monomer unit between A and B monomers, ε_{AA} and ε_{BB} the interaction energies per monomer unit between the same monomers [104, Chapter 13]. The value of χ , which has no unit, thus depends on the selection of the A–B monomer pair and is also a function of the temperature according to Eq. 2.31.

$$\chi \approx \alpha T^{-1} + \beta \quad (2.31)$$

The parameters α and β depend on the monomer combination, their composition Φ , and n [103]. A positive χ indicates repulsion between monomer A and monomer B, whereas a negative χ signifies mixing of the two monomers [104, Chapter 13].

Much research has been done on both the theoretical calculation and the experimental determination of the phase behavior of block copolymers as a function of χ , n , N and Φ (e.g. [102, 103, 105–108]). A typical result of the theoretical work is given in Fig. 2.10, where the phase diagram of a symmetric diblock melt ($n = 1$) calculated by mean-field theory is shown as function of the product χN and the volume fraction of monomer A, Φ . The product χN controls the degree of segregation between the A and B blocks [108]. At values $\chi N \ll 1$, the copolymer melt is disordered (DIS), if χN is in the order of 10, a disorder-to-order phase transitions occurs and the composition profile is sinusoidal, if $\chi N \gg 10$, the segregation is strong and the composition profile is similar to a step function with narrow interfaces [103]. Depending on χN and Φ , different phase morphologies

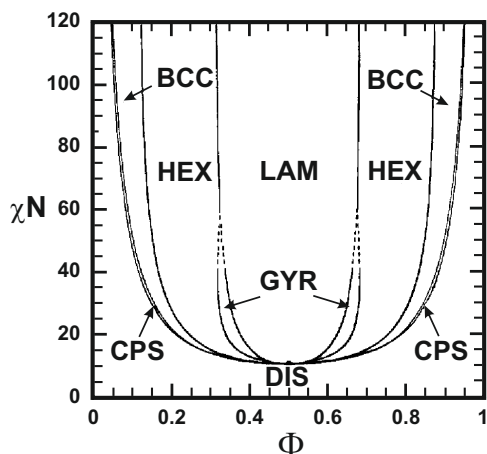


Figure 2.10.: Phase diagram calculated by mean-field theory for a conformationally symmetric diblock (i.e. $n = 1$) copolymer melt as a function of the Flory-Huggins interaction parameter χ , the degree of polymerization (N) and the volume fraction of block A (Φ). The different phases are lamella (LAM), hexagonal cylinders (HEX), gyroid (GYR), bcc spheres (BCC), close-packed spheres (CPS) and disordered (DIS). The dashed lines denote the extrapolated phase boundaries and the dot denotes the mean-field critical point. Adapted with permission from [108]. Copyright 1996 American Chemical Society.

are expected. The most important morphologies of an $(A-B)_n$ copolymer are also illustrated in Fig. 2.11. This includes the lamellar phase (LAM), hexagonal oriented cylinders (HEX), a bicontinuous cubic phase with $Ia\bar{3}d$ symmetry (GYR), which is also called gyroid phase, and two spherical morphologies, either body centered cubic (BCC) or close packed (CPS, not drawn in Fig. 2.11).

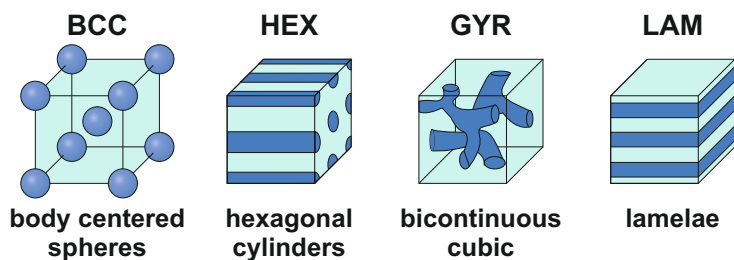


Figure 2.11.: Important phases in an $(A-B)_n$ block copolymer. The minor component is painted darker.

3. Performance of a rubber rheometer under LAOS

Rubber rheometers differ from common shear rheometers with cone and plate or parallel plate geometries (see Fig. 2.2, p. 6) as they have a sealed, cone-cone geometry, which is shown in Fig. 3.1. The surfaces of the upper and the lower geometry of a rubber rheometer contain several grooves to

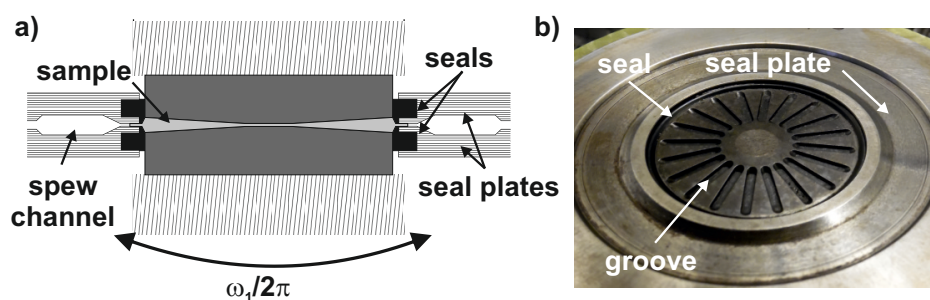


Figure 3.1.: a) Schematic cross section of the cone-cone geometry in a rubber rheometer. Excess of sample material is flowing into the channel between the sealing plates. This excess material, together with the sealing rings, closes the geometry during the measurement. b) Picture of lower geometry in a V50 rheometer. Several grooves in the surface shall decrease sample slipping.

prevent slippage of the polymer [109]. Measurements are done under pressurized conditions, which restrains the slippage of the elastomer on the geometry surface, as could be shown for Mooney viscometers [110, 111]. The pressure applied on the upper geometry throughout the measurement also hinders the formation of a porous structure during the vulcanization of rubbers [112]. This set-up allows reproducible measurements of filled elastomers even at high strain amplitudes [12]. After the measurement, residual sample material in the corners of the grooves makes the cleaning of the geometry tedious. Therefore a thin polymer foil (with a high T_g of the polymer) is often placed between the sample and each geometry to facilitate the cleaning after the measurement.

Due to the two truncated cones, a constant strain rate throughout the gap is expected in the

geometry during shear [26, 113]. However, there is an error from the ideal homogeneous flow, because of the fixed boundaries at the sealing rings. Numerical simulations of torsional flow of a Newtonian fluid showed an increase of the shear rate close to the edge between the lower, moving geometry and the lower sealing ring and consequently the shear rate is decreased around the edge of the upper geometry and the upper sealing ring [26]. The difference in torque between the closed, cone-cone geometry and a cone and plate geometry was found to be 10.6 % for a Newtonian fluid by numerical calculations [26]. Measurements on two layers of polyethylene with different colors did also show non-homogeneous flow at the corners of the geometry [109]. Despite these deviations in the flow field, experimental results of linear measurements showed a good agreement with results from open gap rheometers, i.e. the deviation in the plateau modulus between a rubber rheometer and three standard open gap rheometers was found below 20 % [26].

In the following sections the performance of a SIS-V50 rubber rheometer (hereinafter: V50) from Scarabeaus GmbH (Wetzlar, Germany; now TA Instruments, New Castle, DE) under LAOS was studied in detail. The software of the instrument is capable of calculating the relative higher harmonic contributions of the stress response up to the tenth higher harmonic. Additionally, the raw data of both the strain excitation and the stress response were recorded with an external ADC card (using the oversampling technique to increase sensitivity [49, 114]) and analyzed with a home-written LabView[®] routine [115] to obtain the relative higher harmonic contributions of both signals. The data of the instrument's software and the home-written routine match, e.g. for a polystyrene melt (PS-1, Table 3.1) typical differences in $I_{3/1}$ are below 5 % at $\gamma_0 > 0.2$ ($T = 190\text{ }^\circ\text{C}$, $\omega_{1/2\pi} = 0.5\text{ Hz}$). For the further course of this chapter, only the results from the instrument's software were used when nothing else is explicitly mentioned. Different polymers (see Table 3.1) were measured on the V50 rubber rheometer and on a standard open gap rheometer (ARES G2, TA Instruments), and the results are compared (Section 3.1).

3. Performance of a rubber rheometer under LAOS

Table 3.1.: Polymers used to investigate the performance of the rubber rheometer.

| Name | Polymer | M_w [kg mol ⁻¹] | PDI ^a | Polymerization technique | Styrene content |
|--------------------|--|----------------------------------|------------------|-----------------------------|--------------------|
| PE-1 | polyethylene- <i>co</i> -hexene | | | radical | |
| PS-1 | polystyrene | 292 | 1.34 | anionic | 100 mol% |
| S-SBR ^b | styrene butadiene rubber | 398 | 1.83 | anionic | 13.7 mol% |
| E-SBR ^b | styrene butadiene rubber | 750 | 6.5 | radical | 17.1 mol% |
| SIS-I | poly(styrene- <i>b</i> -isoprene- <i>b</i> -styrene) | 147 | 1.44 | anionic | 10.6 mol% |

^a polydispersity index

^b filled with different amounts of CB and various additives (Appendix B.3, Appendix B.5)

Some features relevant for measurements on the rubber rheometers are discussed in detail, too (Section 3.2). In addition, emulsion polymerized SBR (E-SBR), filled with various volume fractions of CB, was measured on the V50 rubber rheometer and the results are compared to those of Leblanc et al. [12], who investigated the same samples on a RPA 2000 rubber rheometer (Section 3.3). In Table 3.2, the technical data for the three different rheometers used in this study is summarized.

Table 3.2.: Technical data of the rheometers used. Data based on information by the manufacturer [116–118].

| Property | V50 | ARES G2 | RPA 2000 |
|----------------------------|--------------------------|---------------------------|--------------------------|
| T range [°C] | 30 – 200 | –150 – 600 ^a | ambient – 230 |
| $\omega_1/2\pi$ range [Hz] | $1.0 \cdot 10^{-2}$ – 50 | $1.6 \cdot 10^{-8}$ – 100 | $1.6 \cdot 10^{-3}$ – 50 |
| M range [N m] | 10^{-3} – 20 | $5 \cdot 10^{-8}$ – 0.2 | not given |
| M resolution [N m] | 10^{-3} | 10^{-9} | not given |
| Oversampling ^b | yes | yes | no |

^a Forced convective oven and cooling with liquid nitrogen

^b Oversampling technique [49] used by the software of the instrument

3.1. Comparison with open gap geometry rheometer

A linear polystyrene sample, PS-1, was measured on the V50 and the ARES G2 open gap rheometer. For the ARES G2, an Invar cone and plate geometry was used with a diameter of 13 mm and a cone angle of 0.1 rad.

At low to medium strain amplitudes ($\gamma_0 < 0.8$), the absolute value of the complex shear modulus $|G^*|$ and $\tan \delta$ of both instruments differ by usually less than 10% as can be seen in Fig. 3.2. However, the results of both instrument deviate at strain amplitudes above $\gamma_0 = 0.8$. The modulus

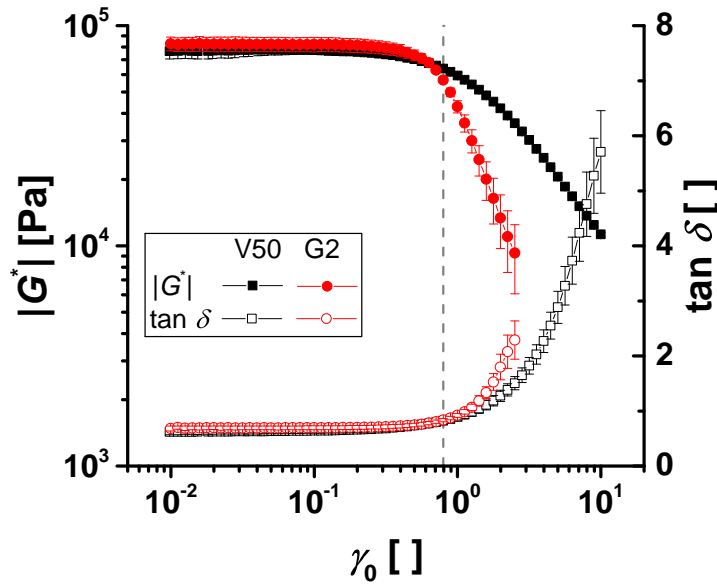


Figure 3.2.: Absolute value of the complex modulus, $|G^*|$, and $\tan \delta$ of PS-1 measured on the V50 and the ARES G2 (average of three specimen for each instrument). At low amplitudes the results of both instrument differ by $\pm 10\%$. Above a strain amplitude of $\gamma_0 = 0.8$ (dashed line) the values start to deviate ($\omega_1/2\pi = 0.5$ Hz, $T = 190$ °C).

drops drastically on the ARES G2 and $\tan \delta$ start to increase. Also the standard deviation of $|G^*|$ increases with increasing γ_0 . These results are most probably due to slippage of the sample on the smooth surface of the geometry and the appearance of irregularities on the edges of the specimen (edge effect), which both start to dominate the response at larger amplitudes. On the V50, the decrease of $|G^*|$ at large amplitudes is not as steep as on the ARES G2 and the standard deviation between the measurements is smaller, especially for $|G^*|$. This can be attributed to the sealing of the geometry at the edges that prevents the occurrence of edge effects as well as to the grooved surface and the applied pressure, which reduce the slip of the polymer.

3. Performance of a rubber rheometer under LAOS

For PS-1, the nonlinear results measured on the V50 and the ARES AG2 were also compared and in Fig. 3.3, $I_{3/1}$ is plotted as function of γ_0 for the two rheometers.

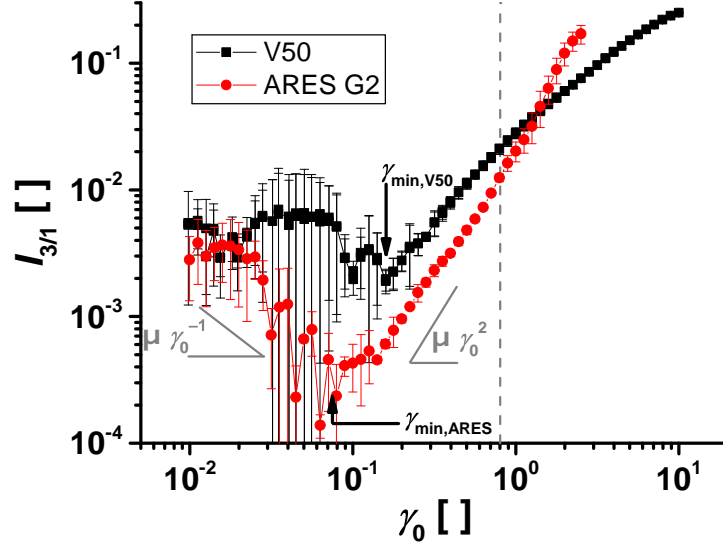


Figure 3.3.: Relative third higher harmonic contribution $I_{3/1}$ as function of γ_0 for PS-1 ($\omega_1/2\pi = 0.5$ Hz, $T = 190$ °C) measured on the ARES G2 and the V50. The dashed line indicates the strain amplitude, at which $|G^*|$ of the two instruments started to deviate (see Fig. 3.2). At low strain amplitudes the signal of both instruments is determined by noise. The arrows indicate the onset of the quadratic scaling of $I_{3/1}$ with γ_0 for the ARES G2 and the V50 ($\gamma_{\min} = 0.075$ and 0.16 , respectively).

The stress response in both instruments is dominated by noise at low strain amplitudes ($\gamma_0 < 0.1$), as can be seen by the decrease of $I_{3/1}$ with increasing γ_0 and the high standard deviation that is indicated by the error bars. For linear homopolymer melts, a quadratic scaling of $I_{3/1}$ with γ_0 is expected at medium amplitudes (in the so called medium amplitude oscillatory shear regime, see Eq. 2.20, p. 14) [25, 53]. This scaling is also found in measurements on both instruments, but the onset of this scaling is at different strain amplitudes ($\gamma_{\min,V50}$ and $\gamma_{\min,ARES}$, respectively). Wilhelm et al. [51] described $I_{3/1}$ by Eq. 2.23 (p. 14) and defined the onset of the quadratic scaling γ_{\min} as the minimum of this curve, i.e. the strain amplitude, where the derivative of Eq. 2.23, Eq. 3.1, is zero (Eqs. 3.2 and 3.3).

$$\frac{dI_{3/1}}{d\gamma_0} = -A\gamma_0^{-2} + 2Q_0\gamma_0 \quad (3.1)$$

$$0 = -A\gamma_{\min}^{-2} + 2Q_0\gamma_{\min} \quad (3.2)$$

$$\gamma_{\min} = \left(\frac{A}{2Q_0} \right)^{\frac{1}{3}} \quad (3.3)$$

For the ARES G2, the onset of the quadratic scaling, $\gamma_{\min, \text{ARES}} = 0.075$, was calculated with Eq. 3.3. For the V50, a peak of $I_{3/1}$ at $0.01 < \gamma_0 < 0.1$, is present, thus Eq. 2.23 is not valid and the lowest data point of $I_{3/1}$ was used to define the onset $\gamma_{\min, \text{V50}} = 0.16$ instead. This value is twice as high as the one for the ARES G2. The peak of $I_{3/1}$ at low γ_0 was found in many measurements on the V50 for various polymers and therefore focus of a separate investigation (Section 3.2).

To quantify the difference in $I_{3/1}$ between the two instruments in the MAOS regime, the Q-parameter (Eq. 2.21) was calculated and the intrinsic nonlinearity Q_0 (Eq. 2.22) was determined by a linear fit of $\log(Q)$ (slope = 0) in the MAOS regime (Fig. 3.4).

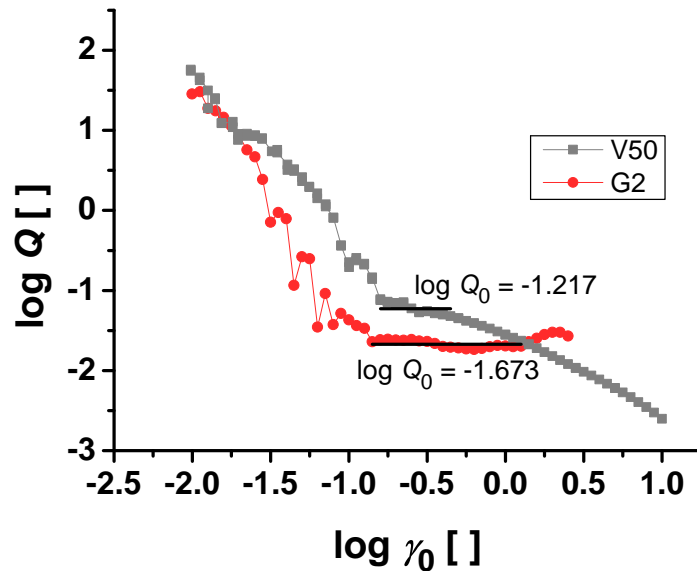


Figure 3.4.: Q-parameter (Eq. 2.21) as function of $\log(\gamma_0)$ measured on the V50 and the ARES G2 for PS-1 ($\omega_1/2\pi = 0.5$ Hz, $T = 190$ °C, average of three measurements on each instrument). At low values of $\log(\gamma_0)$ ($\log(\gamma_0) < -1$), $\log(Q)$ is decreasing, because the stress response is dominated by noise. This regime is followed by a plateau of $\log(Q)$, which is used for the calculation of the intrinsic nonlinearity Q_0 (horizontal line). The measured value for Q_0 is approximately three times higher on the V50 than on the G2.

The intrinsic nonlinearity Q_0 measured on the V50 is almost three times higher than the one measured on the ARES G2. The reason for this is most probably due to the difference in the geometry setup. For parallel plate geometries, it was found that the intrinsic nonlinearity is lower than for cone-plate due to the non-homogeneous flow and has to be corrected by a factor of 1.5 [39]. The V50 has a cone-cone geometry, which should result in homogeneous flow like in the cone-plate

geometry and hence quantitative similar results were expected [119]. However, the sealed edges in the V50 introduce secondary flows [26, 109], which might lead to an increase of the nonlinear contribution.

Another possible source of deviation could be the polymer foil, which is usually put between each surface of the geometry and the sample in rubber rheometers. This foil, made of a polyester, shall facilitate the cleaning of the geometry, which is else often tedious (especially for low viscous samples) due to the grooves. Therefore, the same test as previous was done on the PS-1 without foil. The difference between the measurements with and without foil are in the same order of magnitude ($\pm 10\%$) as the standard deviation of the measurements without foil. Hence, the effect of the foil on Q_0 should be negligible.

3.2. Investigation of the peak in $I_{3/1}$ at small strain amplitudes

During nonlinear measurements on the V50 for most of the samples, a broad peak of $I_{3/1}$ was found at small strain amplitudes (usually $0.01 < \gamma_0 < 0.1$). This can be seen for example in Fig. 3.5 for a polystyrene melt (PS-1).

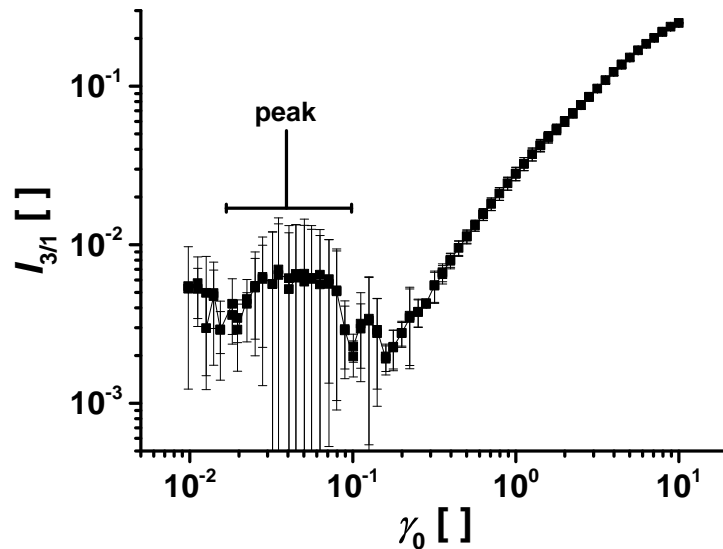


Figure 3.5.: Relative third higher harmonic contribution $I_{3/1}$ as function of γ_0 for PS-1 ($\omega_1/2\pi = 0.5$ Hz, $T = 190^\circ\text{C}$) measured on the V50 rheometer. A broad peak of $I_{3/1}$ is found at $0.02 < \gamma_0 < 0.1$.

This peak does not fit in the theoretical explanations (Section 2.1.2, p. 10) for neither the SAOS

regime, where $I(3\omega_1)$ is dominated by noise and a decrease of $I_{3/1}$ with increasing strain amplitude is expected ($I_{3/1} \propto \gamma_0^{-1}$), nor the MAOS regime, where a scaling law of $I_{3/1} \propto \gamma_0^2$ is predicted for linear homopolymer melts. Therefore this peak was further investigated systematically and different hypotheses for the occurrence of this peak were tested.

The first hypothesis was an additional nonlinear contribution caused by the deformation of an interface in the sample. The idea based on previous results on heterogeneous samples. Reinheimer et al. [23] found the presence of a similar peak for the emulsion of two Newtonian fluids (polydimethylsiloxane (PDMS) in polyisobutylene). They attributed the increase of the nonlinear contribution causing this peak to the deformation of the interface between the PDMS droplets and the polyisobutylene matrix. Similar results were also found on beer foam [51]. The presence of a deformable interface is obvious for the rubber samples tested, because beside CB they also contain different additives such as process oil, activators, anti-aging additives and so on. These chemicals might phase separate from the rubber matrix and hence create interfaces. It is known for example from literature that mineral sulfur tends to diffuse to the surface of rubber samples during storage (the formed sulfur layer is called bloom) [120] and ozone protective waxes often have a low solubility in rubber polymers at room temperature [6, Chapter 3.4.3]. In polymers, such as PS-1, the presence of interfaces is not expected, instead a homogeneous melt should be present. The interface might be explained by a problem that was seen after many measurements of polymer melts on the V50: the presence of gas bubbles in the specimen. These bubbles most probably are caused by air trapped in the corners of the grooves, when the geometry is closed and the polymer is pressed into shape. Evaporation of remaining solvent is unlikely, because these bubbles also appeared in specimen of industrial samples (dry granulate). The granulate was pressed into shape afterwards at elevated temperatures (typically $T = 180^\circ\text{C}$) under vacuum for at least 30 min. However, this peak was also found for specimen, where no bubbles were observed after the measurement.

The second hypothesis was the presence of an oil film on the geometry surface, which might cause additional slip effects that may be responsible for the peak in $I_{3/1}$. The rubber materials measured on the V50 usually all contain fatty acids and process oil. These might phase separate from the polymer as mentioned before and concentrate at the interface between the specimen and the geometry. This oil film might remain on the surface afterwards, especially in the corners of

the grooves and between the sealing rings and the geometry. This could cause the appearance of the peak for polymer melts without oil (and without gas bubbles in the specimen), too. To investigate the influence of an oil film on the nonlinear rheological properties, an industrial SIS triblock copolymer (SIS-I, Table 3.1) was tested and the results are shown in Fig. 3.6. First, the

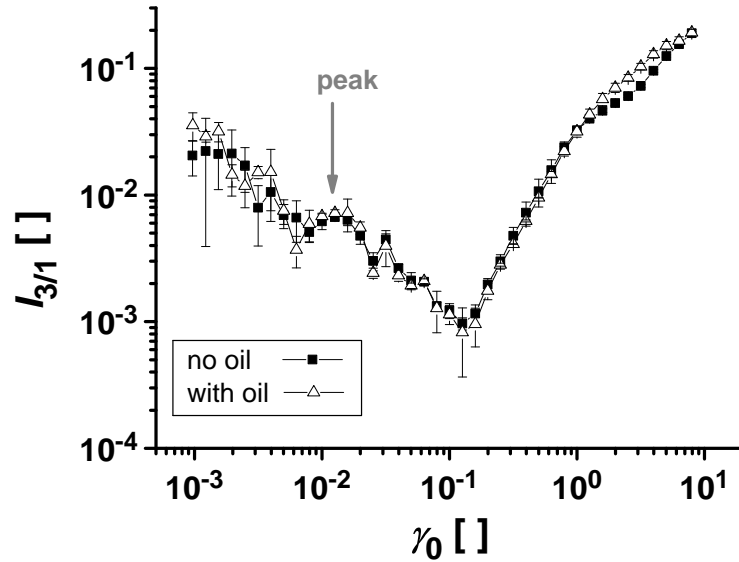


Figure 3.6.: Influence of an oil film on the nonlinear properties of SIS-I ($\omega_1/2\pi = 0.2\text{Hz}$, $T = 80^\circ\text{C}$, V50 rheometer). First, the geometry was cleaned (with water and acetone) and the two sealing rings were replaced with new ones. Then the polymer was measured (samples no oil, full symbols). Afterwards, an oil was sprayed on both geometry surfaces and the polymer was measured again (samples with oil, open symbols). No influence of the oil on $I_{3/1}$ is visible, the peak is still present (although very weak) for all samples.

polymer was measured (four specimen, “no oil”) after both geometry parts were thoroughly cleaned with water and acetone. Also the sealing rings were replaced with new ones. Then a film of oil was sprayed on both geometry parts before the sample was measured (two specimen, “with oil”). As can be seen in Fig. 3.6, there is no influence of the oil on $I_{3/1}$ observable at small strain amplitudes and neither the peak position nor its height do change. Instead, a deviation is only seen at very high strain amplitudes ($1 < \gamma_0 < 7$), where the increase is smoother for the sample with the oil film. This behavior might be explained by less friction at the interface between sample and sealing rings when the specimen is covered with oil.

The third possible explanation for the peak is a nonlinear contribution of the instrument itself. If the strain signal is not perfectly sinusoidal, additional higher harmonic contributions are expected in the stress response, because $I_{3/1}$ of the stress signal is the vector sum of all higher harmonic

contributions with the same frequency ($3\nu_1$), no matter if they are coming from the material response or the excitation. In Fig. 3.7 the third higher harmonic contributions to the stress ($I_{3/1,\sigma}$) and the strain signal ($I_{3/1,\gamma}$) are plotted as function of γ_0 . At low γ_0 ($\gamma_0 < 0.1$), the magnitude

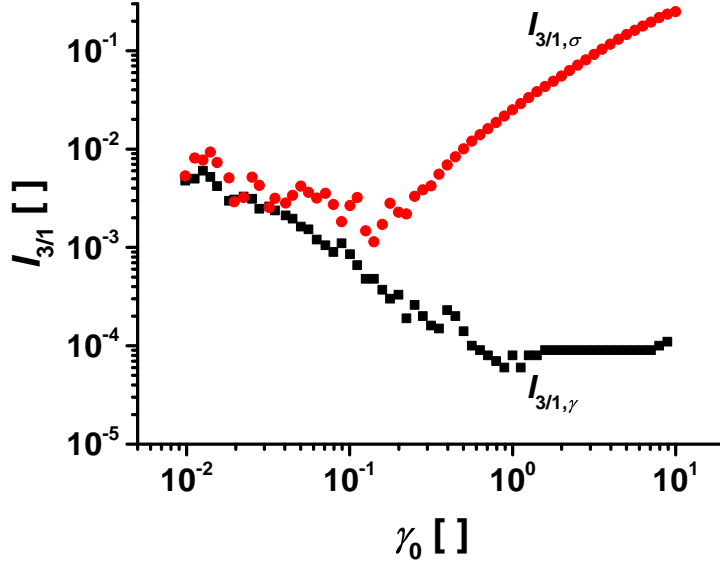


Figure 3.7.: Relative third higher harmonic contribution to the strain ($I_{3/1,\gamma}$, squares) and the stress signal ($I_{3/1,\sigma}$, circles) of PS-1 measured on the V50 calculated by an external software. At low strain amplitudes ($\gamma_0 < 0.1$), $I_{3/1,\gamma}$ is as high as $I_{3/1,\sigma}$. With increasing γ_0 , $I_{3/1,\gamma}$ is decreasing until it reaches a plateau at very low values ($I_{3/1,\gamma} = 10^{-4}$), whereas the stress contribution is increasing.

of the nonlinear strain contribution is similar to the magnitude of the stress response, but with increasing strain amplitude the motor control is improved and the excitation contains almost no third higher harmonic contribution ($I_{3/1,\gamma} \approx 10^{-4}$). In the strain amplitude range, where the peak, or in this case the plateau, of $I_{3/1}$ was found ($0.01 < \gamma_0 < 0.1$), the nonlinear contributions to the stress and the strain signal have almost the same intensity. However, there is no special increase of $I_{3/1,\gamma}$ that could explain the peak in the nonlinear stress response. So the nonlinear strain excitation can not explain the peak in the stress response.

In Fig. 3.8, $I_{3/1}$ is plotted for three different polymers (polyethylene PE-1, polystyrene PS-1, and solution styrene butadiene rubber S-SBR, Table 3.1, p. 30) during a strain sweep test at $\omega_1/2\pi = 0.2$ Hz. The measurement temperature of each polymer was chosen in a way that the three polymers have approximately the same absolute value of the torque response for each strain amplitude. The corresponding $I_{3/1}$ values are very different. The peak is most pronounced for the S-SBR, which also shows the largest nonlinearities at high strain amplitudes. The peak is very

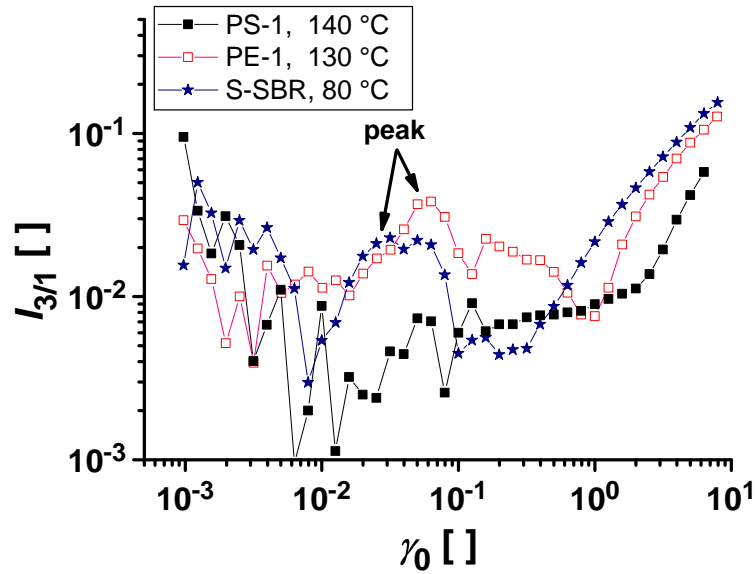


Figure 3.8.: Nonlinear parameter $I_{3/1}$ measured on the V50 for three different polymers with similar torque values ($\omega_1/2\pi = 0.2$ Hz). For the polyethylene (PE-1) and the unfilled solution SBR (S-SBR) the peak is clearly visible, while it is not pronounced in the polystyrene (PS-1).

broad ($0.01 < \gamma_0 < 1$) for the PE-1 and for the PS-1 only a plateau in $I_{3/1}$ is visible. The sample PS-1 shows the lowest values of $I_{3/1}$ over the almost the whole strain amplitude range measured. The reason for the peak is thus not explained by a contribution, which depends only on the torque (i.e. the motor excitation) but also on the polymer.

In September 2014, parts of the V50 rheometer were changed by the manufacturer. These changes included a slightly different geometry (better cooling and the grooves have different shape), a new motor control and a change of the upper geometry part, which included the installation of an additional pressure sensor for measuring the normal forces during shear. This modification of the instrument proved that the peak is mainly caused by the instrument, because since then, the peak is shifted to lower strain amplitudes for all samples measured since the modification. This is illustrated in Fig. 3.9 for an S-SBR compound with 40 phr CB (Appendix B.3), which was measured before and after the modification. However, due to the manifold changes made during the modification, no exact origin of the peak could be identified, yet.

In Table 3.3 the results of the different measurements performed are summarized.

Table 3.3.: Summary of experiments performed to identify the origin of the peak in $I_{3/1}$ at low strain amplitudes ($0.01 < \gamma_0 < 0.1$).

| Hypothesis for origin | Experiment | Results | Interpretation |
|---|---|---|---|
| Deformation of interfaces | Measurement of polymers without additives (PS-1) | Peak observed, even for specimen without bubbles after measurement | not plausible |
| Oil film on geometry surface | Measurement of SIS-I after cleaning of the geometry and after adding of an oil film | Peak in both measurements observed, no difference between measurement with and without oil in this γ_0 -range | not plausible |
| Nonlinear contribution of the strain signal | Analysis of the FT-spectra of the strain signal | $I_{3/1,\gamma}$ has same magnitude than $I_{3/1,\sigma}$ in this γ_0 -range, but no peak | not plausible |
| other contribution of the instrument | Measurement of various polymers with similar torque Measurement before and after the instrument modification | for PE-1 and S-SBR peak observed, no peak for PS-1 Peak shifted to smaller strain amplitudes ($0.005 < \gamma_0 < 0.05$) | Origin not related to torque of the sample Peak connected to one of the parts modified |

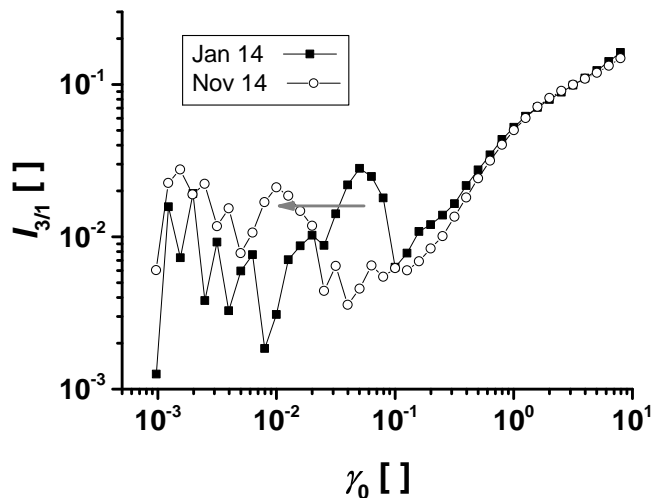


Figure 3.9.: Nonlinear parameter $I_{3/1}$ measured on the V50 for a S-SBR filled with 40 phr CB (phr: parts per hundred weight percent of rubber) before (January 2014) and after (November 2014) the modification of the instrument by the manufacturer in September 2014. The peak of $I_{3/1}$ is shifted to lower strain amplitudes after the modification.

3.3. Comparison of the V50 with an RPA 2000 rheometer

3.3.1. Experimental approach

In order to study the sensitivity of the V50 rubber rheometer, CB filled emulsion SBR was tested and the results were compared with those of Leblanc et al. [12], who measured the same samples on an RPA 2000 rubber rheometer (hereinafter: RPA) from Alpha Technologies (Akron, OH). For each of the nine sample materials, two specimen were tested with each instrument. The technical data of the two instruments was already given in a previous section (see Table 3.2, p. 30). This study was already started during the diploma thesis [121] and parts of the results were already mentioned therein.

The samples consisted of emulsion polymerized SBR (E-SBR) with 17.1 mol% styrene as rubber matrix and 0 phr to 50 phr, i.e. $\phi = 0$ to 0.184, CB (grade N330) as reinforcing filler. Standard additives (16 phr) were included to increase the aging stability and to enhance the mixing properties. The samples were compounded by Prof. Leblanc and the detailed recipe is given in Appendix B.5 and in [12].

The measurement procedure on the V50 was the following. A LAOS strain amplitude test with $\gamma_0 = 10^{-3}$ to 10 was performed with an excitation frequency of $\omega_1/2\pi = 0.5$ Hz. Before and after

the LAOS test, a SAOS frequency test ($\omega_1/2\pi = 0.1$ Hz to 10 Hz, $\gamma_0 = 0.05$) was performed to check for structural changes during the LAOS strain amplitude test. Between all tests, a resting period of 5 min was included.

The measurement procedure used by Leblanc et al. is described in detail in [12]. The LAOS strain amplitude experiment was divided in two subsequent runs ($\omega_1/2\pi = 0.5$ Hz, $\gamma_0 = 0.07$ to 10), separated by a resting period of 2 min. The raw data of the strain excitation and the stress response were recorded with an external 16-bit ADC card and the Fourier-transformed results calculated by a MathCad[®] routine. Leblanc et al. [12] corrected their measured nonlinear data for effects of nonlinear strain excitation at small strain amplitudes. In this study, only the uncorrected data received from the authors was used for the comparison, as the influence of the instrument is a major focus of this chapter. Therefore, the nonlinear data for the RPA shown here slightly deviates from the data published in [12].

3.3.2. Results

In Fig. 3.10, $|G^*|$ and $\tan \delta$ are shown for samples filled with $\phi = 0$ (left graph) and $\phi = 0.184$ CB for both rheometers. The lowest γ_0 used in the study of Leblanc et al. ($\gamma_0 = 0.07$) is in the NVE

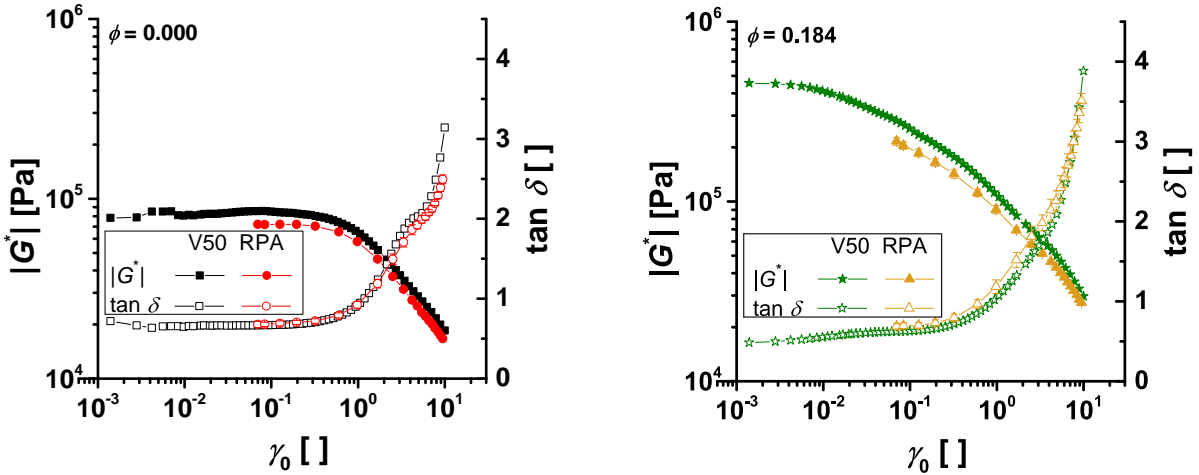


Figure 3.10.: Absolute value of the complex modulus $|G^*|$ and $\tan \delta$ of SBR samples with $\phi = 0$ (left) and $\phi = 0.184$ CB measured in the LAOS test ($\omega_1/2\pi = 0.5$ Hz, $T = 100$ °C) with the V50 and the RPA. The shear modulus $|G^*|$ is between 15 % to 30 % higher on the V50 than on the RPA.

regime for the highly filled elastomers with a volume fraction $\phi > 0.119$. The measured values of $|G^*|$ are between 15 % to 30 % larger on the V50 than on the RPA. This difference is larger

3. Performance of a rubber rheometer under LAOS

than typical deviations between different instruments. Merger and Wilhelm [38] measured PI and polyisobutylene on four different open-gap rheometers and found a difference in moduli and $\tan \delta$ of less than 12 % in the LVE regime. Leblanc and Mongrue [26] reported a difference of up to 20 % in the plateau modulus of an anionic polystyrene melt between five different rheometers (one RPA and four different open-gap rheometers) in three different laboratories. In their study, the RPA showed also the lowest values of the modulus. A reason for the significant difference in $|G^*|$ found between the RPA and the V50 in this study might be the different strain history of the samples in both rheometers. In the V50, a frequency test was performed before the LAOS test and the LAOS test already started at $\gamma_0 = 10^{-3}$. The comparison of the two frequency tests before and after the LAOS testing on the V50 showed an increase in the loss factor by up to 10 % after the LAOS test. This indicates a change in the physical structure of the compounds by the LAOS test.

In Fig. 3.11, $|G^*(\phi)|$ normalized to the value of the unfilled compound is plotted as a function of the filler volume fraction at $\gamma_0 = 0.07$ for both rheometers.

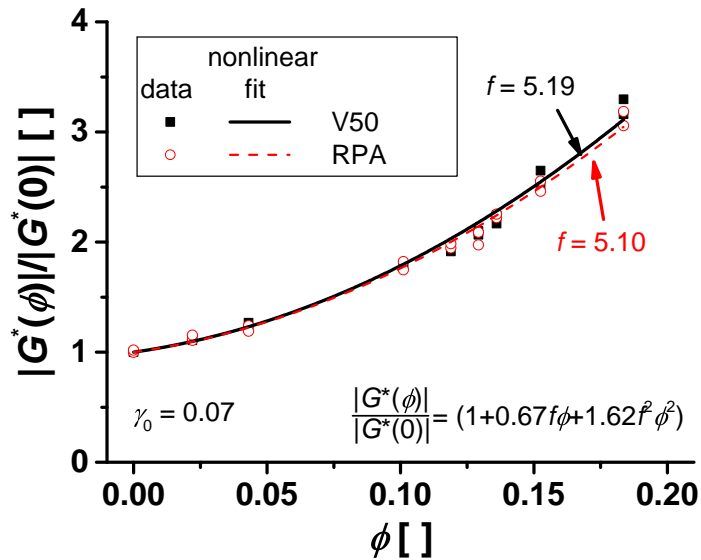


Figure 3.11.: Influence of the CB volume fraction ϕ on the absolute value of the shear modulus of E-SBR ($\gamma_0 = 0.07$, $\omega_1/2\pi = 0.5\text{Hz}$, $T = 100^\circ\text{C}$). The values of $|G^*(\phi)|$ are normalized to the value of the unfilled compound, $|G^*(0)|$. The data (symbols) measured on both instruments was fitted with the Guth equation (Eq. 2.28, p. 21) with $|G^*(0)|$ fixed to the respective value measured. The results of both instruments match well with $f = 5.19$ and 5.10 for the V50 and the RPA, respectively.

From this data it can be concluded that beside the difference in the absolute value of $|G^*(\phi)|$, the change of the modulus with increasing ϕ is the same for both instruments. The data was

fitted according to the Guth equation (Eq. 2.28, p. 21), with the anisotropy factor f as a free parameter. The anisotropy factor found was 5.19 and 5.10 for the V50 and the RPA, respectively. The calculated anisotropy factor deviates from the one found by Mullins and Tobin [82] of 6.5 for a rubber compound with a high abrasive furnace black, which is a CB grade similar to the N330 grade [10].

Figure 3.12 shows the nonlinear parameter $I_{3/1}$ as function of γ_0 during the LAOS test ($\omega_1/2\pi = 0.5$ Hz, $T = 100$ °C) for two samples with different CB volume fraction ($\phi = 0.0$ and 0.183) measured on the two rubber rheometers. At low strain amplitudes ($\gamma_0 < 0.01$), the value of $I(3\omega_1)$

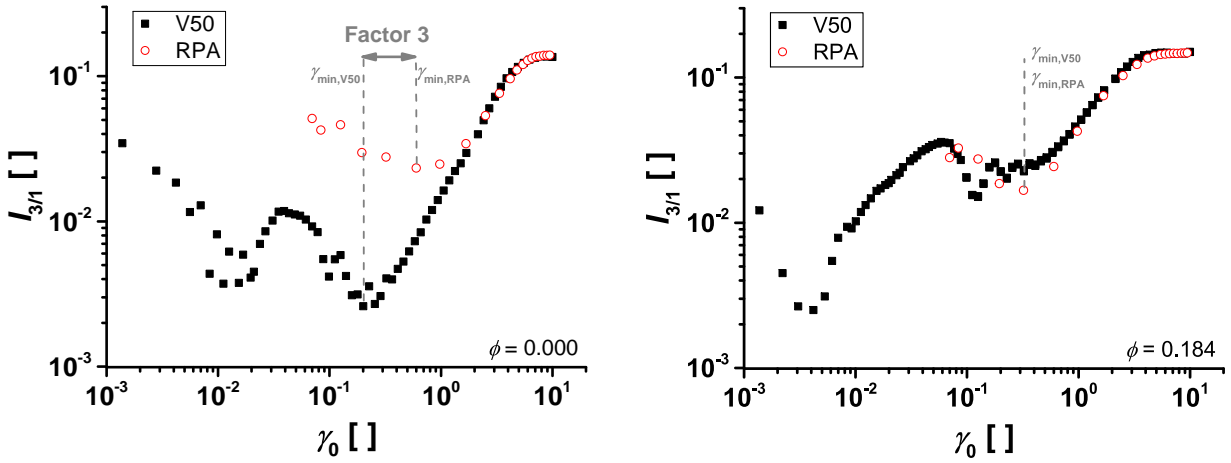


Figure 3.12.: Difference in $I_{3/1}$ as function of γ_0 between the V50 and the RPA during the LAOS test ($\omega_1/2\pi = 0.5$ Hz, $T = 100$ °C, average of two specimen). On the left, the sample without CB ($\phi = 0.0$) and on the right the sample with the highest amount of CB ($\phi = 0.183$) are shown. For the sample without CB, a huge difference is found at strain amplitudes below $\gamma_0 = 1$. The sensitivity of the RPA, defined as strain amplitude of the minimum in $I_{3/1}$, $\gamma_{min,RPA}$, prior to the onset of the scaling behavior is a factor of 3 lower than the sensitivity of the V50, $\gamma_{min,V50}$. For the highly filled sample, the data of the two instruments coincide over the whole range of γ_0 measured on both instruments ($\gamma_0 = 0.07$ to 10).

is dominated by noise (see Section 2.1.2) as can be seen by the decrease of $I_{3/1}$ with increasing γ_0 . Additionally, the data of the V50 shows a pronounced peak with a maximum around $\gamma_0 = 0.04$ and 0.06 for the two samples. This peak was discussed in the previous section (Section 3.2) and is most probably due to instrumental noise. At medium amplitudes ($\gamma_0 = 0.6$ to 1.7), $I_{3/1}$ can be described by a power law ($I_{3/1} \propto \gamma_0^m$) and eventually approaches a plateau value at $\gamma_0 > 5$.

For the sample with CB (right graph of Fig. 3.12), the data of the two instruments matches also quantitative very well over the whole range of strain amplitudes tested on the RPA. The

3. Performance of a rubber rheometer under LAOS

plateau value for both instruments is the same ($I_{3/1}(\gamma_0 = 8.9) = 14.7$) and the scaling exponent at medium amplitudes is similar ($m = 0.97$ and 1.09) for the V50 and the RPA. The difference in m is mainly due to the limited amount of strain amplitudes tested in this regime with the RPA. A quantitative difference between the rheometers for the filled sample is the value of $I_{3/1}$ at the minimum ($I_{3/1}(\gamma_{0,min})$), which differs by 36%. At this strain amplitude, the noise is in the same order of magnitude as the contribution of the nonlinear material response.

For the sample without CB (left graph of Fig. 3.12), the plateau values of the V50 and the RPA match ($I_{3/1}(\gamma_0 = 8.9) = 13.7$ and 13.9 , respectively) but the scaling exponent differ more ($m = 1.30$ (V50) and 1.13 (RPA)). The most important difference between the two instruments for this sample is the strain amplitude range in which $I_{3/1}$ is determined by noise (including the peak due to instrumental noise). The lower limit of this strain amplitude range differs by a factor of 3, i.e. the two rheometers have a different sensitivity for the measurement of higher harmonic contributions.

The strain amplitudes at the respective minimum of $I_{3/1}$, $\gamma_{min,V50}$ and $\gamma_{min,RPA}$, were chosen as a measure in order to quantify the difference in sensitivity. The absolute value of the minimum nonlinear harmonic contributions, which can be detected by each instrument, is approximated by the product of the torque and the relative third higher harmonic at this strain amplitude ($|M(\gamma_{min})| \cdot I_{3/1}(\gamma_{min})$). The results are given in Table 3.4. For the compound with CB, the

Table 3.4.: Sensitivity of different rheometers

| ϕ | Instrument | γ_{min} | $I_{3/1}(\gamma_{min})$ | $ M(\gamma_{min}) $ | $ M(\gamma_{min}) \cdot I_{3/1}(\gamma_{min})$ |
|--------|------------|----------------|-------------------------|---------------------|---|
| 0.000 | V50 | 0.20 | 0.0026 | 0.31 N m | 0.000 81 N m |
| | RPA 2000 | 0.60 | 0.0233 | 0.72 N m | 0.0168 N m |
| 0.183 | V50 | 0.32 | 0.0228 | 1.04 N m | 0.0237 N m |
| | RPA 2000 | 0.32 | 0.0167 | 0.84 N m | 0.0140 N m |

minimum of $I_{3/1}$ is found at the same strain amplitude ($\gamma_{min,V50} = \gamma_{min,RPA} = 0.32$) in both rheometers, which corresponds to similar torque values. The difference in the minimum nonlinear harmonic contributions is roughly a factor of two. For the sample without CB, $\gamma_{min,RPA}$ is three times larger than $\gamma_{min,V50}$. As a consequence, the V50 can detect ten times smaller nonlinear contributions than the RPA and $|M(\gamma_{min})| \cdot I_{3/1}(\gamma_{min})$ differs by a factor of 20.

The results measured for the two samples seem to be contradictory, as the sensitivity of the V50

is higher than the one of the RPA for the unfilled but lower for the filled sample. An explanation for this might be the high error in the quantitative determination of the sensitivity limit. This is mainly due to the limited amount of data points measured on the RPA at low strain amplitudes and hence $\gamma_{\min,\text{RPA}}$ can be determined less accurate than $\gamma_{\min,\text{V50}}$. It also seems that the instrumental noise has a large influence on the nonlinear measurement for the filled system, as the peak in $I_{3/1}$ at low γ_0 is wider and has a higher maximum value. It can not be inferred from the available data if the appearance of this peak is limited to the V50 or also present in the RPA and thus if this is a common feature of rubber rheometers, as the strain amplitude range measured on the RPA does not cover the same range as the one of the V50 rheometer.

The results of this study show, that with both rheometers the influence of the filler on the shear modulus can be measured equally. The V50 seems to be better suited than the RPA for the measurement of nonlinear contributions, especially for low viscous materials.

4. Synthesis of thermoplastic elastomers

4.1. Choice of model system

In filled rubbers, solid particles are added into the rubber matrix to improve the mechanical properties of the material (see Section 2.2). Polymer chains are adsorbed to the filler surface and thus create a three dimensional network in the polymer. At low filler contents (below the percolation threshold ϕ_c), the particles are isolated in the polymer matrix, which is a structure similar to the glassy phases in a TPE with a spherical morphology (Fig. 4.1). Therefore, this phase morphology

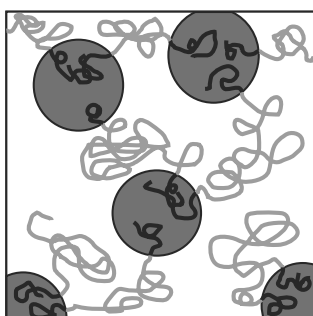


Figure 4.1.: Structure of an A–B–A triblock copolymer with A endblocks (black) forming spheres (dark grey) in a continuous matrix of the midblock B (light grey). Some diblock copolymers are also included because they are side products of the synthetic process.

was chosen for the TPEs used in this study, to have a model system for filled rubber materials below the percolation threshold. In this model system, the filler–polymer network of filled elastomers is resembled by a polymer–polymer network in the TPE. This network of the TPE is formed by polymer chains, which have endblocks in different spheres as well as by “trapped” entanglements of the middle blocks. Both, the network structure in the TPE and in the filled elastomer, have a dynamic structure caused by the thermal motion of the polymers.

Block copolymers can be synthesized by different methods. The most important ones are anionic, cationic, and controlled free radical polymerization [104, p. xiv]. For the important TPE type of A–B–A triblock copolymers with polydiene central units such as PI or polybutadiene [6, Chapter 2.19], anionic polymerization is the synthetic method of choice because the resulting poly-

diene units have high content of the 1,4-*cis* microstructure, if the reaction is carried out in apolar solvents and with lithium as the counterion [104, Chapter 2.1]. This microstructure is essential for the elastic properties and low T_g of polydiene materials and hence for the application of the TPE.

For the model system used in this study, polystyrene (PS) has been chosen as the thermoplastic compound and polyisoprene (PI) as the rubber part. Such poly(styrene-*b*-isoprene-*b*-styrene) triblock copolymers (SIS) are TPEs with a high industrial importance [122–124]. This polymer choice has the advantage that both monomers can be readily polymerized by anionic polymerization. For a poly(styrene-*b*-isoprene) diblock copolymer with a high fraction of 1,4-*cis* PI, Hashimoto and Fetters [125] reported the temperature dependence of the Flory-Huggins interaction parameter according to Eq. 2.31 (p. 26) from SAXS measurements of a diblock copolymer within a temperature range of 50 °C to 180 °C: $\chi = 38.54/T - 0.0419$. According to these results χ varies between 0.09 (20 °C) and 0.04 (200 °C) in the temperature range needed for rheological measurements in this study. The constraint for strong phase separation (by mean field theory, strong segregation limit) is $\chi N > 100$ [103]. This gives a minimum degree of polymerization of 1000 for the model systems. Under these conditions it can be seen from Fig. 2.10 (p. 27) that a spherical morphology is expected for a PS volume fraction $\Phi_{PS} = 0.05$ to 0.15.

4.2. Anionic polymerization of triblock copolymers

Anionic Polymerization is a ‘living’ polymerization, i.e. the polymerization process does not include an unavoidable termination reaction [126]. As a consequence, the active polymer chains, the anions, lose their reactivity only if an additional reagent is added. Such reagents are for example protic molecules (like water, alcohols or acids), carbon dioxide and oxygen. Thus contaminations of such molecules in the reaction system must be avoided. Therefore high vacuum techniques and Argon inert gas atmosphere were used. All solvents and reagents were degassed and dried prior to their use as described in Appendix A. The absence of inevitable termination reactions enables the synthesis of block copolymers with narrow molecular weight distributions (PDI typically below 1.1), defined block lengths and well-adjustable molecular weights [104, Chapter 1].

There are three main synthetic pathways for the anionic polymerization of A–B–A triblock copolymers: the sequential monomer addition, the coupling of two living diblock chains and the

use of a difunctional initiator [127]. All three approaches were used in this work in order to optimize the synthesis of SIS. In the following first some general considerations are mentioned, which are valid for all reaction carried out in this study, and second the three different pathways are explained in detail and the synthetic results are given and discussed. More information about the basic principles of anionic polymerization can be found in standard textbooks of polymer chemistry, e.g. [128–130].

4.2.1. General considerations

The polymerization is started using organic lithium compounds as initiator due to their low pK_a values, which enable the fast and complete metalation of most monomers used in anionic polymerization. This is necessary to get a narrow molecular weight distribution. Additionally, lithium as counterion has a positive effect on the 1,4-*cis* content of PI. In this study, *sec*-butyllithium (*s*-BuLi) was chosen due to its reactivity, which is high enough for a fast initiation of both isoprene and styrene in apolar, organic solvents. The initiation reaction of *sec*-BuLi with styrene is shown in Fig. 4.2. The product is a styryl anion with lithium as the counterion. The Li–C bond in organic

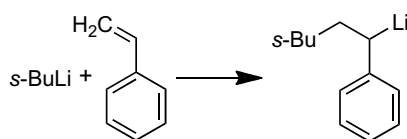


Figure 4.2.: Initiation of styrene with *sec*-butyllithium (*s*-BuLi). The product is a styryl anion (with lithium as counterion). The Li–C bond is between an ionic and a covalent (drawn here) bond.

lithium compounds is between an ionic and a covalent bond and these compounds tend to form larger oligomers with a reduced reactivity, especially in apolar solvents [131, Chapter 5.1]. Apolar solvents, such as benzene, cyclohexane, and toluene, are needed for the initiation step due to the subsequent polymerization of isoprene. Polar solvents like THF decrease the amount of the 1,4-*cis* isomer of PI [104, Chapter 1.1], which would be disadvantageous for the elastic properties of the final product. Therefore, either cyclohexane or toluene were used as solvent. An important parameter for the successful synthesis of A–B–A triblock copolymers in anionic polymerization is the relative reactivity of the two monomers and their respective anions. The carbanion of the first monomer used must be more reactive than the anion of the second monomer in order to initiate the second block [104, Chapter 1.1]. In apolar solvents, the reactivity of the polystyryl anion is larger than the one of the polyisopryl anion. Hence styrene has to be polymerized first. If styrene

needs to be polymerized after isoprene (e.g. third block in the sequential pathway or when using a difunctional initiator), the reactivity of the isoprene anion has to be increased by either increasing the reaction temperature or adding a polar additive like THF in order to have a fast and complete initiation of the styrene polymerization. All reactions were terminated by the addition of degassed methanol (MeOH) after the last reaction step.

4.2.2. Synthetic pathways used for the anionic synthesis of triblock copolymers

Coupling of Diblockanions

The reaction scheme for the synthesis of diblock copolymer anions and their subsequent coupling is depicted in Fig. 4.3.

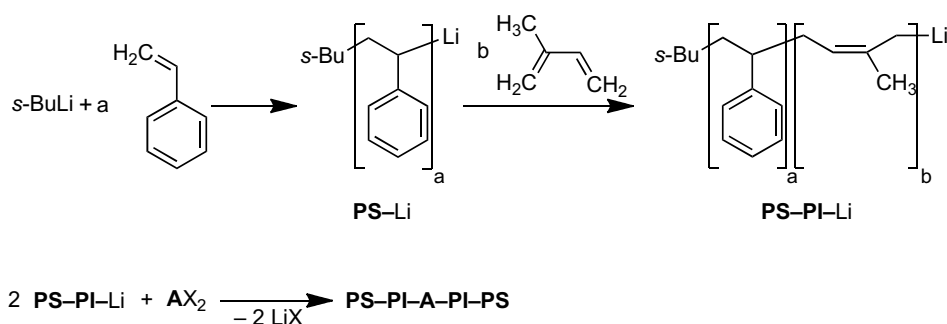


Figure 4.3.: Synthesis of SIS by the consecutive polymerization of styrene and isoprene followed by the coupling of living diblock anion chains with a coupling agent AX_2 . The polymerization is initiated by *s*-BuLi. The final triblock copolymer has a PS-PI-A-PI-PS structure.

First styrene is dissolved in toluene and the polymerization of the first block starts when *sec*-butyllithium is added. After complete conversion of the monomer, a sample of the reaction solution is taken for the analysis of the first block and isoprene is added. The polystyranion initiates the polymerization of the isoprene. When all monomer is used, another sample of the solution is taken and a coupling agent AX_2 is added. The coupling agent has two functional groups usually halogens that each can react with one diblock anion, forming the SIS triblock copolymer with a PS-PI-A-PI-PS structure. In the product, the coupling agent is between the two isoprene blocks and a *sec*-butyl group from the initiator is at each end.

In this synthetic pathway PS-PI diblock copolymer is a side product. The amount of diblock copolymer present in the final product depends largely on the efficiency of the coupling agent in the reaction. Additionally, the coupling agents has to be added in a stoichiometric amount to reduce

the amount of either residual living diblock anions or coupling agent with only one diblock chain attached. As the triblock has only double the molecular weight of the diblock, the separation of the two products by fractionation techniques is difficult. Under the assumption, that the molecular weight of the living anion does not affect its reactivity in the coupling reaction the triblock product should have symmetric endblocks on average. This assumption is fairly reasonable as the reaction solution was always very diluted (monomer to solvent volume ratio < 0.1).

Four different coupling agents, dichlorodimethylsilane, 1,2-bis(chlorodimethylsilyl)ethane, 1,5-dibromopentane, and diacetyl benzene, were tested in this study, which are shown in Fig. 4.4.

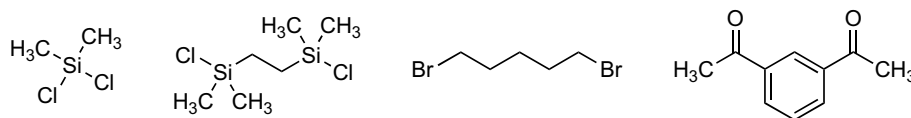


Figure 4.4.: Coupling agents AX_2 used in this study from left to right: dichlorodimethylsilane, 1,2-bis(chlorodimethylsilyl)ethane, 1,5-dibromopentane, and diacetyl benzene.

The coupling agent dichlorodimethylsilane was added stoichiometric to the reaction solution with a syringe after full conversion of the isoprene monomer. Each dichlorodimethylsilane molecule reacts at first with one living dianion and only after this, the second dianion is added. Therefore, the coupling agent was added dropwise in order to prevent an excess of coupling agent and thus ensure a complete reaction of the silane in the reaction mixture. The molecular weight distribution of the final product for one of the synthesized triblocks SIS-C1 (Fig. 4.5) reveals that the coupling reaction is incomplete under these conditions, given that the peak for residual diblock is larger than the peak of the wanted triblock at twice the molecular weight. The integral ratio of the two peaks is 40 % triblock and 60 % diblock. The ratio could be increased for a second polymer SIS-C2 to 53 % triblock, when the silane was added dropwise in two steps with 1 day stirring at room temperature in between. In order to increase the efficiency of the coupling reaction, in another test a small amount of THF was added to the reaction solution prior to the addition of the silane. The increasing polarity of the solvent should increase the reactivity of the diblock anion, but the amount of triblock in the final product could not be increased.

One possible reason for the low efficiency of dichlorodimethylsilane in the coupling reaction could be sterical hinderance after the first chloride ion is substituted by a diblock anion. Hence

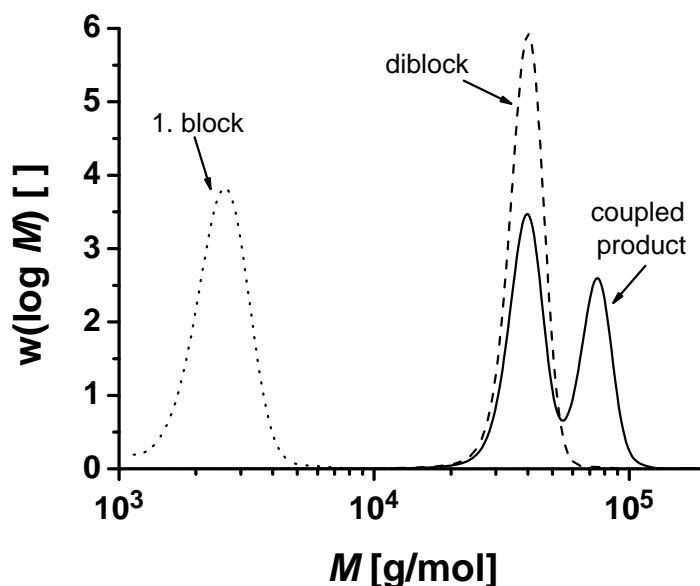


Figure 4.5.: Molecular weight distribution of the samples taken from SIS-C1, which was synthesized by the coupling of two diblock anions with dichlorodimethylsilane, after each step. After the first step (dotted line) a single low molecular weight peak indicates the formation of a polystyrene with $M_w = 2.6 \text{ kg mol}^{-1}$ and a PDI of 1.08. The peak is shifted to higher molecular weights ($M_w = 39.5 \text{ kg mol}^{-1}$, PDI = 1.03) after the diblock is formed (dashed line). The coupled product (full line) shows a peak with double the molecular weight of the diblock ($M_w = 75.0 \text{ kg mol}^{-1}$). The coupling reaction was not quantitative as can be seen by the additional pronounced diblock peak. The integral fraction of triblock in the product is only 0.4 (Solvent: THF, DRI).

1,2-bis(chlorodimethylsilyl)ethane was tested as coupling agent. Because of the additional ethylene unit the two chloride groups are further separated from each other, which should facilitate the substitution of the second chloride. Bis(chlorodimethylsilyl)ethane was dissolved in THF and added in two steps with 1 day in between. The integral ratio of the gained final product SIS-C3 is increased with this coupling agent to 65 % triblock and only 35 % diblock (see Fig. B.2).

1,5-Dibromopentane, where the halogen atoms are even further separated from each other than in bis(chlorodimethylsilyl)ethane, was found to be worse in terms of coupling efficiency, as no triblock polymer was found in the product.

1,3-Diacetylbenzene is a coupling agent, which does not contain halogens but two carbonyl groups. One anion can add at the C-atom of each carbonyl group and the oxygen gets negatively charged. After termination with MeOH a tertiary alcohol is gained. To evaluate this coupling agent, styrene was polymerized and no isoprene added afterwards. The solution was cooled down to -60°C to -80°C and a small amount of THF was added. The cooling was done in order to reduce the decomposition of the styrylanion by spontaneous termination in THF [129, Chapter 5-3b]. Then half

of the stoichiometric necessary amount of a diacetylbenzene solution in THF was added dropwise with a syringe, the other half 1 h later. 20 min after the second addition of diacetylbenzene, the cooling bath was removed. The reaction was terminated after another 3 h with degassed MeOH. The final product, S-C1, contained 30 % polystyrene with double the molecular weight than before according to the integral ratio in the GPC.

In summary, it was not possible to obtain pure triblock polymer by the coupling technique. The SEC of the synthesized polymers always revealed a large amount of remaining diblock. The highest triblock content was gained by using 1,2-bis(chlorodimethylsilyl)ethane dissolved in THF as coupling agent. After the stepwise addition of this agent, the integral of the two SEC peaks consisted to 65 % of triblock, which is equal to less than 50 mol%. For high contents of triblock copolymer the coupling agent needs to be added stoichiometric, which is hard to achieve due to termination of some living anions during all reaction steps. This termination, caused by either small amounts of contaminants like water and oxygen or by spontaneous termination in THF, could be detected by the presence of small amounts of polystyrene homopolymer in the SEC of the final product.

Difunctional initiator

The second method for the anionic polymerization of SIS presented here, is the use of a difunctional initiator. The advantages of this method are that the product is always symmetric in terms of molecular weight of the end blocks and only two monomer addition steps are needed [132, 133]. There are two main types of difunctional initiators for anionic synthesis [132–134]. These are the coupling of two radical anions [135] and the metalation of a precursor with two double bonds [132]. The difficulty of applying this synthetic method on SIS, is the low solubility of dicarbanionic species in apolar media [134, 136], which are needed for a high content of 1,4-*cis* PI. The precursor also needs a low ceiling temperature in order to prevent its polymerization [132]. Many suitable initiators have been proposed, most of them based on 1,3-diisopropenyl benzene (DIB) [132, 137], 1,3-bis(1-phenylethenyl) benzene (PEB) [138], 1,3-di[1-(methylphenyl)ethenyl] benzene (MPEB) [133, 138], and 3-pentadecyl phenol [136],

In this study DIB was used as precursor. DIB and *s*-BuLi were added to toluene in a 1:2 molar

ratio to form the difunctional initiator (Fig. 4.6). The successful formation of the difunctional

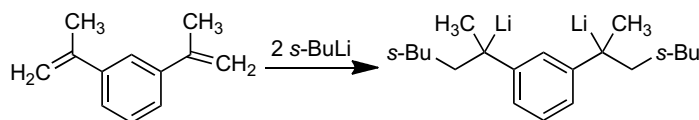


Figure 4.6.: Reaction of 1,3-diisopropenyl benzene with *sec*-butyllithium in toluene to the difunctional initiator.

initiator was indicated by an orange-red color of the solution. This was only possible, if the reaction was carried out at elevated temperatures (30 °C to 50 °C) for at least 1 h. This is consistent with the work of Yu et al. [139] that also reported the use of elevated temperatures to increase the reaction rate but in contrast to the findings of Beinert et al. [137], who successfully conducted the reaction at room temperature. In the next step of the reaction, isoprene was added to the solution. After the complete conversion of isoprene, THF was added to increase the reactivity of the isoprenyl anion and a small sample of the reaction solution was taken for further analysis of the first block. This was followed by the addition of styrene for the second polymerization step. Eventually the reaction was terminated by the addition of degassed MeOH after the complete conversion of styrene.

In Fig. 4.7 the results from size exclusion chromatography are shown for the sample SIS-D1 synthesized with the difunctional initiator in toluene. For the PI homopolymer sample, taken before the addition of styrene, the signal of the differential refractive index (DRI) detector shows a peak, which indicates the successful polymerization of isoprene with a molecular weight of $M_w = 56.0 \text{ kg mol}^{-1}$ (PDI = 1.07). This peak is shifted to a smaller elution volume, i.e. higher molecular weight, for the triblock copolymer SIS after the subsequent polymerization of styrene. The molecular weight of the SIS is $M_w = 61.4 \text{ kg mol}^{-1}$ (PDI = 1.07). In contrast to the PI, the SIS has a distinct peak in the signal of the UV detector, which corresponds to the presence of styrene units in the polymer.

The intended molecular weights were 100 kg mol^{-1} for the PI homopolymer and 130 kg mol^{-1} for the SIS. Given that the measured values are only half of the intended values, it seems that most probably *sec*-BuLi was still present and thus diblock copolymers were synthesized to a large extent. Beside the comparison of the calculated and the measured molecular weight, it is hard to determine whether a diblock or a triblock copolymer is obtained. NMR analysis does not give additional information because the aliphatic protons of PS and PI overlap with the protons of both butyl lithium and the difunctional initiator. The vinyl protons of DIB (if still present) are expected

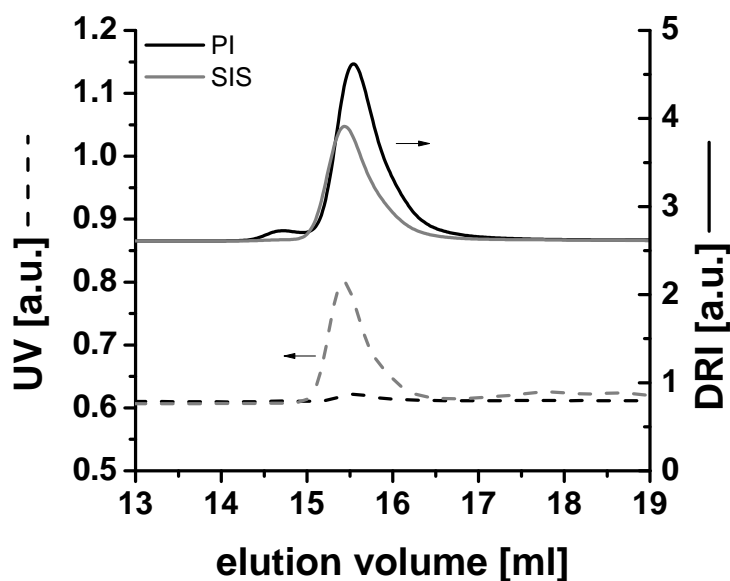


Figure 4.7.: Size exclusion chromatogram of SIS-D1 in THF synthesized with a difunctional initiator in toluene. The differential refractive index (DRI) detector (full lines) shows a decrease of the elution volume from the PI homopolymer (black) to the triblock copolymer (SIS, gray). This corresponds to an increase of the molecular weight from $M_w = 56.0 \text{ kg mol}^{-1}$ to $M_w = 61.4 \text{ kg mol}^{-1}$. In the UV signal (dashed lines) a considerable styrene content can be detected in the SIS in contrast to the PI homopolymer.

at $\delta = 5.2 \text{ ppm}$ (*cis*) and 5.4 ppm (*trans*, see Fig. B.7), which partly overlaps with the vinyl protons of PI at $\delta = 5.1 \text{ ppm}$.

To check if the formation of the difunctional initiator is quantitative, low molecular weight PS homopolymers were synthesized. The solution of *s*-BuLi and DIB in toluene was heated to 40°C for 1 h and 3 h before styrene was added and the PS homopolymers S-D1 and S-D2 were gained, respectively. The measured M_w values were 7.5 kg mol^{-1} and 7.0 kg mol^{-1} , which are considerably lower than the calculated value of 10 kg mol^{-1} . No vinyl protons could be detected in the NMR spectra of both polymers. This means that the reaction of *s*-BuLi and DIB was quantitative. Yu et al. [132, 139] found that beside the difunctional initiator, other polyfunctional species are formed during this reaction and that most of them react only as monofunctional initiators. This would explain the lower molecular weight of the synthesized polymers as well as the complete disappearance of the vinyl protons of the DIB species.

As a consequence, DIB was found not suitable as a precursor for the difunctional initiator. Alternative precursors proposed in the literature like PEB or MPEB have the same problem, which is that the created initiator is not completely difunctional but also mono- or polyfunctional [133, 138]

and parts of the monomer are initiated by *s*-BuLi. This problem can be circumvented only by the addition of polar additives like THF, which are disadvantageous for a high 1,4-*cis* PI content [133, 140], or by introducing a seeding step, i.e. the addition of a small amount of the first monomer in a step prior to its complete addition in order to increase the solubility of the initiator [135, 138, 140]. This last possibility negates the advantage of a two-step process for the difunctional initiator method.

In summary, the pathway using a difunctional initiator was not successful for the synthesis of SIS polymers.

Sequential monomer addition

This reaction scheme is the most straightforward method for the synthesis of triblock copolymers [141], but needs three monomer additions, which increases the probability of the termination of the polymerization by impurities [127, 133]. Another disadvantage is, that for the synthesis of triblock copolymers with symmetric endblock lengths, the amount of styrene added in the first and third polymerization step has to be exactly the same, providing that no chains are terminated during the whole reaction process. As side products polystyrene and poly(styrene-*b*-isoprene) are possible [104, Chapter 2.1].

The first two steps of the reaction (Fig. 4.8) are identical to the ones of the coupling approach. The

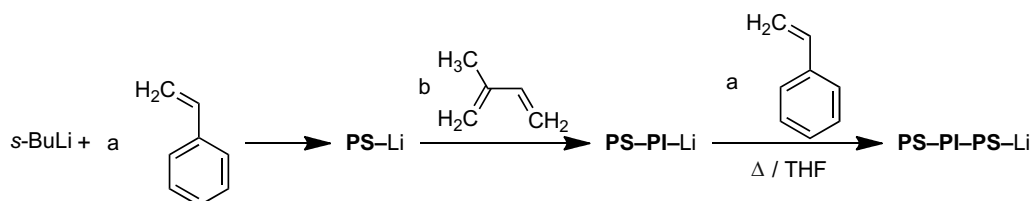


Figure 4.8.: Reaction scheme of the anionic synthesis of SIS by the sequential approach. First, styrene is polymerized with *s*-BuLi as initiator. After the subsequent polymerization of isoprene, styrene is added again to the solution of the living diblock anion solution. To start this third polymerization step, the reaction conditions have to be changed by increasing the temperature (Δ) or adding polar solvent (e.g. THF) prior to the styrene addition in order to increase the reactivity of the living isoprenyl anion. After the full conversion of styrene, the reaction is terminated with degassed MeOH and the triblock copolymer SIS is obtained.

polymerization of styrene is initiated by *s*-BuLi and a living polystyryl anion is formed. After the complete conversion of styrene, isoprene is added, which results in a diblock copolymer anion and the solution turns from orange to colorless. For the sequential polymerization another fraction of

styrene is added in the third step. In order to start this last polymerization step, the reactivity of the living diblock anion must be increased to initiate the final polymerization by either adding a polar solvent or increasing the reaction temperature prior to the styrene addition. After the complete conversion of styrene, the reaction is terminated by the addition of degased MeOH and the triblock copolymer is obtained. Samples of the reaction solution were taken after each polymerization step to investigate the change in molecular weight.

In order to increase the reactivity of the living diblock anion, THF was added prior to the second addition of styrene to increase the polarity of the solvent [104, Chapter 2.1], which was toluene. The resulting polymers showed no change in molecular weight between the diblock and the triblock polymer (e.g. sample SIS-S1, Fig. B.3), which indicates a high amount of termination during the polymerization of the third block. The reduction of the temperature during the last polymerization step to -60°C to -80°C , in order to decrease the spontaneous termination of the polymerization by THF, did not improve the results.

In another attempt, cyclohexane was used as a solvent, because toluene can act as a chain transfer agent [142]. Additionally instead of adding THF, the reaction temperature was increased to 60°C during the last polymerization step to increase the initiation rate of the diblock anion. With this, the polymers SIS-S2 and SIS-S3 were gained. As can be seen in the SEC data (Figs. 4.9 and 4.10), the major peak is shifted after each block and triblock copolymers with low polydispersity (PDI = 1.19) were gained.

It was not possible to quantify the amount of diblock in the product, as the difference in molecular weight between the diblock and the triblock is too small to get separated peaks in the SEC. The difference in M_w measured between the second and third sample is close to the expected shift due to the third block and NMR results prove the increase of the styrene content for SIS-S2 from 3.8% to 8.3%.

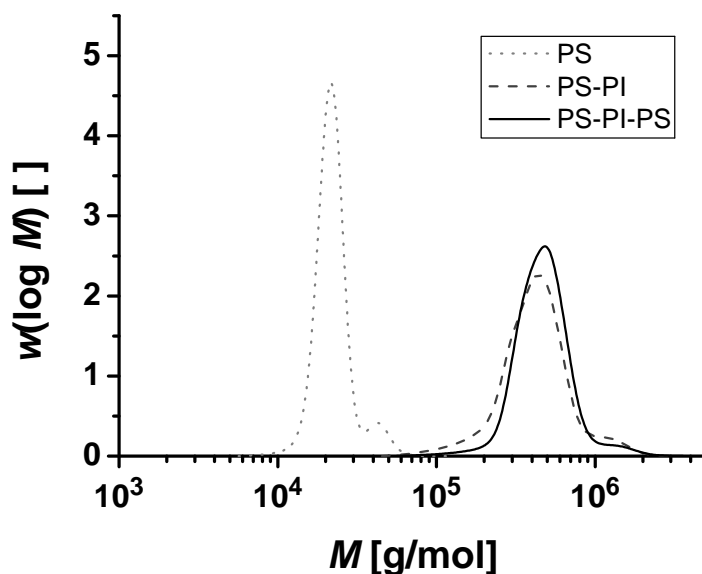


Figure 4.9.: Molecular weight distribution of the samples taken from SIS-S2, synthesized by the sequential addition of styrene, isoprene and styrene. After the first step (dotted line) a single low molecular weight peak indicates the formation of a polystyrene with $M_w = 23.1 \text{ kg mol}^{-1}$ and a PDI of 1.08. The peak is shifted to higher molecular weights ($M_w = 474 \text{ kg mol}^{-1}$, PDI = 1.32) after the diblock is formed (dashed line). In the final product (full line) the peak is further shifted to higher molecular weight ($M_w = 510 \text{ kg mol}^{-1}$, PDI = 1.19) (Solvent: THF, DRI detector).

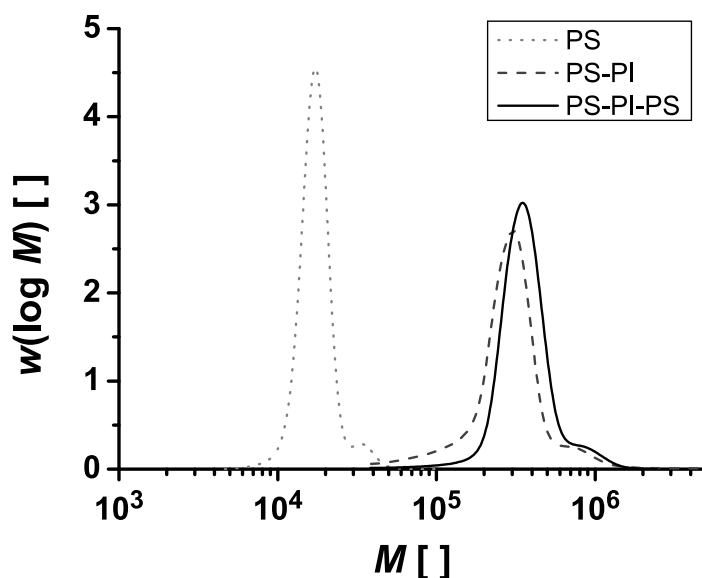


Figure 4.10.: Molecular weight distribution of the samples taken from SIS-S3, synthesized by the sequential addition of styrene, isoprene and styrene. After the first step (dotted line) a single low molecular weight peak indicates the formation of a polystyrene with $M_w = 18 \text{ kg mol}^{-1}$ and a PDI of 1.07. The peak is shifted to higher molecular weights ($M_w = 353 \text{ kg mol}^{-1}$, PDI = 1.46) after the diblock is formed (dashed line). In the final product (full line) the molecular weight is even higher ($M_w = 390 \text{ kg mol}^{-1}$, PDI = 1.19) (Solvent: THF, DRI detector).

5. FT rheology of thermoplastic elastomers

5.1. Samples

For the investigation of the nonlinear rheological behavior of thermoplastic elastomer (TPE) samples, three different poly(styrene-*b*-isoprene-*b*-styrene) copolymers (SIS) were used, one industrial sample from Kraton Polymers Belgium (SIS-I) and two samples (SIS-S2, SIS-S3) synthesized by sequential polymerization (Chapter 4). The composition of these sample is given in Table 5.1.

Table 5.1.: Summary of the analytic data for the three SIS triblock copolymers used for the rheological characterization. First, the number and weight averaged molecular weight (M_n and M_w , respectively) and the polydispersity index (PDI) of the three SIS samples are given (calculated from the SEC curve with a calibration for polyisoprene). The styrene and the isoprene content in mol% were measured by $^1\text{H-NMR}$ spectroscopy. The volume fraction of styrene, Φ_{PS} , was calculated with $\rho_{PS} = 1.05 \text{ g cm}^{-3}$ and $\rho_{PI} = 0.91 \text{ g cm}^{-3}$ [143].

| Sample | $M_{n,SIS}$ [kg mol $^{-1}$] | $M_{w,SIS}$ [kg mol $^{-1}$] | PDI | PS [mol%] | 1,4-PI [mol%] | 3,4-PI [mol%] | Φ_{PS} [vol%] |
|--------|----------------------------------|----------------------------------|------|--------------|------------------|------------------|-----------------------|
| SIS-I | 102 | 147 | 1.44 | 10.6 | 83.0 | 6.3 | 17.4 |
| SIS-S2 | 428 | 510 | 1.19 | 9.3 | 83.3 | 7.4 | 16.0 |
| SIS-S3 | 327 | 390 | 1.19 | 12.6 | 82.4 | 5.0 | 20.3 |

In order to determine the phase morphology of the three polymers, a method needs to be used, which is sensitive for typical sizes of microphase separation, i.e. 1 nm to 100 nm. Such methods include small angle X-ray scattering (SAXS), transmission electron microscopy (TEM) and small angle neutron scattering [144, Chapter 1.4]. The first two of these methods were used in this study.

In the following, the basic principle of determining the phase morphology of a block copolymer with SAXS is explained. For more details see textbooks about SAXS, e.g. [145–147].

The sample material is irradiated by an X-ray beam and typically the wavelength of the CuK_α radiation (1.5418 Å) is used [145, Chapter 2]. The incident beam is scattered at differences in the electron density $\rho(\vec{r})$. The scattering is predominantly elastic (Thomson scattering), whereas inelastic scattering (Compton scattering) can be neglected [145, 146]. If the electron density dif-

ference $\rho(\vec{r})$ has a regular structure along the position vector \vec{r} in the sample volume, a typical diffraction pattern is formed with an intensity $I(\vec{q})$, which is measured on a detector (in this study a two-dimensional CCD detector was used). This pattern is defined by the Bragg equation (Eq. 5.1)

$$n\lambda = 2d \sin \theta \quad (5.1)$$

The intensity of the scattered radiation $I(\vec{q})$ is the square of the scattering amplitude $|A(\vec{q})|$ (which is the Fourier-Transform of $\rho(\vec{r})$) (Eq. 5.3). Both are functions of the scattering wave vector \vec{q} , which is a function of the scattering angle θ (Eq. 5.2). The intensity $I(\vec{q})$ can be calculated as the product of the structure factor $S(\vec{q})$ and the form factor $P(\vec{q})$ (Eq. 5.3)

$$|\vec{q}| = \frac{4\pi \sin \theta}{\lambda} \quad (5.2)$$

$$I(\vec{q}) = P(\vec{q}) \cdot S(\vec{q}) \quad (5.3)$$

For a phase separated polymer, the form factor is given by the form of the repeat unit (e.g. sphere, cylinder, lamella), whereas the structure factor is defined by the arrangement of the repeat unit within the volume V (e.g. BCC, FCC, hexagonal). By inserting Eq. 5.2 in Eq. 5.1 the long period L , i.e. the distance between two repeat units, can be calculated by the position of the first peak ($n = 1$) in the diffraction pattern:

$$d = \frac{n\lambda}{2 \sin \theta} = \frac{n \cdot 2\pi}{\vec{q}} \quad (5.4)$$

$$L = \frac{2\pi}{|q_0|} \quad \text{for } n = 1 \quad (5.5)$$

In a system with a spherical morphology for example, L is equal to the distance between two spheres, in a lamellar system, L is the sum of the thickness of both layers. The scattering pattern of a structured polymer shows peaks for increasing n in Eq. 5.1 at multiples of the first peak q_0 . The positions of these higher peaks depend on $P(\vec{q})$ and $S(\vec{q})$ and thus are characteristic for each morphology. The positions of these characteristic peaks are given in Table 5.2 as multiples of the first peak q_0 for the different possible ordered microstructures shown in Fig. 2.10 (p. 27).

The intensity $I(\vec{q})$ is decreasing if defects are present in the structure, thus in weakly segregated

Table 5.2.: Peak positions in SAXS patterns normalized to the first order peak for the different morphologies of block copolymers (Figs. 2.10 and 2.11) [148].

| Morphology | Ratio q_n/q_0 |
|-------------------------|--|
| LAM lamella | 1, 2, 3, 4, 5, ... |
| HEX hexagonal cylinders | 1, $\sqrt{3}$, $\sqrt{4}$, $\sqrt{7}$, $\sqrt{9}$, ... |
| GYR gyroid | 1, $\sqrt{4/3}$, $\sqrt{7/3}$, $\sqrt{8/3}$, $\sqrt{10/3}$, ... |
| BCC spheres | 1, $\sqrt{2}$, $\sqrt{3}$, $\sqrt{4}$, $\sqrt{5}$, ... |
| FCC spheres | 1, $\sqrt{4/3}$, $\sqrt{8/3}$, $\sqrt{11/3}$, $\sqrt{12/3}$, ... |

samples only a few of these peaks with a low order might be identified [148]. Alignment of the sample by shear forces can increase the order within the sample and thereby increase the intensity [148]. The polydispersity has also an effect on the scattering intensity. The higher the PDI, the less pronounced are the different peaks [145].

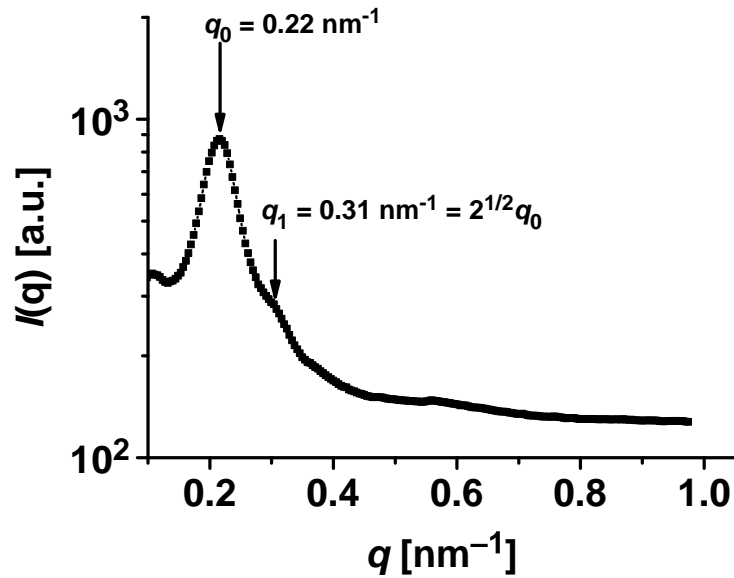


Figure 5.1.: SAXS pattern of the sample SIS-I (measured in a direction normal to the direction of the previously applied shear of 30 min at $\gamma_0 = 0.5$, $\omega_{1/2\pi} = 0.1$ Hz, $T = 160$ °C on ARES G2, SAXS measurement time: 60 s, 10 measurements were averaged). The first peak is found at $q_0 = 0.22$ nm⁻¹, which corresponds to a length of $L = 29$ nm. A second peak is found at $q_1 = 0.31$ nm⁻¹ which equals $\sqrt{2} \cdot q_0$.

For the sample SIS-I, the diffraction pattern is shown in Fig. 5.1. Only the first order peak at $q_0 = 0.22$ nm⁻¹ can be clearly identified. This corresponds to a long period of 29 nm. A shoulder of this peak corresponds to the second order peak at $q_1 = 0.31$ nm⁻¹. This correlates to $q_0 = \sqrt{2}q_0$, which means that SIS-I has a spherical morphology (BCC) as expected from its styrene content according to Fig. 2.10. The sample was sheared ($\omega_{1/2\pi} = 0.1$ Hz; $\gamma_0 = 0.5$, $T = 160$ °C, $t = 30$ min)

in order to enhance the phase separation, but this was not successful and no significant effect on the SAXS pattern was seen. The results for SIS-S2 and SIS-S3 are shown in the appendix (Fig. B.8 and Fig. B.9, respectively). Due to the lower PDI, the peaks of these two polymers are more pronounced, even though a lower measurement time was used compared to SIS-I. For SIS-S2 the first peak was found at $q_0 = 0.057 \text{ nm}^{-1}$, which corresponds to $L = 110 \text{ nm}$. Two further peaks can be identified at $q_1 = 0.081 \text{ nm}^{-1} = \sqrt{2}q_0$ and $q_3 = 0.119 \text{ nm}^{-1} = \sqrt{4}q_0$. The peak at $q_1 = \sqrt{2}q_0$ indicates a spherical symmetry, which corresponds to the styrene content ($= 16.0 \text{ vol}\%$). The peak at $q_2 = \sqrt{3}q_0$ could not be seen in this sample. The first peak of SIS-S3 is found at $q_0 = 0.086 \text{ nm}^{-1}$, i.e. $L = 73 \text{ nm}$. Another peak can be identified at $q_1 = 0.149 \text{ nm}^{-1} = \sqrt{3}q_0$. This peak indicates a cylindrical morphology. This sample has also a higher styrene content as the other two samples (20.3 vol%), which could explain the different morphology. A spherical BCC morphology is also possible, if the peak at $\sqrt{2}q_0$ is hidden below the peak at q_0 . In Table 5.3 the results of the small angle X-ray measurements are summarized for the three different SIS samples investigated.

Table 5.3.: Summary of the SAXS results for the three SIS triblock copolymers investigated.

| Sample | $\Phi(PS)$ [vol%] | N_{PI} | q_0 [nm^{-1}] | q_1 [nm^{-1}] | L [nm] | morphology |
|--------|----------------------|----------|-------------------------------|-------------------------------|-------------|------------|
| SIS-I | 17.4 | 134 | 0.22 | 0.31 | 29 | BCC |
| SIS-S2 | 16.0 | 571 | 0.057 | 0.081 | 110 | BCC |
| SIS-S3 | 20.3 | 420 | 0.086 | 0.149 | 73 | HEX |

The distance between the different repeating units, L , of a triblock copolymer should be determined by the size of the coiled structure of the middle block, which connects the repeat units. This coil diameter should be related to the radius of gyration $\langle R_G \rangle$ of the PI middle block. For the simple model of a Gaussian chain with a random orientation of each monomer unit, the square of the radius of gyration is given by Eq. 5.6

$$\langle R_G \rangle_{PI}^2 = \frac{N_{PI} \cdot l_{PI}^2}{6} \propto N_{PI} \quad (5.6)$$

In this equation, N_{PI} is the degree of polymerization of the PI block and l_{PI} the length of one PI monomer unit. Thus the long period should scale with $L \propto N_{PI}^{1/2}$. In contrast to this, the measured ratio between the different distances L of the three samples SIS-I, SIS-S2 and SIS-S3 (29 nm, 110 nm and 73 nm) is proportional to the degree of polymerization $N_{PI} = 134, 571$ and 420 . This might

be explained by the very simple model of a Gaussian chain with free orientation of the chains used for Eq. 5.6, which ignores for example the restricted bond angles in real polymer molecules. Additionally, diblock polymers present in the polymers would also affect L .

For the sample SIS-I, a transmission electron micrograph was also recorded. The polymer granulate was formed into a circular disk with a thickness of approximately 1 mm by using a heated press. The subsequent sample preparation (microtomic cut at -180°C) and the measurement were done at Continental Reifen Deutschland in Hannover. The image of the sample is shown on the left of Fig. 5.2.

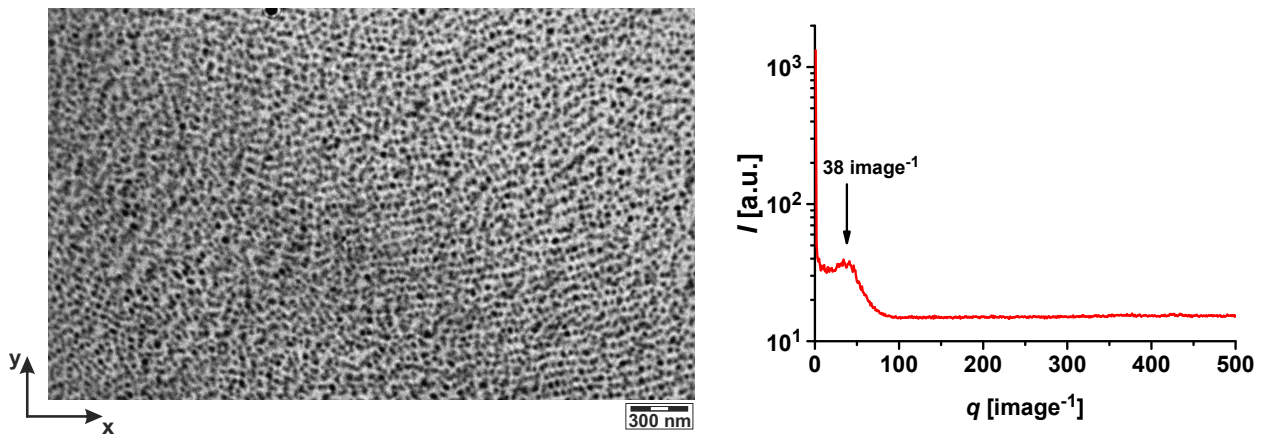


Figure 5.2.: Cryo-STEM image of the sample SIS-I without shear alignment (left). The sample was microtomic cut at -180°C and measured by Continental Reifen Deutschland GmbH (HAADF, 100 keV). From this image, a FT spectra of the gray scale in y-direction was calculated for every position in the x-direction. These spectra were then averaged and the resulting spectrum is given on the right. In this spectrum a peak at approximately 38 waves/image , which corresponds to a length of $= 60 \text{ nm}$, can be identified.

This image was analyzed via a Fourier-Transform of the gray scale along the y-axis for every line in x-direction. The different FT-spectra calculated by this method were then averaged. The averaged spectrum is shown on the right of Fig. 5.2. A characteristic peak at 38 waves/image was found. The total length of the image in y-direction corresponds to 2664 pixel and the scale is $300 \text{ nm} = 349 \text{ pixel}$. Hence the characteristic peak of the FT-spectrum indicates a distance between the centers of two repeating units of 60 nm . This is twice as high as the characteristic length determined by SAXS ($L = 29 \text{ nm}$), however L is just the distance between two spheres.

The three SIS samples were also investigated by dynamic scanning calorimetry (DSC). For phase-separated block copolymers, a glass transition of each polymer phase should be expected [149]. In Fig. 5.3 the results for the triblock copolymers are given. For all three samples, the glass transition

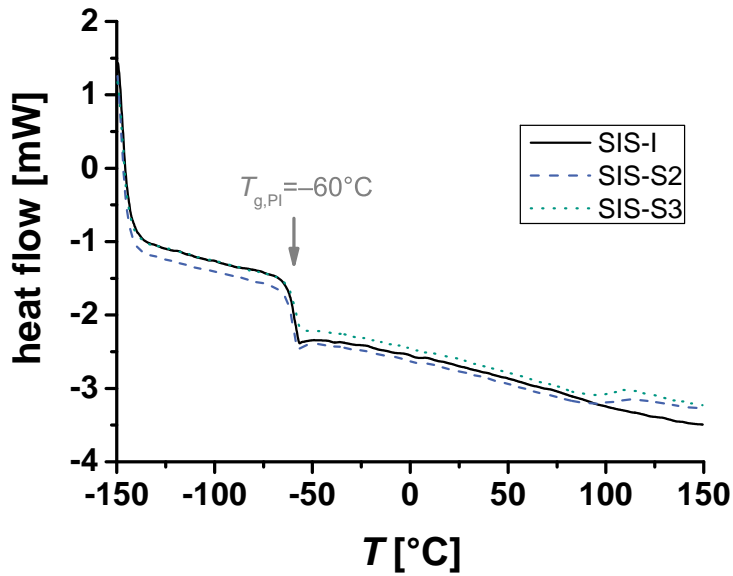


Figure 5.3.: Results from DSC measurement of the three triblock copolymers. The glass transition temperature for the PI phase was found at $T_{g,PI} = -60.1\text{ }^{\circ}\text{C}$, $-61.0\text{ }^{\circ}\text{C}$ and $-59.7\text{ }^{\circ}\text{C}$ for SIS- I, SIS-S2 and SIS-S3, respectively (results from second heating run shown, heating rate = 10 K min^{-1}). No glass transition of the polystyrene phase is observed.

temperature of the PI was found at $T_{g,PI} = -60\text{ }^{\circ}\text{C} \pm 1\text{ }^{\circ}\text{C}$. Although a phase separation was detected by SAXS for all three polymers and by TEM for SIS-I, no glass transition temperature of the polystyrene was found. The signal of the glass transition is most probably only very weak due to the low PS volume fraction, the low PS block length and the relatively high PDI of the triblock copolymers ($\text{PDI} \geq 1.19$) and thus could not be detected.

5.2. Rheological measurements

All rheological measurements of the three SIS triblock copolymers were performed using a ARES G2 rheometer. In Fig. 5.4, the linear master curve of the sample SIS-I is shown for a reference temperature $T_{\text{ref}} = 120\text{ }^{\circ}\text{C}$. The sample displays a broad rubber plateau at frequencies above $a_T\omega_1 = 2.5\text{ rad s}^{-1}$. The longest relaxation time τ corresponds to the crossover of G' and G'' and was determined as $\tau = 0.4\text{ s}$. At lower frequencies ($a_T\omega_1 < 2.5\text{ rad s}^{-1}$) G' is smaller than G'' but no terminal behavior is seen, i.e the power law behavior for a fluid following the Maxwell model ($G' \propto \omega_1^2$, $G'' \propto \omega_1^1$) was not found. This feature, the presence of a second transition zone at frequencies smaller than those of the rubber plateau, is a typical finding for phase separated block

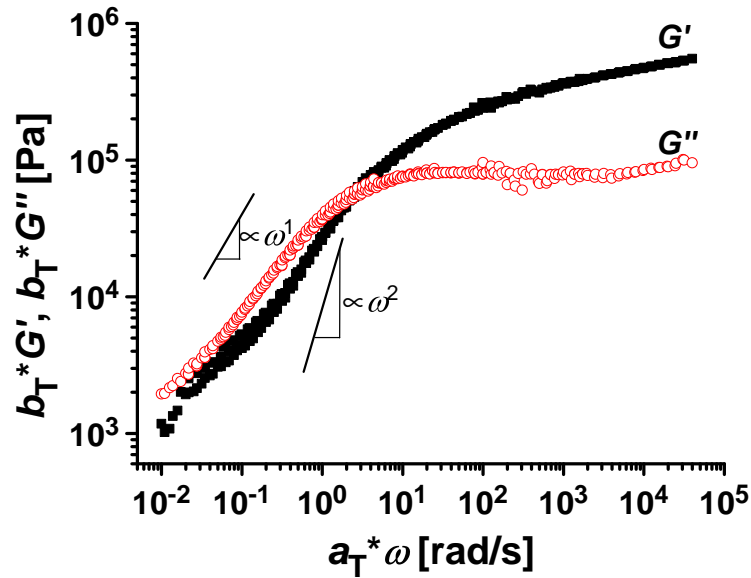


Figure 5.4.: Master curve of SIS-I at $T_{ref} = 120\text{ °C}$ measured at frequencies between $\omega_{1/2\pi} = 0.05\text{ Hz}$ to 20 Hz at $T = 80\text{ °C}$ ($\gamma_0 = 10^{-4}$), $T = 100\text{ °C}$ ($\gamma_0 = 10^{-3}$), $T = 120\text{ °C}$ ($\gamma_0 = 0.01$), $T = 140\text{ °C}$ ($\gamma_0 = 0.05$), $T = 160\text{ °C}$ and 180 °C ($\gamma_0 = 0.1$) on the ARES G2 (13 mm, plate-plate, Invar). The sample was always measured twice at each temperature.

copolymers below the order-disorder-temperature T_{ODT} [102, 150–152]. The T_{ODT} is the temperature at which the polymer changes from a phase separated state to a homogeneous melt. For $T < T_{ODT}$, the free movement of the chains is restricted by the phase separation and hence the relaxation of the chain by reptation is hindered [150, 153].

The time-temperature superposition principle, which is the basis for calculating the master curve, is valid only for thermorheologically simple samples such as homopolymers [151] and thus its applicability for a phase separated polymer is not necessarily justified, especially below the glass transition temperature of the high T_g -compound [151, 154], which is in this work PS with an expected glass transition temperature of $T_{g,PS} \approx 100\text{ °C}$, even though no glass transition was found for polystyrene in the DSC measurements (see Fig. 5.3). For the SIS-I, the horizontal and vertical shift factors, a_T and b_T used for the master curve are shown in Fig. 5.5. The shifting was done automatically by the software of the ARES G2 (TRIOS). The horizontal shift factors a_T do follow the equation of Williams, Landel and Ferry (WLF-equation, Eq. 5.7), which contains beside the reference temperature T_{ref} , two additional, empirical parameters, C_1 and C_2 , which were 4.43 and

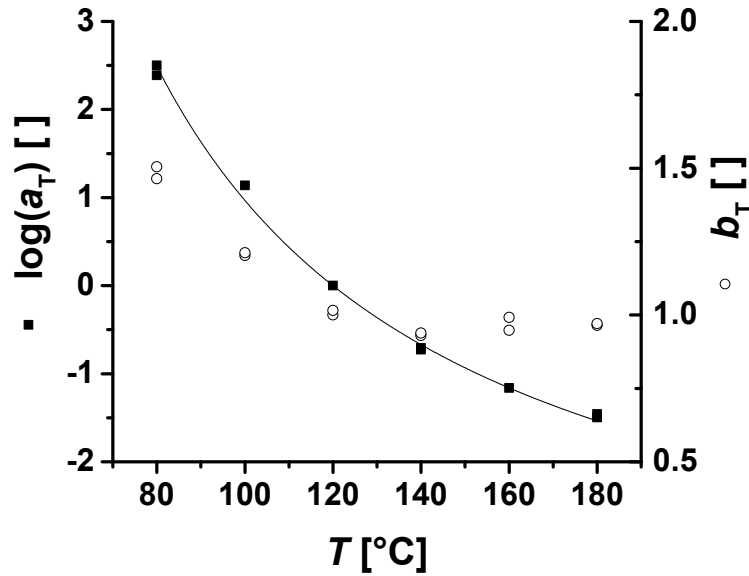


Figure 5.5.: Horizontal and vertical shift factors $\log a_T$ (full squares) and b_T (open circles), respectively as function of the temperature ($T_{ref} = 120^\circ\text{C}$) for the linear master curve for SIS-I shown in Fig. 5.4. The horizontal shift factors follow the WLF-equation Eq. 5.7 (line) with $C_1 = 4.43$ and $C_2 = 111.2\text{K}$.

111.2K, respectively for the SIS-I.

$$\log a_T = \frac{-C_1(T - T_{ref})}{C_2 + T - T_{ref}} \quad (5.7)$$

The vertical shift factors should only depend on the change of the sample density [154]. For the block copolymers, the exact temperature dependence of the density is estimated to be in the range of a few percent in the temperature range observed. Therefore, b_T should be close to one. This is the case for temperatures above $T_{ref} = 120^\circ\text{C}$ but not for those below. These temperatures (80°C and 100°C) are close to the T_g of the polystyrene. It can be concluded, that close to the T_g of polystyrene the validity of the TTS principle seems to be restricted and additional vertical shifting is needed in order to achieve a master curve.

The storage modulus of the sample SIS-S2 during a LAOS strain amplitude test is plotted in Fig. 5.6 as function of the strain amplitude at $T = 120^\circ\text{C}$ for six different angular frequencies from $\omega_1 = 1\text{ rad s}^{-1}$ to 10 rad s^{-1} . For the LAOS strain amplitude test, the average value and standard deviation of G' calculated from three different measurements at each angular frequency are given. It can be seen, that the storage modulus starts to decrease from its plateau value at strain amplitudes of $\gamma_0 > 0.1$ for all frequencies. The most striking feature of this graph is the large error

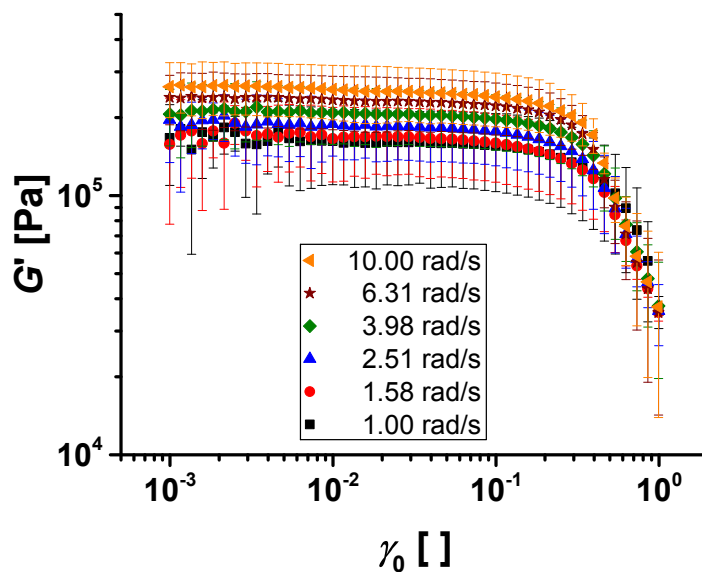


Figure 5.6.: Storage modulus of sample SIS-S2 at 120 °C at six different angular frequencies on the ARES G2 (10 mm partitioned plate geometry or a 13 mm parallel plate geometry). The nonlinear viscoelastic regime starts at strain amplitudes $\gamma_0 > 0.1$.

of the modulus values as indicated by the error bars, which was found for most of the measurements on the TPE samples. A reason for this large error might be related to the complex heterogeneous structure of the sample due to the phase separation. During the sample preparation (pressing the specimen into a circular disc with a hot press for approximately 30 min at 180 °C) a different degree of orientation of the styrene phase can be introduced by slight differences in the process. It is known from literature [148, 155] that phase separated polymers can be partially oriented by external forces. The specimen also might be for example slightly bend during its alignment on the rheometer geometry and hence an orientation of the morphology could be introduced, which differs from other specimen. Such problems could be avoided if the sample is heated above its order-disorder transition temperature, where the phases get disordered, and eventually cooling of the sample to the measurement temperature. For all three samples no T_{ODT} was found within the measurement range (up to 200 °C). Another possible reason for the large error in the measurement could be slip at the geometry surface.

The corresponding results for $I_{3/1}(\gamma_0)$ are shown in Fig. 5.7. At small strain amplitudes ($\gamma_0 < 0.005$) the signal is dominated by noise, as can be seen by the decrease of $I_{3/1}$ with increasing strain amplitude and the large error bars. Between $\gamma_0 = 0.005$ to 0.05, a peak of $I_{3/1}$ is found with a

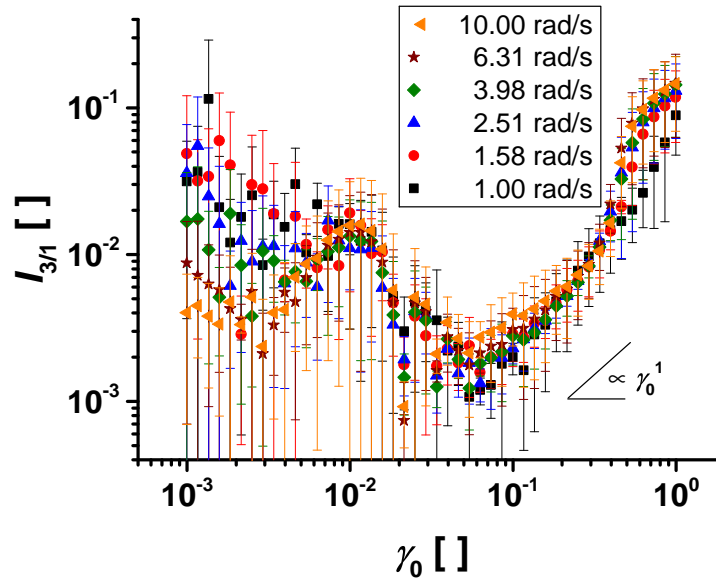


Figure 5.7.: Nonlinear parameter $I_{3/1}$ of the sample SIS-S2 at 120 °C at six different angular frequencies measured on the ARES G2 (10 mm partitioned plate geometry or a 13 mm parallel plate geometry). Up to a strain amplitude of $\gamma_0 = 0.05$ the signal is dominated by noise. In this regime, a peak of $I_{3/1}$ could be seen, similar to the one measured on the V50 (Section 3.2). This is followed by a region where $I_{3/1}$ can be described by a power law, but the slope is below 1. Above a strain amplitude of $\gamma_0 = 0.5$ the nonlinear contribution $I_{3/1}$ is strongly increasing (except for $\omega_1 = 1 \text{ rad s}^{-1}$), having values above 0.01 in $I_{3/1}$.

maximum around $\gamma_0 = 0.01$. This peak looks similar to the one usually measured on the V50 (see Section 3.2). This peak was found on the ARES G2 only for this sample and at this temperature for two of the three specimen tested. Up to now it is unclear, whether there is a connection between this peak and the one seen in results of the V50 or not. At larger strain amplitudes ($\gamma_0 > 0.05$), $I_{3/1}$ starts to increase with γ_0 and follows a scaling law with an exponent smaller than one. The data of all angular frequencies are within the error of one measurement, which is also very high for the nonlinear parameter. At strain amplitudes above $\gamma_0 = 0.5$, the increase of $I_{3/1}$ is more pronounced, which is most probably due to slippage of the sample. Edge effects can be excluded, because two of the three measurements of the sample were done with a so called partitioned plate geometry [156]. This geometry is designed to prevent edge fracture. The upper part of the geometry is divided into two radial parts and only the inner part (diameter=8 mm or 10 mm) is connected to the torque transducer, while the outer part is fixed. No significant differences between the partitioned plate and the 13 mm parallel plate geometry were found. Additionally, SAOS frequency tests ($T = 120 \text{ °C}$, $\gamma_0 = 0.02$) before and after the LAOS amplitude tests showed no significant deviation, i.e. no permanent destruction of the sample was found.

In order to further investigate the influence of temperature and angular frequency on $I_{3/1}$ of the triblock copolymers, two different strain amplitudes within the power law region were chosen ($\gamma_0 = 0.1$ and 0.4). The nonlinear parameter $I_{3/1}$ at these strain amplitudes is plotted as function of ω_1 for different temperatures in Fig. 5.8.

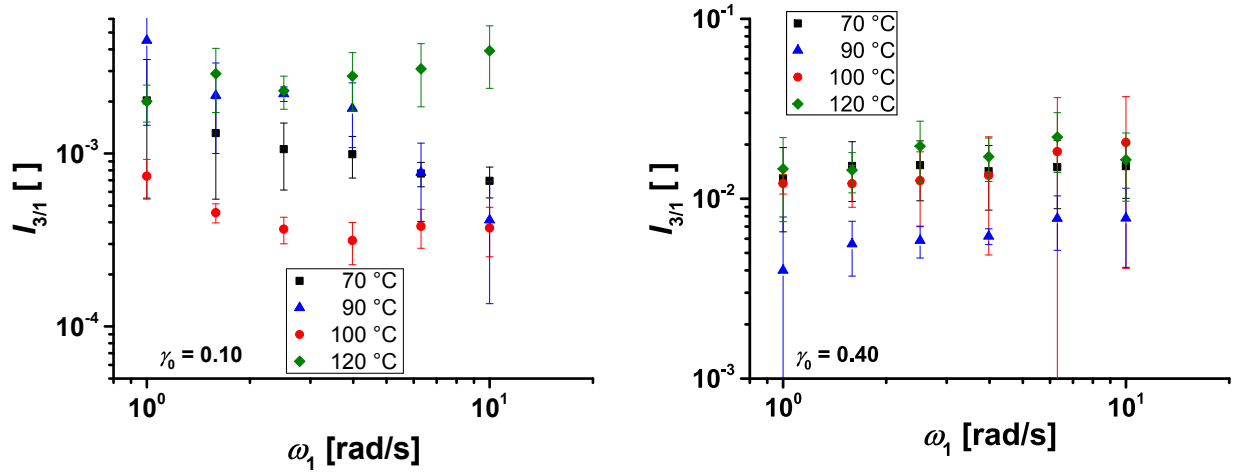


Figure 5.8.: Nonlinear parameter $I_{3/1}$ of the sample SIS-S2 at $\gamma_0 = 0.1$ and 0.4 as function of ω_1 at various T measured on the ARES G2.

At $\gamma_0 = 0.4$ no influence of ω_1 or T can be seen. Only the results at 90 °C are somewhat lower but still within the error range. At $\gamma_0 = 0.1$, the results for various T show a large deviation and no clear trend can be seen for the frequency dependence. Only the sample at $T = 90\text{ °C}$ shows a significant frequency dependence. For all measurements, the sample is in the rubber plateau, i.e. $G' > G''$.

6. FT-Rheology of carbon black filled solution

SBR

The influence of solid, reinforcing particles, namely carbon black (CB), on the nonlinear rheological properties of rubber was investigated in the following sections. As was already discussed in Section 2.2.3 (p. 19), the addition of CB has a large influence on the mechanical properties of rubber, such as the Payne and the Mullins effect, and the underlying physical mechanisms are not yet fully understood. Nonlinear contributions can give additional information about the samples measured, which is not captured in the linear modulus. In contrast to findings of other researchers, who discovered only marginal higher harmonic contributions even at strain amplitudes of $\gamma_0 = 1$ for filled rubbers [16, 92], the results presented in the following sections clearly show that these higher harmonic contributions are not negligible at strain amplitudes $\gamma_0 > 0.1$ and that they can help to improve the understanding of composites under shear deformation. This chapter is divided in two sections. In the first section, filled, unvulcanized styrene butadiene rubber (SBR) is investigated with special focus on the effect of filler content, particle shape, and measurement temperature on the nonlinear parameter $I_{3/1}$. Most of the results shown in this section were published in [157] and hence most of the figures are reproduced with permission from Wiley-VCH. In the second section, the vulcanization process of these samples and their properties after vulcanization are investigated by FT-Rheology.

6.1. Influence of carbon black on unvulcanized rubber

The compounds used in this study were prepared by Continental Reifen Deutschland (Hannover) and received in form of flat sheets. The samples consisted of a polymer matrix of a solution styrene

butadiene rubber (S-SBR) with 15.8 mol% ($\hat{=}$ 29.3 wt%) styrene, 29.9 mol% 1,2- and 54.3 mol% 1,4-butadiene. The (weight averaged) molecular weight was $M_w = 398 \text{ kg mol}^{-1}$ and the PDI 1.83. Standard anti-aging additives (6 phr) were added to increase the longterm stability of the samples. A curing system (7.35 phr) was also included to enable the investigation of the vulcanization of the rubber and to resemble samples used in industry. Carbon black was used as a solid filler and the filler loading was varied between 0 phr to 70 phr. The corresponding CB volume fractions, ϕ , were calculated by literature values of the densities for the different constituents and ranged from $\phi = 0$ to 0.242. The preparation of such compounds is complicated, due to the high amount of ingredients and the need for a good dispersion of these ingredients in the polymer. Thus only a limited amount of different compounds (21) could be investigated during this work.

As filler three different ASTM-grades of CB were used: N121 (4 samples), N339 (13 samples), and N660 (4 samples). Details of the standard CB classification system and the corresponding nomenclature of the different grades as defined by the ASTM International are given in Section 2.2.1 (p. 15). N121 is a highly reinforcing grade with a high specific surface area, whereas N660 consists of primary particles with a large diameter and has a low NSA value. N339 is somewhere in between the two other grades. In Table 6.1, the main physical characteristics of the fillers are listed.

Table 6.1.: Structural properties of the carbon black grades used. Data received from Continental Reifen Deutschland.

| Grade | NSA ^a | OAN ^b | COAN ^c |
|-------|-----------------------------------|---------------------------|---------------------------|
| | [m ² g ⁻¹] | [ml(100g) ⁻¹] | [ml(100g) ⁻¹] |
| N121 | 122 | 132 | 111 |
| N339 | 91 | 120 | 99 |
| N660 | 35 | 90 | 74 |

^a NSA: nitrogen surface area (ASTM D6556)

^b OAN: oil adsorption number (ASTM D2414)

^c COAN: crushed oil adsorption number (ASTM D23493)

In Fig. 6.1, transmission electron micrographs of the three CB grades are shown, illustrating their structural differences.

The state of the macro dispersion of the CB in the matrix (i.e. the number of CB agglomerates

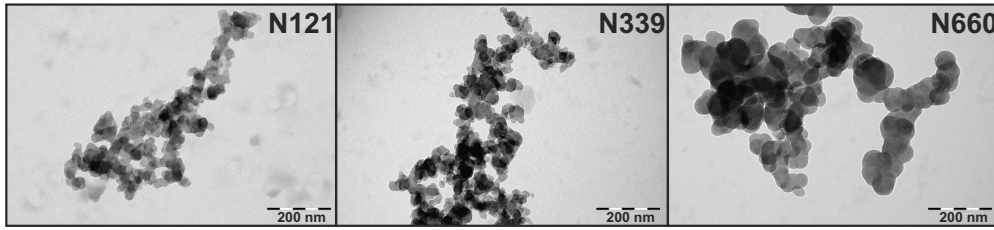


Figure 6.1.: TEM pictures of the three different CB particles (N121, N339, N660) used in this study, measured by Continental Reifen Deutschland. N121 is a CB with small primary particles and has a high structure, i.e. many small voids and a rough surface. N660 consists of large primary particles with low structure and nearly no small voids. The morphology of N339 is in between the two others.

larger than $5\ \mu\text{m}$) was analyzed with a disperGrader (Alpha Technologies, Akron, OH) and was above 97% for all compounds used in this work.

6.1.1. Measurement of the electrical percolation threshold by dielectric relaxation spectroscopy

The conductivity of the different CB filled SBR compounds was measured in order to find the electrical percolation threshold. The matrix of the samples consisted of an insulating rubber and different amounts of conductive CB were added. At low concentrations of CB, the CB aggregates and agglomerates are separated from each other by a layer of the insulating rubber and the DC-conductivity of the compound corresponds to the conductivity of the matrix. At volume fractions above the percolation threshold ϕ_c , the network formed by the CB agglomerates is continuous through out the sample, at least in terms of electrical conductivity (see also Section 2.2.2). This means that the distance between different CB agglomerates is low enough to enable the tunneling of electrons, which is typically below 5 nm [76]. This results in a strong increase of the electrical conductivity by several orders of magnitude [71]. If the filler content is further increased, the conductivity levels off and forms a plateau in the so called conductive regime.

To determine the percolation threshold, the different samples were measured by dielectric relaxation spectroscopy. An alternating electrical current (AC) was applied to a home-made dielectric geometry (diameter of 13 mm) built into an ARES LS rheometer (TA Instruments) with an Alpha Single Unit Analyzer (Novocontrol Technologies, Montabaur, Germany) as described in [158]. The frequency range of the applied AC was $\nu_{AC} = 10^{-2}\ \text{Hz}$ to $10^6\ \text{Hz}$. The electrical excitation induces an electrical field in the sample, which is measured by the set-up. Typical spectra of the resulting

absolute value of the AC-conductivity $|\sigma_{AC}|$ are displayed in Fig. 6.2 for the samples filled with $\phi = 0.084$ and $\phi = 0.215$ N121 CB. The (root mean square) voltage of the applied current was

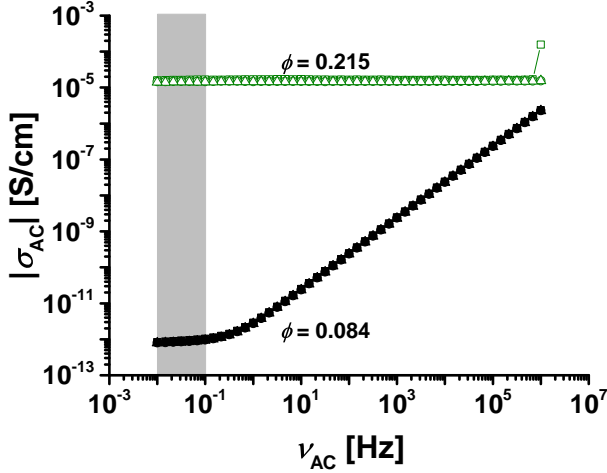


Figure 6.2.: Absolute value of the AC-conductivity $|\sigma_{AC}|$ as function of the frequency of the electrical current (ν_{AC}) for the S-SBR filled with $\phi = 0.084$ and $\phi = 0.215$ N121 CB, measured at $T = 60^\circ\text{C}$ with a voltage of $U_{\text{RMS}} = 0.5\text{V}$. The extrapolated DC-conductivity $|\sigma_0|$ was calculated by the AC-conductivity $|\sigma_{AC}|$ at low frequencies ($\nu_{AC} = 10^{-2}\text{Hz}$ to 10^{-1}Hz , gray area).

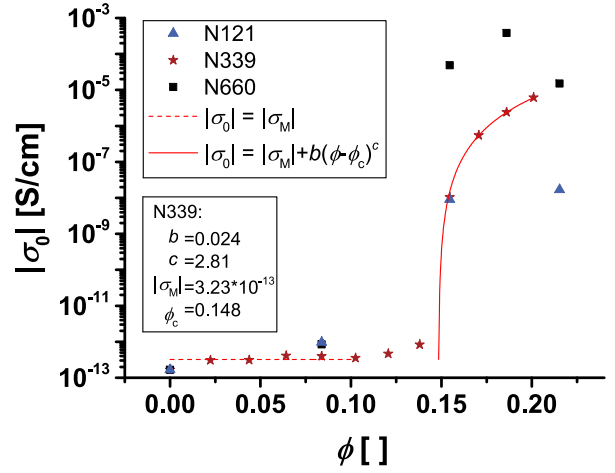


Figure 6.3.: Conductivity $|\sigma_0|$ as function of ϕ ($T = 60^\circ\text{C}$). At low CB volume fractions ($0 < \phi < 0.12$) the conductivity is low (for N339: $|\sigma_M| = 3.2 \cdot 10^{-13}\text{S cm}^{-1}$, dashed line). For $\phi > \phi_c$, the conductivity increases by several orders of magnitude and finally levels off. The height of the plateau at high ϕ differs by four orders of magnitude between the grades. For the N339 CB a percolation threshold $\phi_c = 0.148$ was calculated by Eq. 6.1 (full line).

$U_{\text{RMS}} = 0.5\text{V}$. A specimen of each sample was measured three times. From these spectra the DC-conductivity $|\sigma_0|$ was approximated as the plateau value of the AC-conductivity $|\sigma_{AC}|$ at low frequencies ($|\sigma_0| = \text{average of } |\sigma_{AC}| \text{ between } \nu_{AC} = 10^{-2}\text{Hz}$ to 10^{-1}Hz , gray area). The filler particle size and structure has a strong influence on the percolation threshold [71, 159], but also the state of dispersion can influence the conductivity [74]. The effect of the filler volume fraction and the CB grade can be seen in Fig. 6.3, where the absolute value of the electrical conductivity $|\sigma_0|$ is plotted as function of the filler content. At low CB volume fractions ϕ , the conductivity of the samples is low and corresponds to the conductivity of the polymer matrix without CB. The conductivity of the matrix, $|\sigma_M| = 3.2 \cdot 10^{-13}\text{S cm}^{-1}$, was calculated by a linear fit with slope zero for $0 < \phi < 0.12$ (dashed line in Fig. 6.3). The percolation threshold is found for all three CB grades between $\phi = 0.084$ to 0.155 . Due to the limited amount of samples available for this study, only for the N339 grade the percolation threshold could be studied in more detail and was calculated by

a nonlinear fit with Eq. 6.1 (full line in Fig. 6.3, see also Section 2.2.2) and $\phi_c = 0.148$ was found.

$$|\sigma_0| = |\sigma_M| + b(\phi - \phi_c)^c \quad (6.1)$$

An interesting finding in Fig. 6.3 is the large difference in conductivity between the different CB grades at high volume fractions. In literature it is found that the plateau value at high ϕ is usually independent of the filler structure [159, 160]. The reason for the large difference in the plateau value seen in our study is not yet clear and needs further investigation. Balberg [159] showed in his work that beside the percolation threshold, the critical exponent of the scaling law c (Eq. 6.1) is also strongly influenced by the structure of the CB particles. He found that highly structured, anisotropic CB (like the N121 grade, see Fig. 6.1) can be represented by elongated rod-like structures, whereas low structured particles like the N660 grade are better represented by spherical structures. The elongated particles showed a narrow distribution of the particle-particle distances and the formed networks facilitated the tunneling of electrons better than the spherical structures at the same filler concentration [159] and thus could explain the lower conductivity of the N660 at high volume fractions.

6.1.2. Curing tests

All samples used in this study contained a vulcanization system with sulfur. In order to prevent the curing of the system during the LAOS measurements, time dependent tests were conducted at different temperatures. In Fig. 6.4 the storage modulus of the sample filled with $\phi = 0.215$ N660 CB at 80 °C and 120 °C is plotted as function of measurement time t .

At 120 °C a strong increase of G' can be detected after approximately 60 min. This indicates the onset of the curing reaction, when the sulfur of the vulcanization system starts to react with the double bonds of the butadiene units. A covalent polymer network is formed which has a much higher elasticity than the unvulcanized rubber and thus result in an increase of G' . The rheological behavior of the CB filled compounds during vulcanization is further discussed in Section 6.1.2. No increase of the storage modulus can be detected at 80 °C, i.e. no significant cross-linking occurs at this temperature within the 2 h measurement time. Similar results were obtained for all S-SBR compounds. Because the LAOS measurements each last about 80 min, the upper limit of the

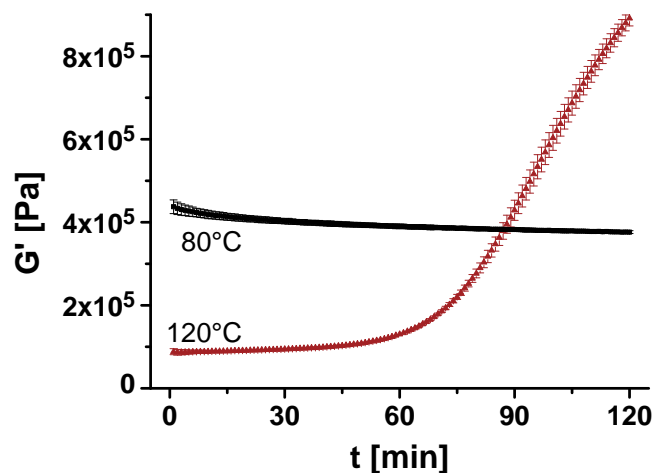


Figure 6.4.: Storage modulus of the S-SBR filled with $\phi = 0.215$ N660 CB measured at two different temperatures ($T = 80^\circ\text{C}$ and 120°C , $\omega_{1/2\pi} = 1\text{ Hz}$, $\gamma_0 = 0.1$, V50). At 120°C , G' increases after 60 min due to the start of the vulcanization reaction. At 80°C no increase of G' can be seen within the two hours measurement time.

measurement temperature used for the investigation of the unvulcanized samples in this section was 80°C .

6.1.3. SAOS frequency tests

For the rheological characterization of the different unvulcanized samples in the linear and the nonlinear viscoelastic regime, the following test protocol was used. The main focus lay on the LAOS strain amplitude test ($\omega_{1/2\pi} = 0.2\text{ Hz}$, $\gamma_0 = 10^{-3}$ to 8). In order to examine the linear viscoelastic behavior of the samples, a SAOS frequency test ($\omega_{1/2\pi} = 0.1\text{ Hz}$ to 10 Hz , $\gamma_0 = 0.1$) was also included before the LAOS test. This test was repeated after the LAOS measurement to check for permanent changes in the rubber structure caused by the large strain amplitudes used, which are known to happen in filled rubbers (like the Mullins effect, Section 2.2.3)

In Fig. 6.5, the results from the first SAOS test (prior to the LAOS strain amplitude test) are plotted for the three different CB grades. The moduli for each rubber grade are increasing with filler volume fraction ϕ , which would be consistent with an increase of the hydrodynamic effects, the in-rubber structure (volume fraction of occluded and bound rubber), and the filler-polymer interactions with increasing ϕ as discussed in Section 2.2.3. All samples are in the rubber plateau at high frequencies and this plateau extends to lower frequencies with increasing filler content. This results in an increase of the relaxation time τ of the polymer, i.e. the crossover of G' and G'' ,

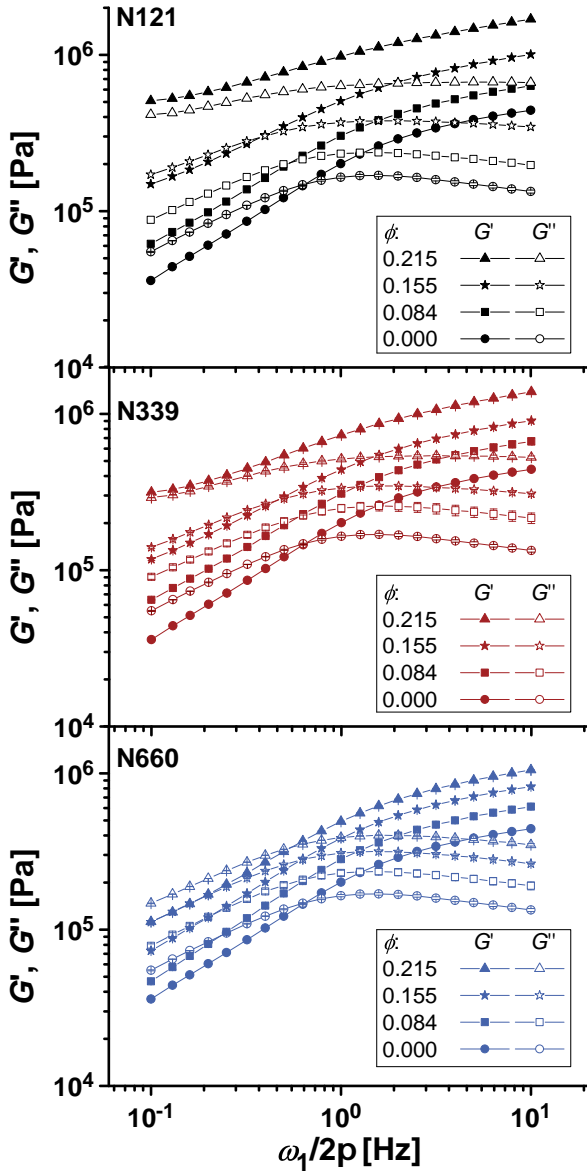


Figure 6.5.: SAOS frequency test results of the first SAOS test of each specimen ($\omega_1/2\pi = 0.1$ Hz to 10 Hz, $\gamma_0 = 0.1$, V50) at $T = 80^\circ\text{C}$ for the SBR filled with the three different grades of CB in three different volume fractions ($\phi = 0.084, 0.155$ and 0.215). The results for the sample without CB are shown in all graphs for better comparison.

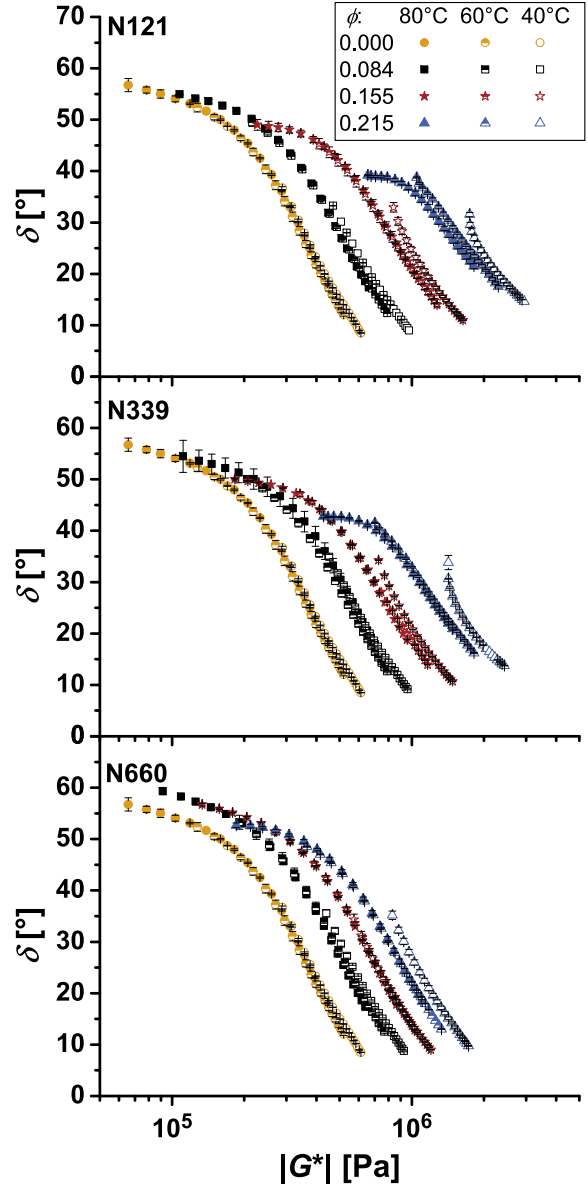


Figure 6.6.: Van Gorp-Palmen plot of the SBR samples filled with the three CB grades at volume fractions of $\phi = 0.084, 0.155$ and 0.215 . For better comparison, the results of the sample without CB is added to all three graphs. All data is from the first SAOS test ($\omega_1/2\pi = 0.1$ Hz to 10 Hz, $\gamma_0 = 0.1$, V50) prior to the LAOS strain amplitude test.

is shifted to lower frequencies. This can be also seen in Fig. 6.7, where the relaxation time τ is plotted as function of the CB volume fractions for all samples. A longer relaxation time indicates

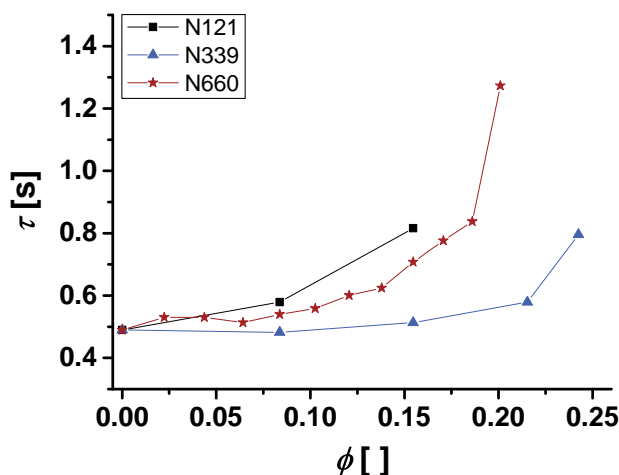


Figure 6.7.: Relaxation time τ of the S-SBR filled with different volume fractions of CB (grades N121, N339, and N660) at 80 °C. The relaxation time was calculated by the crossover of G' and G'' (Fig. 6.5). For $\phi > 0.159$ and $\phi > 0.201$ the crossover is out of the investigated frequency range for the N121 and the N339 grade, respectively. Thus no relaxation times are given for these highly filled compounds.

a reduced mobility of the polymer chain, which could be explained by additional filler-polymer interactions in the filled compounds. The effect of the filler is strongest for the N121 grade and lowest for the N660. The higher specific surface area of N121 might enables more interactions with the surrounding rubber and therefore a pronounced increase of the moduli. At higher filler volume fractions ($\phi > 0.159$ (N121) and $\phi > 0.201$ (N339)), no terminal behavior is seen, i.e. these compounds are dominantly elastic over the whole frequency range investigated, and the storage modulus is nearly independent of the applied frequency at low $\omega_1/2\pi$. This was also seen by Aranaugen et al. [88], who attributed this behavior to the increased probability of polymer chains forming direct bridges between two neighboring filler particles with increasing filler content. These polymer chains can not fully relax unless they are desorbed from one of the filler surfaces.

Van Gurp-Palmen plots, i.e. the loss angle δ as function of the absolute value of the complex modulus $|G^*|$, are shown in Fig. 6.6 for all three CB grades. For the highly filled samples, the curves measured at different temperatures do not overlap, i.e. the loss angle of each compound depends on the temperature. This means that the time-temperature-superposition (TTS) principle is not valid for these systems. This can also be seen in Fig. 6.8, in which $|G^*|_{\delta=30^\circ}$ is plotted, the absolute value

of the complex modulus at which the loss angle δ is equal to 30° . The results for the measurements

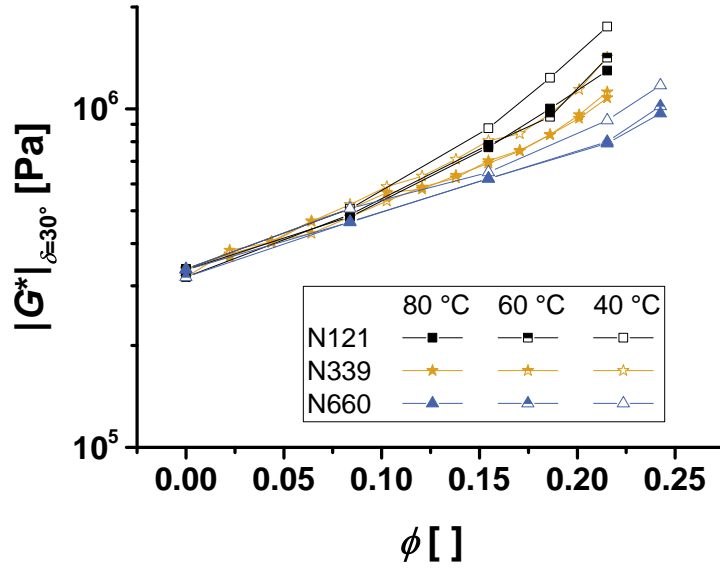


Figure 6.8.: Absolute value of complex modulus at a loss angle $\delta = 30^\circ$ as function of ϕ at three different temperatures extracted from Fig. 6.6. The values at $T = 40^\circ\text{C}$ deviate from those at 60°C and 80°C for all three CB grades.

at 40°C deviate from those for the other measurements for all three CB grades. There are different possible reasons for this behavior. One is the presence of additives in all samples. The solubility of these additives in the polymer matrix is a function of temperature and some of the additives have according to the literature a melting point in the temperature range investigated (the melting point of stearic acid is for example 69°C [161]). In Fig. 6.9 the results for the DSC measurement of one of the compounds (filled with $\phi = 0.084$ N121 CB) is given. The glass transition of the polymer matrix is found at approximately -40°C . A peak (either minimum or maximum for heating or cooling, respectively) at approximately 50°C might correspond to a melting/crystallization process of one of the additives and thus may be the reason for the temperature dependence of $|G^*|_{\delta=30^\circ}$. At 109°C a minimum is seen only in the first heating run, i.e. before the vulcanization reaction. Thus this should be the melting point of sulfur ($T_m = 107^\circ\text{C}$ [161]).

An important point for interpreting the SAOS frequency data, is the fact that the strain amplitude used in the frequency test ($\gamma_0 = 0.1$) is already in the nonlinear viscoelastic regime for the highly filled systems as can be seen later for example in Fig. 6.11 (p. 80) and the TTS principle is only valid in the linear regime. At this strain amplitude the nonlinear contribution $I_{3/1}$ ranges

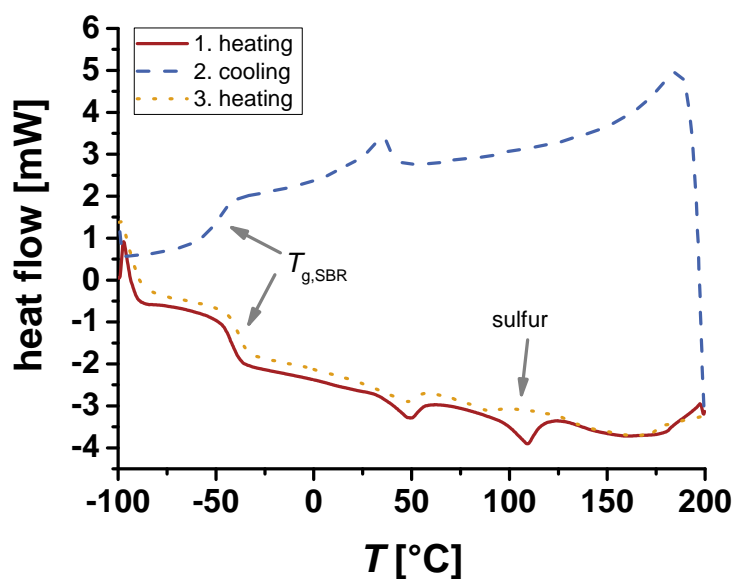


Figure 6.9.: DSC measurement of the S-SBR sample filled with $\phi = 0.084$ CB of grade N121 during all three runs (1. run: heating from -100 °C to 200 °C , 2. run: cooling from 200 °C to -100 °C , 3. run: heating from -100 °C to 200 °C , heating rate = 20 K min^{-1}). The glass transition temperature of the SBR is found at approximately -40 °C . The peak at 50 °C is seen in all three curves, whereas a minimum at 109 °C is only seen for in the first run and thus might be related to the vulcanization or one of the compounds of the vulcanization system.

from 0.005 to 0.1, depending on the filler volume fraction and the grade (see for example Fig. 6.12, p. 81). This strain amplitude was chosen in order to measure even the unfilled compound with enough sensitivity. The strain amplitude chosen is also comparable to those used in the standard testing of rubber (see e.g. [162]) The same strain amplitude was used for all samples in order to provide a comparable deformation history in the LAOS test.

The influence of the deformation history was examined by the comparison of the frequency tests before and after the LAOS test ($\omega_{1/2\pi} = 0.2\text{ Hz}$, $\gamma_0 = 10^{-3}$ to 8). It was found that the moduli changed for most of the samples by less than $\pm 15\%$. Only for the highly loaded SBR with filler volume fractions above the percolation threshold, the modulus of the second frequency test was up to 60% lower than the one of the first test. Typical results are shown in Fig. 6.10, for samples with different amount of N339 filler at 40 °C . For the sample with only $\phi = 0.044$ N339, the moduli changed by less than 12%, while the storage modulus decreased by more than 40% for the sample with $\phi = 0.215$ N339. The fact that the decrease is most severe at filler volume fractions above the percolation threshold indicates, that the filler-filler network might be partly destroyed and oriented during the LAOS test and can not reform within the resting period between the rheological test.

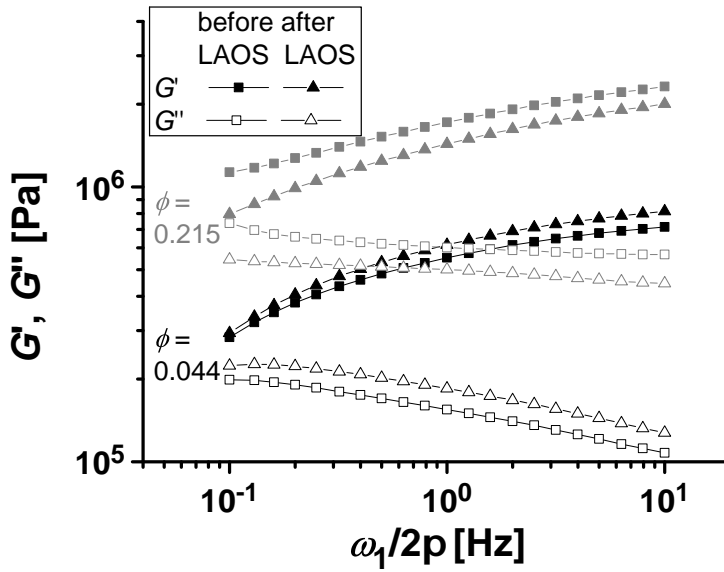


Figure 6.10.: Results of the frequency tests ($\omega_1/2\pi = 0.1$ Hz to 10 Hz, $\gamma_0 = 0.1$) before and after the LAOS strain amplitude test ($\omega_1/2\pi = 0.2$ Hz, $\gamma_0 = 10^{-3}$ to 8, V50) for the SBR with $\phi = 0.044$ and 0.215 N339 at 40 °C. The storage modulus decreased by more than 40 % in the second test for the highly filled sample. For the sample with $\phi = 0.044$ N339, the storage modulus is constant and the loss modulus increased by 12 %.

As could be seen in the TEM pictures (Fig. 6.1), the aggregates of the N121 grade have the highest anisotropy and the most complex fractal structure. Therefore, these particles are prone to the formation of agglomerates, which then would be destroyed during the LAOS test. This can also explain the larger decrease of the shear modulus for samples of the N121 series than for the ones of the N660 series. Additionally, the decrease was more pronounced at lower temperatures, when the viscosity of the polymers was higher. Hence, the local stresses during the applied deformation should have been larger, which would result in a higher deagglomeration.

6.1.4. LAOS strain amplitude tests

Influence of filler volume fraction

The influence of the CB volume fraction on the nonlinear rheological properties of the unvulcanized SBR compounds was investigated with the series containing the N339 grade.

The influence of the filler volume fraction on unvulcanized rubber has been largely investigated in the last few decades with a focus on linear parameters like the storage modulus or the loss factor [16, 29, 84, 94, 113, 163]. Figure 6.11 shows the influence of increasing CB volume fraction

on the absolute value of the complex modulus and on the loss factor. Three main effects of an increasing CB volume fraction can be identified. First, the modulus of the compounds is increased by up to one order of magnitude. Second, the loss tangent is decreased, especially at low strain amplitudes, which results in an increase of elasticity. Third, the onset of nonlinear viscoelasticity is shifted to lower γ_0 . These findings reflect the results explained in Section 2.2.3 on the Payne effect

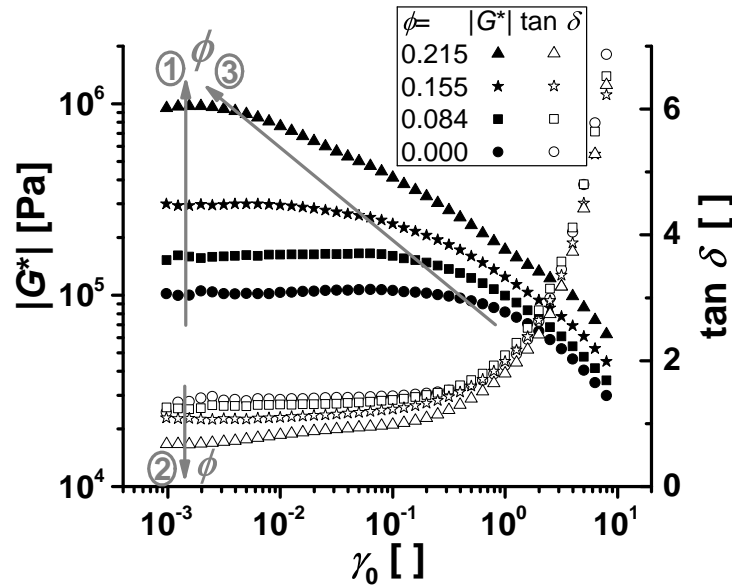


Figure 6.11.: Absolute value of the complex modulus $|G^*|$ and loss factor $\tan \delta$ as function of strain amplitude for SBR compounds filled with different concentrations of CB (grade N339) during the LAOS test ($\omega_1/2\pi = 0.2$ Hz, $\gamma_0 = 10^{-3}$ to 8, $T = 80^\circ\text{C}$, V50). Three main influences of the filler volume fraction can be seen. First, the modulus is increasing. Second, the elasticity is increasing, i.e. the loss factor is decreasing. Third, the onset of nonlinear viscoelasticity is shifted to lower strain amplitudes.

and are probably caused by a combination of the hydrodynamic effect of the filler, the additional contribution of immobilized rubber (occluded and bound rubber), and the reinforcement caused by the formation of a filler-filler and a filler-polymer network. These network structures might be partly destroyed when the strain amplitude is increased, which could explain the decrease of the modulus with increasing strain amplitude. The corresponding nonlinear results are shown in Fig. 6.12 for the third higher harmonic contribution.

The plot can be divided in four distinct sectors. In sector 1 ($\gamma_0 < 0.01$), the nonlinear stress response is decreasing, while the strain amplitude is increased with a scaling exponent of approximately -1 . The standard deviation (two specimen measured for each sample) is also very high. Both facts fit with the interpretation, that the absolute value $I(3\omega_1)$ is below the sensitivity limit

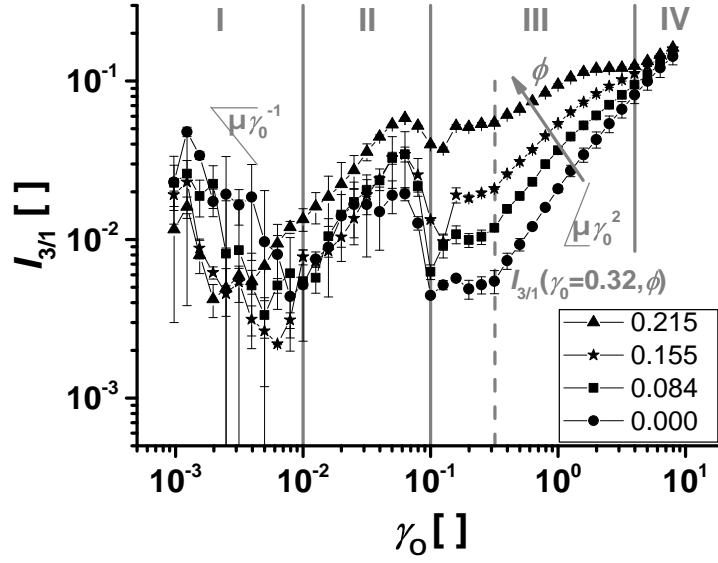


Figure 6.12.: Relative third higher harmonic contribution $I_{3/1}$ as function of strain amplitude for SBR compounds filled with different concentrations of CB (grade N339) during the LAOS test ($\omega_{1/2\pi} = 0.2$ Hz, $\gamma_0 = 10^{-3}$ to 8, $T = 80^\circ\text{C}$, V50). The plot can be divided in four sectors. In sector 1, the stress response is determined by noise. Sector 2 is dominated by a broad peak most likely caused by instrumental noise. In sector 3, the nonlinear response of the material is a function of ϕ . In sector 4 the different curves merge and the influence of ϕ is diminished. The dashed line marks the strain amplitude of $\gamma_0 = 0.32$.

of the instrument and hence determined by noise (see Eq. 2.19, p. 14).

Sector 2 ($0.01 < \gamma_0 < 0.1$) is dominated by a broad peak of $I_{3/1}$ and the values show a high standard deviation. The appearance of this peak is typical for measurements on the V50 rheometer and was discussed in Section 3.2. Even though the origin of this peak is not yet fully clear, most evidence indicates that it is due to instrumental noise.

In sector 3 ($0.1 < \gamma_0 < 4$) the nonlinear response of the material is above the sensitivity limit, i.e. above a strain amplitude of $\gamma_0 = 0.1$ the nonlinear material properties can be measured with the V50 rubber rheometer. In sector 3, $I_{3/1}$ scales with γ_0^m . The slope m is below 2 and decreasing with increasing filler volume fraction.

Finally in sector 4 of Fig. 6.12, the curves of the different compounds seem to merge and the filler effect is almost completely diminished. This is similar to results from Leblanc [29], who found a maximum of the absolute filler contribution to $I_{3/1}$ in CB filled rubbers at a strain amplitude of $\gamma_0 = 2$. The findings would be consistent with the following hypothesis. The increasing strain amplitude can lead to high local stresses at the rubber-filler interface. These high stresses might destroy the CB-rubber network and consequently reduce the filler influence on the nonlinear contribution to

a mere hydrodynamic effect. The break up of the physical network structure is also discussed in literature as explanation for the filler influence on $|G^*|$ at high strain amplitudes (Payne-effect), as was discussed in Section 2.2.3. The break up of the polymer-filler network would also be consistent with the reduced moduli in the second LAOS frequency test measured for the highly filled samples (Fig. 6.10).

The nonlinear rheological behavior in sector 3 can be explained by two possible effects, a filler dependent one and a filler independent one. Every polymer shows nonlinear behavior at higher strain amplitudes, when the polymer chains are oriented and stretched by the applied mechanical forces (Section 2.1.2). The finding that the scaling exponent m of the sample without filler differs from the value 2, which is the theoretical expectation for linear homopolymers (Eq. 2.20), can have different reasons. First, the deviation from the theoretical scaling law is found, when the nonlinear contribution is below or in the order of the lower torque sensitivity limit of the instrument, as it was discussed for sector 1 of Fig. 6.12. However, in sector 3 the torque is well above the sensitivity limit and therefore the measured values reflect material behavior. The nonlinear stress response is a vector sum of the nonlinear material response and the nonlinear instrumental contributions, which include a nonlinear strain signal. If the strain excitation has a high nonlinear contribution, this can also influence $I_{3/1}$ of the stress response. Therefore, the strain signal was analyzed with respect to its spectral contributions. The raw data of the excitation signal was captured with an external ADC card and the corresponding FT spectra were analyzed. Figure 6.13 shows the relative third higher harmonic contributions to the strain and the stress signals for the sample without CB. At very small strain amplitudes (sector 1 of Fig. 6.12) the nonlinear contribution of the strain signal is close to the one of the stress response. As the motor movement increases, the quality of the excitation improves, i.e. $I_{3/1}$ of the strain signal is decreasing, until it shows a plateau at $\gamma_0 > 1$ with a very low level of higher harmonic contributions ($I_{3/1} \approx 10^{-4}$). At $\gamma_0 > 1$, $I_{3/1}$ of the strain excitation is more than one order of magnitude lower than $I_{3/1}$ of the stress. Consequently, an imperfect strain excitation is not a plausible explanation for the lower slope of $I_{3/1}$ in sector 3 of Fig. 6.12. The sample without CB is not a pure polymer melt and contains different additives like stabilizers and vulcanization agents. If the additives are not completely dissolved or homogeneously distributed throughout the sample, phase separation might occur and

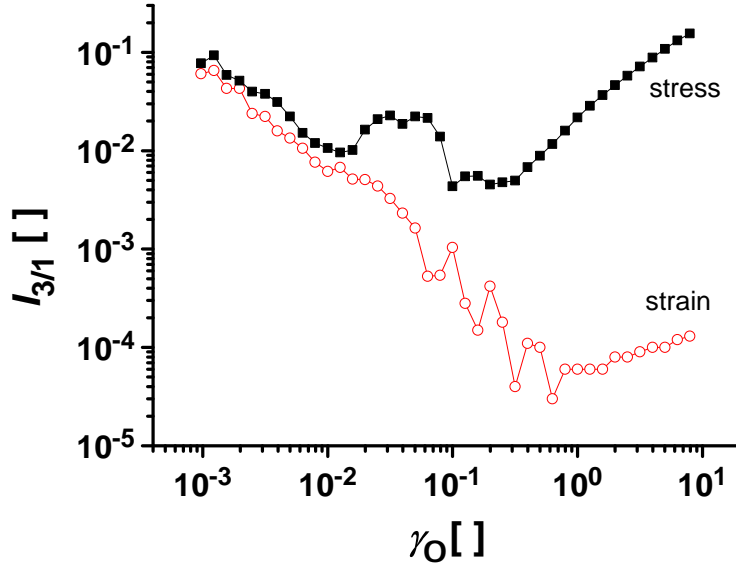


Figure 6.13.: Relative third higher harmonic contribution $I_{3/1}$ to the strain excitation and the stress response as function of the strain amplitude for the S-SBR compound without CB during the LAOS test ($\omega_1/2\pi = 0.2$ Hz, $\gamma_0 = 10^{-3}$ to 8, $T = 80$ °C, V50). For $\gamma_0 > 0.1$ the nonlinear contribution to the strain excitation is more than a decade lower than the nonlinear contribution to the stress response.

the deformation of the interface could result in additional nonlinear contributions. An effect of the interface on $I_{3/1}$ in phase separated polymer systems was already found in melts of a PS-PI diblock copolymer with a lamellar morphology [155], in emulsions of two Newtonian liquids [23], and in beer foam [51]. To clarify the reasons for the non-quadratic scaling of $I_{3/1}$ in sector 3 and the influence of the various additives used in the compounds on the LAOS behavior, the pure polymer (without any additives) needs to be investigated in future studies as well as the phase morphology of the polymer with additives.

The filler influence on $I_{3/1}$ in sector 3 is most pronounced at low strain amplitudes. There seems to be a plateau of $I_{3/1}$ at $0.1 < \gamma_0 < 0.32$. In this range of γ_0 , the instrumental noise, which causes the peak in sector 2, has still a large influence on the measured nonlinearity. Therefore, the values of $I_{3/1}$ at a strain amplitude of $\gamma_0 = 0.32$ ($\equiv I_{3/1}(\gamma_0 = 0.32, \phi)$) is the lower sensitivity limit for nonlinear measurements of the S-SBR samples on the V50. Thus $I_{3/1}(\gamma_0 = 0.32, \phi)$ was further investigated to quantify the filler influence. This is shown for example in Fig. 6.14, where $I_{3/1}(\gamma_0 = 0.32, \phi)$ is plotted normalized to the value of the sample without CB as function of the CB volume fraction (symbols). The addition of $\phi = 0.215$ CB results in a ten times higher nonlinear contribution. A mathematical description of this data has to fulfill certain features. The function

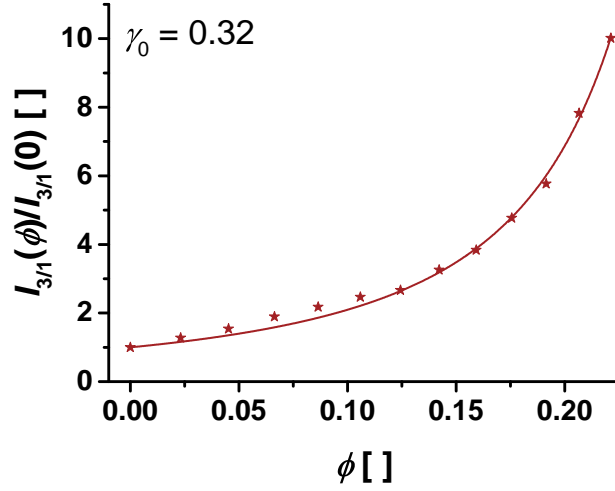


Figure 6.14.: Relative third higher harmonic contribution $I_{3/1}(\gamma_0 = 0.32, \phi)$ for SBR compounds filled with different concentrations of CB (grade N339) (normalized to the value of the sample without CB) during the LAOS test ($\omega_1/2\pi = 0.2$ Hz, $\gamma_0 = 0.32$, $T = 80$ °C, V50). With increasing filler volume fraction the nonlinear contribution is increasing. The data (symbols) was fitted with Eq. 6.3 (line). The calculated maximum packing fraction $\phi_m = 0.31$ for the N339 grade.

has to start at 1 for $\phi = 0$ due to the normalization, with increasing ϕ the function has to increase monotonically and it has to show a singularity at the highest filler concentration possible in the compound. A general approach that fulfills these three criteria with a minimum of free parameters (two) is given for example by Eq. 6.2.

$$y = \left(1 - \frac{\phi}{x_m}\right)^{-d} \quad (6.2)$$

This is a two parameter model with a critical value, x_m , at which the equation has a singularity and a scaling exponent d . This equation was first used to fit the data in Fig. 6.14 and a scaling exponent of $d = -2.07$ was found. In order to reduce the amount of parameters in the mathematical description of $I_{3/1}(\gamma_0 = 0.32, \phi)$, the scaling exponent was fixed to $d = -2$ and Eq. 6.3 was used for the fit shown in Fig. 6.14 (line).

$$\frac{I_{3/1}(\gamma_0 = 0.32, \phi)}{I_{3/1}(\gamma_0 = 0.32, \phi = 0)} = \left(1 - \frac{\phi}{\phi_m}\right)^{-2} \quad (6.3)$$

The reduction of the amount of free parameters is especially important for the investigation of the influence of the filler grade (see p. 88), because less samples (five) were measured of the filler grades

N121 and N660.

Equation 6.3 is similar to the Krieger-Dougherty equation (Eq. 6.4), which is used to describe the influence of the filler volume fraction on the viscosity of dispersions [164].

$$\frac{\eta(\phi)}{\eta_0} = \left(1 - \frac{\phi}{\phi_m}\right)^{-[\eta]\phi_m} \quad (6.4)$$

η_0 is the zero shear viscosity of the matrix, $[\eta]$ the intrinsic viscosity of the dispersion and ϕ_m the maximum packing fraction of filler in the dispersion. For the Krieger-Dougherty it is also found that the scaling exponent of Eq. 6.4, $-[\eta]\phi_m$, is often close to -2 [165].

Similar to Eq. 6.4, the only free parameter of Eq. 6.3 might be interpreted as maximum packing fraction. For example $\phi_m = 0.74$ is expected for unimodal hard spheres in a closest packing. For the N339 CB grade a maximum packing fraction of $\phi_m = 0.31$ was found. This value is much lower than the one for the hard spheres, which is due to the complex fractal structure of the particles (see Fig. 6.1). Therefore, these particles can not be packed so tightly in the rubber matrix. This effect was also found by Kasgoz et al. [166], who reported that the maximum packing fraction of various filler types, such as CB, carbon fibers, and graphite, depends on the aspect ratio of the respective filler.

For the physical explanation of the filler influence on $I_{3/1}(\gamma_0 = 0.32, \phi)$, different mechanisms are plausible. The occluded rubber present in the cavities of the complex filler particles is partly shielded from the applied deformation and this could increase the stress in the other parts of the polymer matrix [84]. Hence, the stress in the compound would be unequally distributed and the highest should be found close to the filler surface due to the large difference in modulus between the filler and the polymer [167, 168]. According to the literature, the polymer surrounding the filler, the bound rubber, can also be interpreted as glassy bridges at the measurement temperature with a finite lifetime between different particles [91]. The high stress acting on these bridges could result in a decrease of their lifetime, which would increase the nonlinear behavior [91] and cause strain hardening [92]. With increasing filler loading, the content of occluded rubber and solid filler in the matrix is increasing. Hence the effect of the local stress concentration on the bound rubber should be more pronounced and the nonlinear contribution increased.

Influence of CB grade

The three CB grades used in this study vary widely in their structure, as could already be seen in the TEM images of the different particles (Fig. 6.1). The CB of grade N121 is made of small primary particles, which is consistent with its high NSA value (Table 6.1). The aggregate is anisotropic and the surface is very rough. The N339 grade is made of primary particles with a higher diameter. The aggregate is larger than the one of the N121. It has also a rough surface and a high anisotropy. Due to the much larger primary particles, the surface of the N660 aggregate is smooth compared to the others with only a few voids.

The filler grade has a strong influence on the linear parameters only at higher volume fractions of CB. This is shown for example in Fig. 6.15 for $|G^*|$ as function of γ_0 . At $\phi = 0.084$, the difference

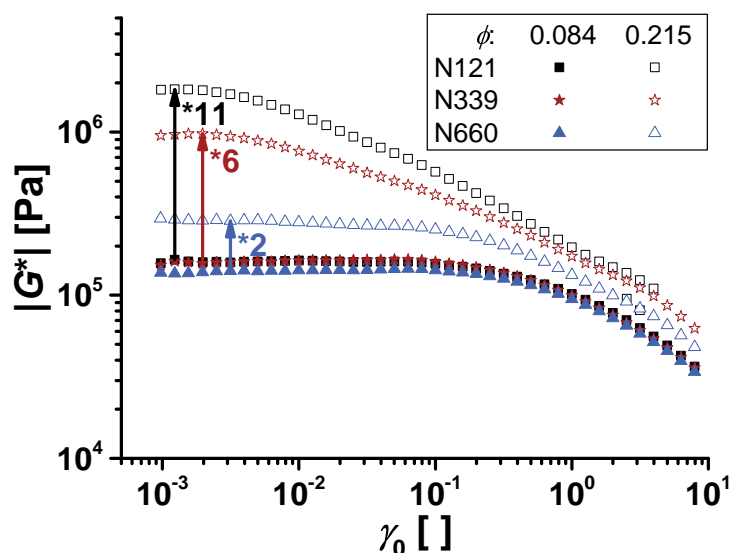


Figure 6.15.: Absolute value of the complex modulus $|G^*|$ as function of γ_0 ($\omega_{1/2\pi} = 0.2$ Hz, $T = 80$ °C, V50) for S-SBR filled with all three different CB grades at two filler volume fractions ϕ . For $\phi = 0.084$ there is no significant influence of the CB grade, but if the filler loading is increased to $\phi = 0.215$ the modulus of the N121 sample is increased by a factor of 11, which is more than five times larger than the increase of the sample with N660 filler.

between the filler grades is only marginal (difference between N121 and N660 $< 15\%$). If the filler loading is increased to $\phi = 0.215$, $|G^*|$ is more than five times larger for the N121 filled sample than for the N660 filled sample. The results for the N339 are in between the other two, but closer to the values of the N121.

A similar behavior is observed for the nonlinear parameter $I_{3/1}$ (Fig. 6.16). The addition of filler

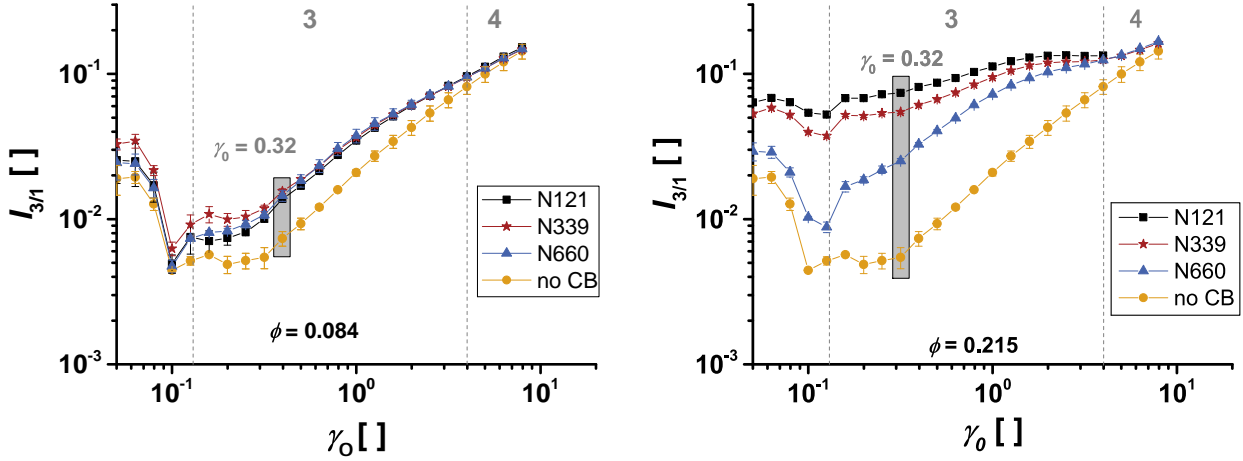


Figure 6.16.: Nonlinear parameter $I_{3/1}$ in region 3 and 4 for the S-SBR with $\phi = 0.084$ (left) and $\phi = 0.215$ (right) of the different CB grades ($\omega_{1/2\pi} = 0.2$ Hz, $T = 80$ °C, V50). For a better comparison, the result of the unfilled compound is given in both graphs. The addition of filler results for all grades in an increase of $I_{3/1}$, compared to the unfilled sample. At $\phi = 0.084$ no significant difference is found between the fillers in contrast to $\phi = 0.215$, for which the samples with the N121 show the highest nonlinear contributions and the samples with N660 the lowest. The marked area corresponds to a strain amplitude of $\gamma_0 = 0.32$.

resulted for all samples in the increase of the nonlinear parameter compared to the unfilled sample (same data for unfilled sample in both graphs). At a small filler volume fraction ($\phi = 0.084$), $I_{3/1}$ does not differ much between the three grades, as it was also observed for $|G^*|$. If ϕ is increased to 0.215, the structure of the CB has a large influence on the nonlinear mechanical behavior in region 3. For the sample filled with N121, a much higher value of $I_{3/1}$ was measured compared to the sample with N339. The sample with N660 has the lowest values of $I_{3/1}$. For a better investigation of the filler influence, the nonlinear contribution $I_{3/1}$ at $\gamma_0 = 0.32$ was used as a parameter (marked areas in Fig. 6.16). This parameter is shown in Fig. 6.17 as function of the filler volume fraction ϕ (full symbols).

It can be seen in this graph that the particle structure has a large influence on the nonlinear mechanical behavior of the SBR. The increase of $I_{3/1}$ with increasing ϕ is most pronounced for the N121 grade and the smallest for the N660 grade. The data was also fitted with Eq. 6.3 in order to get the maximum packing fraction of all grades. The calculated values for ϕ_m are 0.29, 0.31 and 0.39 for the N121, the N339, and the N660 grade, respectively. The absolute value of the complex modulus (open symbols) is less affected by the CB grade at this strain amplitude. The addition of $\phi = 0.215$ N121 to the S-SBR leads to an increase of $I_{3/1}$ by a factor of more than 13, whereas the modulus is only increased by a factor of 3.5. To test the significance of this difference, the

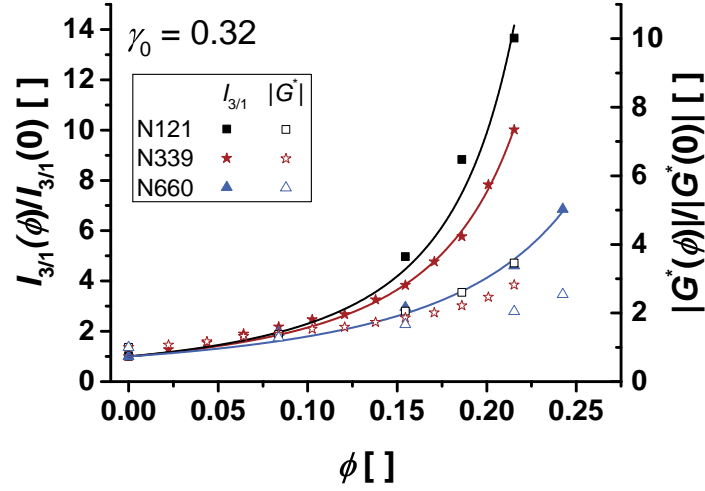


Figure 6.17.: Nonlinear parameter $I_{3/1}(\gamma_0 = 0.32, \phi)$ (full symbols) and absolute value of the complex modulus $|G^*|$ (open symbols) normalized to the respective value of the unfilled compound for the three different rubber grades ($\omega_1/2\pi = 0.2$ Hz, $T = 80$ °C, V50). The influence of the CB grade increases with increasing ϕ and is much more pronounced on the nonlinear than on the linear parameter at this amplitude. The lines correspond to a nonlinear fit of the nonlinear data with Eq. 6.3. The maximum packing fractions are 0.29, 0.31 and 0.39 for the N121, the N330 and the N660 CB grades, respectively.

respective error in determining each value has to be taken into account. This was done by dividing the increase of each parameter P (either $I_{3/1}(\gamma_0 = 0.32, \phi)$ or $|G^*(\gamma_0 = 0.32, \phi)|$) caused by the addition of $\phi = 0.215$ CB by the standard deviation of the respective parameter for the unfilled compound $\sigma_{P(\phi=0)}$ (calculated by the measurement of two specimen):

$$\text{Sensitivity of } P = \frac{P(\phi = 0.215) - P(\phi = 0)}{\sigma_{P(\phi=0)}} \quad (6.5)$$

The results of this calculation are given in Table 6.2 and they indicate a higher sensitivity of the nonlinear contribution $I_{3/1}$ to changes in the CB volume fraction for all three CB grades.

Table 6.2.: Sensitivity of the relative third higher harmonic contribution $I_{3/1}(\gamma_0 = 0.32, \phi)$ and the absolute value of the complex modulus $|G^*(\gamma_0 = 0.32, \phi)|$ to variations of the CB volume fraction ϕ ($\omega_1/2\pi = 0.2$ Hz, $T = 80$ °C). This sensitivity was calculated according to Eq. 6.5.

| | $ G^* $ [kPa] | | | $I_{3/1}$ [] | | |
|---------------|---------------|-------------|---------------|-----------------|-----------------|-----------------|
| | N121 | N339 | N660 | N121 | N339 | N660 |
| $\phi = 0$ | 99 ± 6 | 99 ± 6 | 99 ± 6 | 0.55 ± 0.09 | 0.55 ± 0.09 | 0.55 ± 0.09 |
| $\phi = 0.22$ | 341 ± 2 | 278 ± 0 | 202.0 ± 1 | 7.40 ± 0.04 | 5.47 ± 0.12 | 2.52 ± 0.10 |
| Sensitivity | 40.3 | 29.8 | 17.2 | 76.1 | 54.7 | 21.9 |

From this data it can be clearly concluded that the choice of the CB grade has a tremendous

effect on the nonlinear mechanical properties of the rubber. The reason for this influence might be attributed to the particle structure. The aggregates of the N121 grade, which is the grade causing the highest nonlinear contributions, consist of many small primary particles and thus have a very rough and also very large surface compared to the bulky aggregates of the N660 grade with the much larger primary particles. The larger surface area of the N121 particles should enable the formation of more rubber-filler interactions at the interface. The polymer thus would be stronger adsorbed to the CB and a more stable network would be formed. Additionally, the higher amount of occluded rubber in the voids of the N121 particles can lead to a higher effective filler volume fraction.

The influence of the filler grade is most pronounced at high filler loadings. This indicates the formation of a filler-filler network, which also plays a crucial role on the nonlinear mechanical response. It is known from percolation theory [73] and verified in many experiments [59, 71, 159] that the shape of a particle has a large influence on the percolation threshold, i.e. the minimum filler volume fraction needed to form continuous filler structures throughout the sample. This is most obvious in the comparison of CB and carbon nanotubes. The latter have a much higher aspect ratio and hence show a much lower percolation threshold than CB, usually already at a few volume percent [24, 76, 160]. As could be seen in the TEM images (Fig. 6.1), the aggregate of the N121 grade shows a higher aspect ratio than the other fillers. Therefore, N121 most likely has a lower percolation threshold than the other fillers and the filler-filler network would be stronger, which might also explain the large differences in the conductivity at high volume fractions found for the different grades (Fig. 6.3). Due to the limited amount of samples filled with this grade of CB, the electrical percolation threshold could only be roughly determined between $0.084 < \phi_c < 0.155$. The stronger network would also explain the larger increase of the complex modulus at low strain amplitudes for the N121 filler than for the N660.

The nonlinear mechanical contribution in filled elastomers is most probably also related to the dynamic destruction of the filler-filler and the filler-polymer network. A break down of the filler-filler network should lead to an increased number of isolated particles in the polymer matrix, which then could be oriented by the flow and thus contribute to a higher value of $I_{3/1}$.

An important parameter for the nonlinear mechanical contribution is the size of the interface

between CB and rubber, because this size can be related to the amount of interactions between the two components. Therefore, in Fig. 6.18 $I_{3/1}$ was plotted as function of the size of the interface. This interfacial area was calculated by the oil adsorption number (OAN) times the CB volume

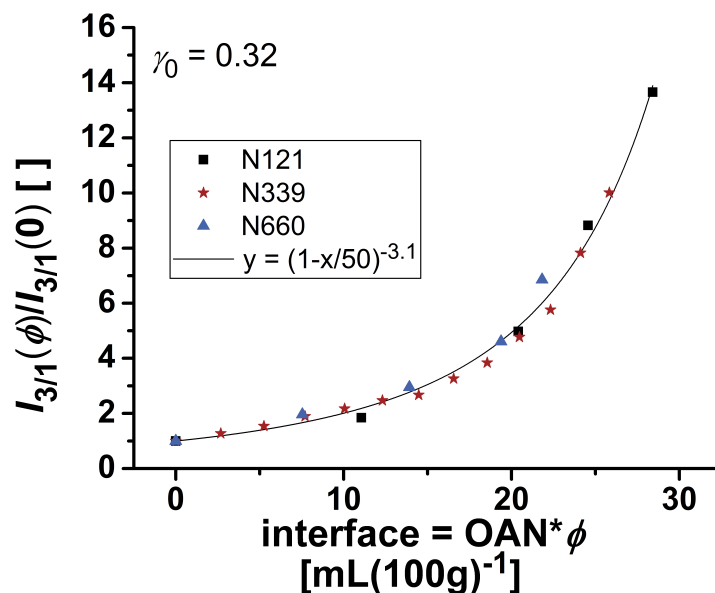


Figure 6.18.: Nonlinear parameter $I_{3/1}(\gamma_0 = 0.32)$ of the three different CB grades normalized to the corresponding value of the sample without CB as function of the size of the interface between rubber and CB ($\omega_{1/2\pi} = 0.2$ Hz, $T = 80$ °C, V50). The size of the interface was approximated by the product of the oil adsorption number (OAN) and the CB volume fraction ϕ . The unit is therefore mL/100g. The data of all three grades together was fitted according to Eq. 6.2. With that a critical surface area of $x_m = \text{OAN} \cdot \phi = 50$ and a scaling exponent of $d = -3.1$ were found.

fraction ϕ . The OAN was chosen and not the nitrogen surface area NSA, because the oil used to measure the OAN is closer in size to rubber molecules than nitrogen. Not all parts of the filler surface, where nitrogen can adsorb, are also accessible for the polymer chains and the OAN is therefore better suited. The drawback is that the size of the interface does not have the unit of an area. The assumption that the interface of the rubber is defined by the product of the OAN and ϕ is based on the linear relationship between the maximum packing fraction ϕ_m and the OAN, which was found in this work, but only three different CB grades were tested. Therefore, the investigation of additional CB grades is needed to validate this finding. It is also possible that the anisotropy of the particles needs to be taken into account by another factor. In Fig. 6.18 a nonlinear fit of the data for all three grades with Eq. 6.2 is shown (black line). With this equation a critical surface area of $x_m = \text{OAN} \cdot \phi = 50$ and a scaling exponent of $d = -3.1$ were found for the mathematical description of the nonlinear contribution $I_{3/1}(\gamma_0 = 0.32)$ as function of the interface area in a CB

filled compound for all CB grades.

Influence of measurement temperature

The measurement temperature is another important parameter for the rheological behavior of filled elastomers. From the van Gorp-Palmen plots (Fig. 6.6) it could already be concluded that the TTS principle is not valid for the highly filled systems, so the temperature dependence of $I_{3/1}$ was investigated. Figure 6.19 shows $I_{3/1}$ during the LAOS amplitude test for two samples with $\phi = 0$ and 0.215 N339 CB at three different temperatures. When the temperature is decreased

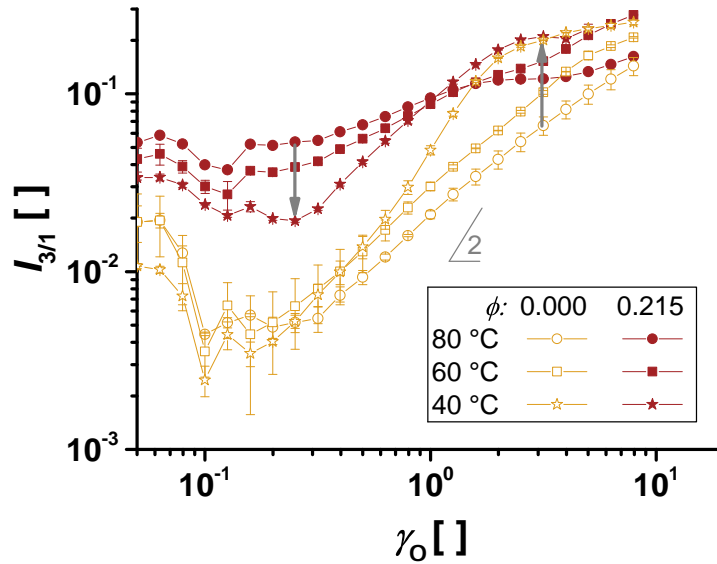


Figure 6.19.: Nonlinear parameter $I_{3/1}$ of SBR with $\phi = 0.215$ and without N339 CB at different temperatures ($\omega_{1/2\pi} = 0.2$ Hz, V50. With decreasing temperature $I_{3/1}$ is increasing at large amplitudes for both samples and at medium amplitudes $I_{3/1}$ is decreasing for the system with CB.

from 80 °C to 40 °C, $I_{3/1}$ is increasing for both samples at high strain amplitudes ($\gamma_0 > 1$). At 40 °C, the curves of the filled and unfilled sample merge at $\gamma_0 \approx 3$ instead of $\gamma_0 \approx 8$ as it is found for the measurement at 80 °C. At medium amplitudes ($0.1 < \gamma_0 < 1$) the temperature dependent behavior of $I_{3/1}$ is different. No significant change of $I_{3/1}$ can be seen for the sample without CB, whereas $I_{3/1}$ is decreasing for the filled sample.

The first observation made in Fig. 6.19, the increase of $I_{3/1}$ at large amplitudes, might be explained by the increase of the matrix viscosity due to the lower temperature. The higher viscosity should result in higher local stresses and the destruction of the network structure in the compound

would be more severe. The strain amplitude needed for an almost complete destruction of the physical networks would hence be reduced and within the measurement range. The second observation, the behavior of $I_{3/1}$ at medium amplitudes, is further illustrated in Fig. 6.20, where $I_{3/1}(\gamma_0 = 0.32)$ (full symbols) as well as $|G^*(\gamma_0 = 0.32)|$ (open symbols), both normalized to the corresponding value of the sample without CB, are plotted as function of the CB volume fraction ϕ (N339 grade) for three different temperature.

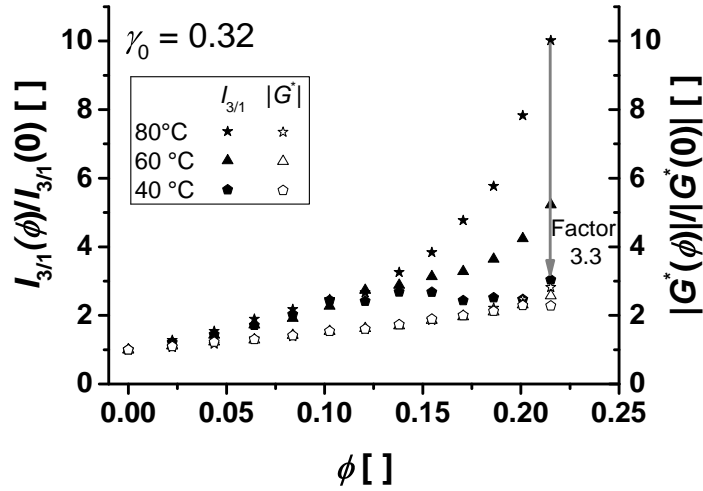


Figure 6.20.: Nonlinear parameter $I_{3/1}(\gamma_0 = 0.32)$ (full symbols) and absolute value of the complex modulus $|G^*(\gamma_0 = 0.32)|$ (open symbols) normalized to the respective value of the unfilled compound as function of the N339 CB volume fraction ϕ for three different temperatures ($\omega_1/2\pi = 0.2$ Hz, V50). The higher harmonic contribution is decreased at lower temperatures only for large ϕ . For $\phi = 0.215$ the decrease is more than a factor of three. In contrast, there is only a slight change of the modulus with temperature.

The temperature has only little effect on $|G^*|$, whereas $I_{3/1}$ is decreased by a factor of three if the sample with $\phi = 0.215$ is measured at 40 °C instead of 80 °C. Most interesting is the observation that the temperature dependence of $I_{3/1}$ is only at high filler loadings ($\phi > 0.1$) detectable. This may indicate again the importance of the filler-filler network at this strain amplitude range.

6.2. Influence of carbon black on vulcanized rubber

Since the invention of the sulfur based vulcanization of NR by C. Goodyear in 1844 [1], a wide field of applications is accessible for rubber products. By the formation of a covalent polymer network the processable and deformable but also sticky uncured rubber is turned into a highly elastic solid, which is insoluble and keeps its shape. This enabled the use of vulcanized rubber products in many

areas, e.g. tires, sealing and dampers [169]. There are different ways to create a covalent polymer network. For rubber materials, sulfur based vulcanization is still one of the most important cross-linking reactions for rubbers with double bonds [6, Chapter 3.2]. For rubbers without double bonds, other types of cross-linking are used, e.g. with peroxides.

A single, flexible polymer chain has many possible configurations with (almost) the same potential energy and thus many degrees of freedom [6, Chapter 2]. In the relaxed state it will be in one of the most probable configurations, which is a coiled structure. If a force is applied on a coil, it is deformed. This is a less probable configuration and reduces the entropy of the chain. Thus it tends back into the coiled structure, which creates a tension in the polymer and is the reason for rubber elasticity [170]. Linear chains also have the possibility to flow, when external forces are applied and thereby change their position and dissipate energy. By linking linear chains together in a covalent network, the flow of the polymer chains is prevented. The energy used to stretch the network is mostly elastically stored in the material and is gained when the forces are released.

The understanding of the structure of vulcanized rubber and knowledge about the influence of this structure on their mechanical behavior are, due to the importance of vulcanized rubber in technical applications, important research areas. In this section, Fourier-Transform rheology is used to get new insight on the influence of solid fillers, namely CB, on the mechanical behavior of vulcanized rubbers under LAOS. The samples used were the same as in the previous section. They contain a vulcanization system based on sulfur, with TBBS (*N-tert*-butylbenzothiazole-2-sulphenamide, Fig. 6.21) as accelerator and zinc oxide and stearic acid as activators. The investigation was restricted to the samples with $\phi = 0.084, 0.154$ and 0.215 CB of grades N121 and N660.

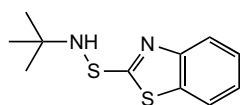


Figure 6.21.: Accelerator *N-tert*-butylbenzothiazole-2-sulphenamide (TBBS)

For the measurement of the vulcanization properties, different test protocols were used. They all consist of a combination of SAOS frequency, LAOS strain amplitude and isothermal tests and are summarized in Table 6.3. During the isothermal test, the compound is cured at elevated temperatures. The measurement conditions for the SAOS frequency test ($\gamma_0 = 0.05$, $\omega_{1/2\pi} = 0.1$ Hz to 10 Hz) and the LAOS strain amplitude test ($\gamma_0 = 10^{-1}$ to 2, $\omega_{1/2\pi} = 0.2$ Hz) were always

the same and the temperature was 80 °C in these test. The test names correspond to the order of the performed test. For the isothermal test, the test conditions are given in brackets.

Table 6.3.: Test protocols for the vulcanization on the V50. The different subtests were performed from left to right. The nomenclature of the different test names is: S and L correspond to a SAOS frequency ($T = 80\text{ °C}$, $\gamma_0 = 0.05$, $\omega_{1/2\pi} = 0.1\text{ Hz}$ to 10 Hz) and LAOS strain amplitude tests ($T = 80\text{ °C}$, $\gamma_0 = 10^{-3}$ to 2), respectively. The test conditions of the isothermal test I are given in brackets in the order T - γ_0 - t . All LAOS and isothermal measurements were done at $\omega_{1/2\pi} = 0.2\text{ Hz}$.

| Test | SAOS | LAOS | Isotherm | LAOS | SAOS |
|------------------------|------|------|------------------------------------|------|------|
| I(160-0.05-20)-L-S | | | 160 °C, $\gamma_0 = 0.05$, 20 min | X | X |
| I(160-0.05-60)-L-S | | | 160 °C, $\gamma_0 = 0.05$, 60 min | X | X |
| I(180-0.05-20)-L-S | | | 180 °C, $\gamma_0 = 0.05$, 20 min | X | X |
| S-L-I(160-0.05-20)-L-S | X | X | 160 °C, $\gamma_0 = 0.05$, 20 min | X | X |
| S-L-I(160-0.50-20)-L-S | X | X | 160 °C, $\gamma_0 = 0.50$, 20 min | X | X |

By comparing the tests I(160-0.05-20)-L-S and I(160-0.05-60)-L-S, the influence of the vulcanization time was investigated. In test I(180-0.05-20)-L-S a higher vulcanization temperature of 180 °C was used. For tests S-L-I(160-0.05-20)-L-S and S-L-I(160-0.50-20)-L-S, the SAOS frequency and the LAOS strain amplitude test were additionally added prior to the vulcanization test to be able to directly compare the influence of the vulcanization on one specimen. In test S-L-I(160-0.50-20)-L-S a strain amplitude of $\gamma_0 = 0.5$ was used in contrast to $\gamma_0 = 0.05$ in all other vulcanization tests in order to investigate the influence of γ_0 . The frequency of the isothermal and LAOS tests was always the same, $\omega_{1/2\pi} = 0.2\text{ Hz}$.

This section is divided in two parts. First, the changes of the linear and nonlinear rheological properties during the isothermal vulcanization test are discussed. In the second part, the rheological behavior of the cured samples under LAOS is investigated.

6.2.1. Rheology during the isothermal vulcanization

Vulcanization is usually investigated in closed gap rubber rheometers, because the torque is increasing with increasing cross-link density and hence can be directly related to the vulcanization process. In Fig. 6.22 a typical curing curve is shown, measured on the V50 for the sample with 20 phr N121 CB at 160 °C (test I(160-0.05-60)-L-S).

In this test, the geometry of the rheometer is heated to the vulcanization temperature ($T = 160\text{ °C}$) and the sample is inserted. Then the geometry is directly closed and the measurement

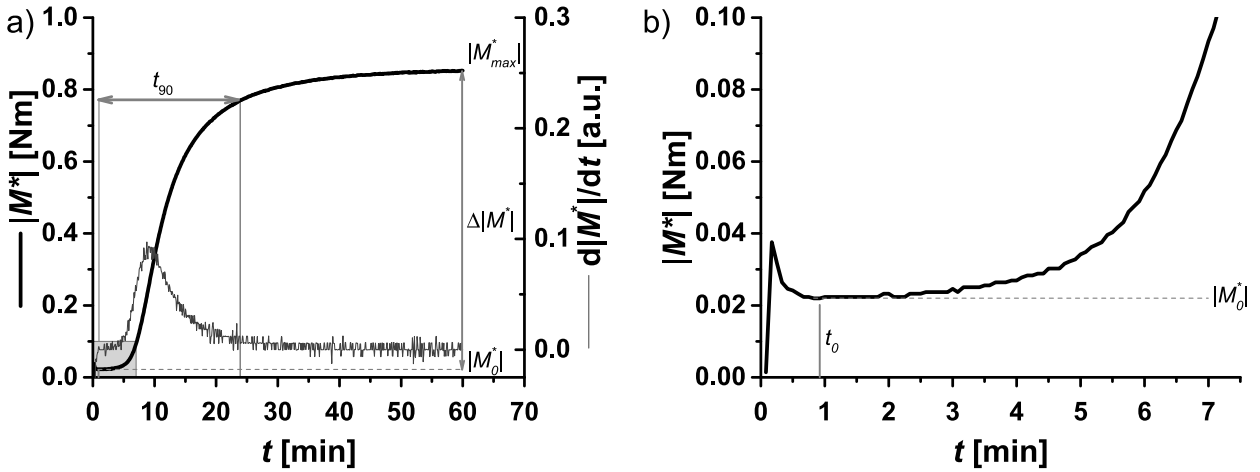


Figure 6.22.: a) Absolute value of the complex torque $|M^*|$ (black line) and its time derivative (gray line) of the S-SBR filled with $\phi = 0.084$ N121 CB as function of time (test I(160-0.05-60)-L-S, $\omega_{1/2\pi} = 0.2$ Hz, $\gamma_0 = 0.05$, $T = 160$ °C, V50) b) Magnification of the gray box in a). First, $|M^*|$ is slightly decreasing to a minimum value $|M_0^*|$ at time t_0 , due to the decrease of the viscosity when the polymer is heated. The modulus subsequently increases when the vulcanization reaction started and finally $|M^*|$ approaches a plateau value when the reaction is finished. The t_{90} is defined as the time, where $|M^*|$ increased by 90 % of $\Delta|M^*|$. The derivative of $|M^*|$ is a measure for the cure rate.

started. In the first few seconds, the polymer is heated to the measurement temperature. Thus the torque is slightly decreasing and reaches a minimum value $|M_0^*|$ at time t_0 as can be seen in Fig. 6.22 b). After the start of the vulcanization reaction, the torque increases and eventually reaches a plateau, when the reaction is complete. Depending on the vulcanization system used, also a continuously growing torque is possible, which is called a marching vulcanization. Another possibility is a vulcanization reaction with a simultaneous degradation of the network (also called reversion), which results in a maximum of the torque [6, Chapter 6.4]. In this study, a marching vulcanization was always found and the last torque data point of each measurement was defined as the maximum torque $|M_{max}^*|$. Other important parameters of such a vulcanization curve are e.g. the t_{90} time (see Fig. 6.22 a)), which is a measure of the time needed for vulcanization of the rubber material. It is defined as the time between the onset of the vulcanization reaction (i.e. the torque minimum $|M_0^*|$) and the point, where $|M^*|$ increased by 90 % of $\Delta|M^*| = |M_{max}^*| - |M_0^*|$. The time derivative of the torque, $d|M^*|/dt$, can be interpreted as a cure rate [171].

The higher temperature of 180 °C results in a lower viscosity of the unvulcanized sample, thus $|M_0^*|$ is slightly lower than for a curing temperature of 160 °C. However, the higher vulcanization temperature increases the vulcanization rate and hence $|M^*|$ increases faster. This is shown in

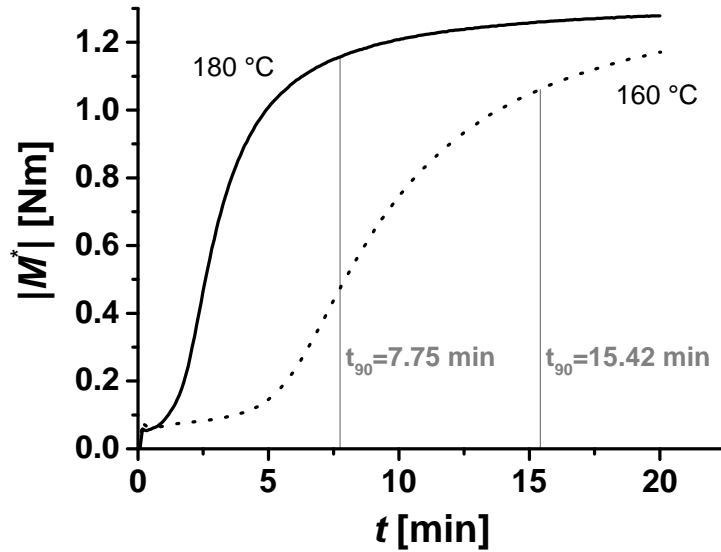


Figure 6.23.: Curing curve of the sample with $\phi = 0.154$ N121 CB at two different temperatures ($T = 160^\circ\text{C}$ and 180°C , V50) with a strain amplitude of $\gamma_0 = 0.05$ (test I(160-0.05-20)-L-S and I(180-0.05-20)-L-S). At higher temperatures $|M_0^*|$ is slightly decreased, but the vulcanization rate is higher, which results in a faster increase of the torque and thus a lower t_{90} .

Fig. 6.23 for the S-SBR filled with $\phi = 0.154$ of N121 CB. The t_{90} at 180°C is only half of the t_{90} at 160°C . Also $|M_{max}^*|$ is increasing due to the marching vulcanization, which results in a higher cross-link density after 20 min for the sample vulcanized at 180°C .

The influence of the CB volume fraction and the CB grade on the vulcanization behavior of the S-SBR is shown in Fig. 6.24. The absolute values of the minimum and the maximum torque, $|M_0^*|$ and $|M_{max}^*|$, are increasing with increasing ϕ and the samples filled with N121 show higher torque values than those filled with N660 CB. This is consistent with the results from Section 6.1.4, where it was found that the modulus, and hence also the torque, are increasing with increasing CB-polymer interface. The interface is larger for compounds filled with particles of the N121 CB grade, because the particles of this grade have a higher specific surface area than the particles of the N660 grade. The t_{90} time is influenced by the CB grade and the CB concentration in a different manner. The higher the CB volume fraction ϕ the lower is t_{90} and thus the faster is the vulcanization. This is consistent with the work of Li et al. [172], where an increase of the conversion rate with increasing specific surface area of the CB was found for the vulcanization of ethylen-propylen-diene-monomer (EPDM) rubber filled with various different CB grades.

In Fig. 6.25, the change of the nonlinear parameter $I_{3/1}$ is shown together with the time deriva-

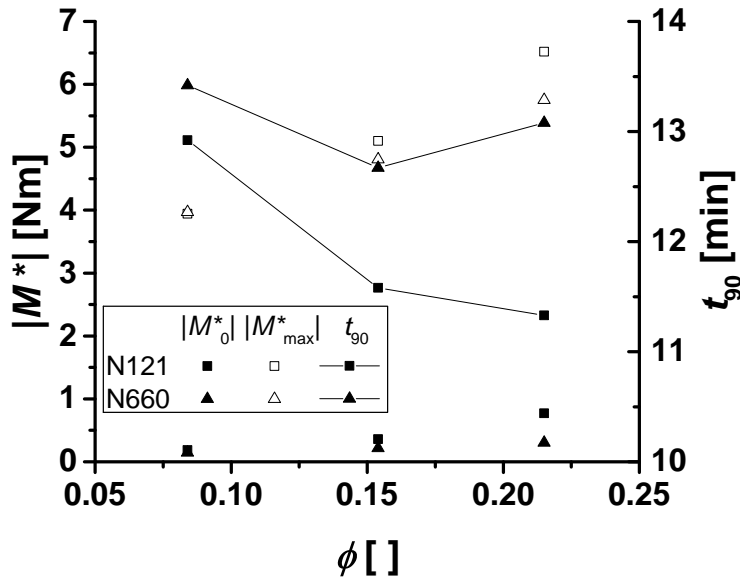


Figure 6.24.: Influence of ϕ and the CB grade on $|M_0^*|$, $|M_{max}^*|$ and t_{90} (test S-L-I(160-0.05-20)-L-S, $T = 160^\circ\text{C}$, $\gamma_0 = 0.5$, V50). With increasing ϕ , $|M_0^*|$ and $|M_{max}^*|$ increase. The samples with N121 have the higher torque. For t_{90} , no clear influence of ϕ is seen, but N660 has a slightly higher t_{90} than N121.

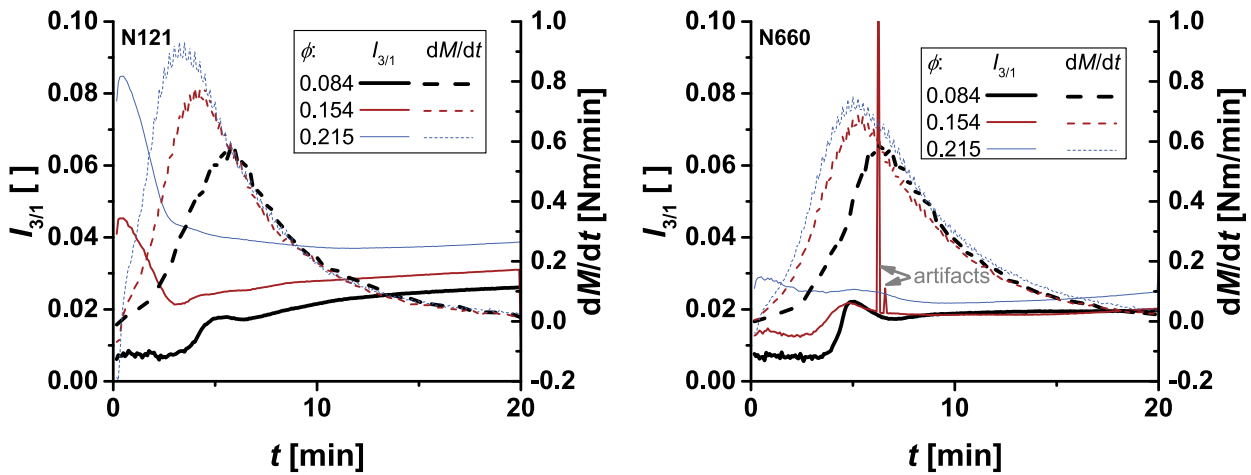


Figure 6.25.: Influence of ϕ on $I_{3/1}$ (full lines) and the derivative of the torque (dashed lines) during vulcanization (test S-L-I(160-0.50-20)-L-S, V50) for samples filled with N121 (left) and N660 (right). A peak of $I_{3/1}$ is found at approx. 5 min for all samples. For the samples with $\phi = 0.154$ and 0.215 N121 and N660, an additional peak is seen at 1 min. The two peaks marked with arrows in the right graph are probably artifacts of the FT.

tive of the torque during the vulcanization (test S-L-I(160-0.50-20)-L-S) for the S-SBR filled with different amount of N121 and N660 CB. For all other tests, the strain amplitude during curing was $\gamma_0 = 0.05$ and the results were too noisy to determine any features of the vulcanization process. For test S-L-I(160-0.50-20)-L-S the strain amplitude was $\gamma_0 = 0.05$ and thus the nonlinear parameter was less noisy. The nonlinear contribution $I_{3/1}$ shows a peak at approximately 5 min for the

samples filled with N660 and with $\phi = 0.084$ N121, which is close to the time of the maximum curing rate, which was between 3.5 min and 6.5 min for all six samples. For the other two samples ($\phi = 0.154$ and 0.215 N121) the pronounced peak in $I_{3/1}$ is found at shorter times (1 min). For all samples, $I_{3/1}$ approaches a plateau value at longer times. Leblanc [171] found a similar pattern of the third higher harmonic contribution during the vulcanization of CB filled EPDM, i.e. a peak in $I_{3/1}$ at times close to the maximum curing and another increase towards a plateau value during the further course of the vulcanization. He attributed the occurrence of the peak with the transition from a nonlinear viscoelastic fluid to a nonlinear viscoelastic solid during the vulcanization. He also detected a peak in $I_{2/1}$ at times below the maximum cure rate. This was also seen here in this study for most of the samples, but the position and height did not show a trend regarding CB content or grade and varied over a wide range of times.

All in all is the nonlinear contribution during the vulcanization reaction too low to show significant variances at strain amplitudes low enough to limit their influence on the properties of the final product. This will be discussed in the next section. It was found, that with increasing filler content the nonlinear contribution is increased during the vulcanization test and the values for the N121 filled samples are higher than the ones for the N660 filled samples, which coincides with the larger interface area in these samples.

6.2.2. FT-Rheology of vulcanized rubber

In this section, the linear and nonlinear rheological properties of the vulcanized, CB filled S-SBR are investigated under LAOS and compared to the results found on the unvulcanized samples (Section 6.1.4).

The influence of the covalent network structure on the modulus $|G^*|$ and the nonlinear stress contribution $I_{3/1}$ was investigated by comparing the results of the LAOS strain amplitude tests ($\omega_1/2\pi = 0.2$ Hz, $T = 80$ °C) before and after the isothermal test with $\gamma_0 = 0.05$ and $T = 160$ °C (Test S-L-I(160-0.05-20)-L-S). This is shown in Fig. 6.26 for the S-SBR samples filled with different amounts of N121 CB. After the isothermal vulcanization (open symbols) the modulus of the compounds is increased. With decreasing filler content is the increase of the modulus more pronounced. If more filler is added to the compound, more physical cross links should already be

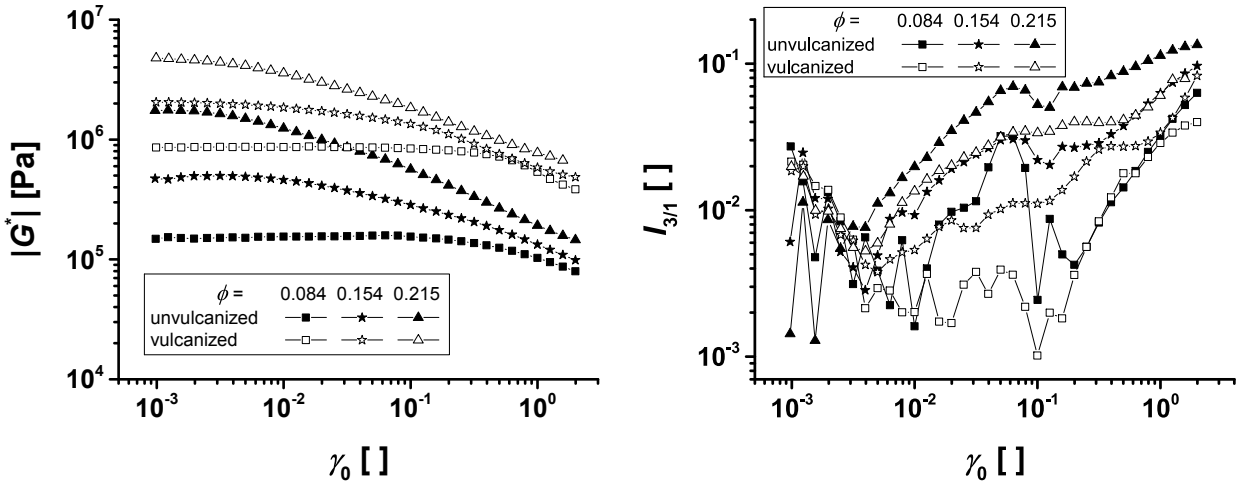


Figure 6.26.: Influence of the permanent network on the absolute value of the complex modulus, $|G^*|$, (left graph) and the nonlinear stress contribution, $I_{3/1}$, (right graph) for the samples filled with different concentrations of N121 CB (test S-L-I(160-0.05-20)-L-S, LAOS test before and after the isothermal vulcanization) measured on the V50 rheometer. The modulus is increased for all samples after the vulcanization, due to the permanent cross links. The nonlinear parameter shows a different behavior. For all samples, the influence of the peak at strain amplitudes of $0.01 < \gamma_0 < 0.1$ is decreased. Additionally, $I_{3/1}$ decreased for the samples with $\phi = 0.154$ and 0.215 at higher amplitudes, whereas no change is seen for the sample with $\phi = 0.084$.

present in the unvulcanized compound and less influence of the additional covalent network on the rheological properties of the compound is expected. The nonlinear parameter $I_{3/1}$ is changed in a different manner. The first remarkable difference is the decrease of the peak in $I_{3/1}$ at strain amplitudes $0.01 < \gamma_0 < 0.1$, which was found in most measurements on the V50 rheometer and is most probably caused by instrumental noise as discussed in Section 3.2. The second observation is, that for the samples with $\phi = 0.154$ and 0.215 , $I_{3/1}$ is decreased after the vulcanization for the whole range of strain amplitudes tested. For the sample with $\phi = 0.084$, this is only observed at $\gamma_0 > 1$.

For the decrease of $I_{3/1}$ at low strain amplitudes, several explanations are possible, which can all be related to the covalent network structure present in the vulcanized systems. According to the literature [26, 109], secondary flows are present in unvulcanized samples measured in rubber rheometers due to the closed geometry as was discussed in Chapter 3. These secondary flows might increase the nonlinear contributions for the unvulcanized samples and thus explain the lower values of $I_{3/1}$ for the vulcanized samples, which are not able to flow. The possible orientation of the filler particles by the applied deformation should also be hindered by the permanent network structure. This would become more important at higher filler volume fractions, when the CB agglomerates

form a physical network structure.

The strain history also has an impact on the rheological properties of the compounds. This is demonstrated in Fig. 6.27 for the four different test (conducted on the sample with $\phi = 0.084$ N121 CB) for which a vulcanization temperature of 160°C was used.

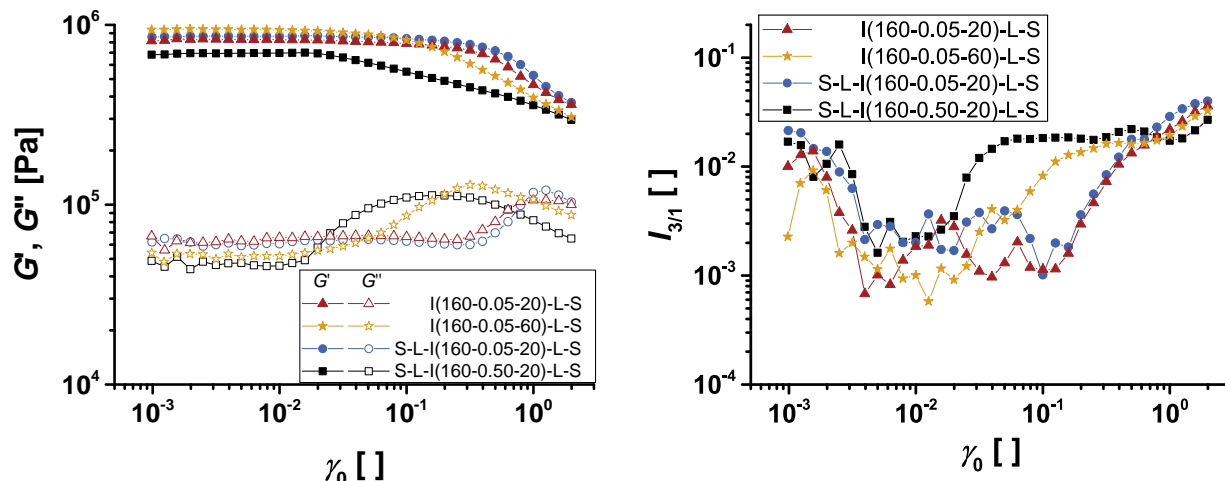


Figure 6.27.: Influence of strain history on the shear modulus (left graph) and on $I_{3/1}$ (right graph) for the sample with $\phi = 0.084$ N121 CB measured on the V50 rheometer. Test I(160-0.05-20)-L-S and S-L-I(160-0.05-20)-L-S gave similar results. Test S-L-I(160-0.50-20)-L-S differs most from the other tests, due to the larger strain amplitude used ($\gamma_0 = 0.5$ instead of $\gamma_0 = 0.05$), whereas test I(160-0.05-60)-L-S, for which the vulcanization time was longer (60 min), shows intermediate behavior.

Test I(160-0.05-20)-L-S and I(160-0.05-60)-L-S both started directly with the isothermal vulcanization test. They only differ in the length of the isothermal vulcanization, which was 20 min and 60 min, respectively. However, their rheological properties differ. The sample of test I(160-0.05-60)-L-S shows a higher plateau value in G' , a lower G'' and a shorter linear viscoelastic regime, i.e. G' starts to decrease at lower strain amplitude and the maximum of G'' is shifted to lower γ_0 , than the sample of test I(160-0.05-20)-L-S. The nonlinear contribution $I_{3/1}$ also starts to increase at smaller γ_0 for the sample of test I(160-0.05-60)-L-S.

The linear and nonlinear rheological properties (G' , G'' and $I_{3/1}$) of the sample measured by test S-L-I(160-0.05-20)-L-S are very similar to the one of I(160-0.05-20)-L-S.

Finally, for the sample of test S-L-I(160-0.50-20)-L-S the lowest storage modulus is found. Additionally, the strain amplitude for the onset of the nonlinear viscoelastic regime (where G' and G'' start to deviate from their respective plateau values) is more than one decade lower than the one for tests I(160-0.05-20)-L-S and S-L-I(160-0.05-20)-L-S ($\gamma_0 = 0.01$ and $\gamma_0 = 0.4$, respectively).

Also $I_{3/1}$ is increasing already at $\gamma_0 = 0.02$ and shows a pronounced plateau at strain amplitudes of $0.1 < \gamma_0 < 1$.

From all these observations it can first be concluded that the change of the storage modulus G' , the loss modulus G'' , and the nonlinear parameter $I_{3/1}$ are related. All three change for the samples in a similar manner and are most probably related to each other. When G' starts to deviate from its low strain plateau value, G'' and $I_{3/1}$ start to increase. The relation between G' and G'' is also known from literature (e.g. [16, 55]), where the maximum of G'' is usually found at the same strain amplitude as the maximum derivative of the G' decrease. This behavior is usually attributed to the amount of filler-filler and filler-polymer interactions. The better the interactions, the higher is the strain amplitude above which the nonlinear behavior is found [16, 55].

Because the results of test I(160-0.05-20)-L-S and test S-L-I(160-0.05-20)-L-S are very similar, the additional SAOS frequency and LAOS strain amplitude tests on the unvulcanized samples prior to the isothermal vulcanization seem to have no significant influence on the rheological properties of the compound. Before the vulcanization started, the viscosity of the polymer matrix is still low, especially when the heating to the vulcanization temperature starts. Thus the network structure, which might be partly destroyed during the first LAOS test in test S-L-I(160-0.05-20)-L-S (see discussion in Section 6.1.4) could be reformed. Thus the samples of both tests (I(160-0.05-20)-L-S and S-L-I(160-0.05-20)-L-S) would have the same properties in the vulcanized state.

For the other two test methods (S-L-I(160-0.50-20)-L-S, I(160-0.05-60)-L-S) used, the situation is different, which might be related to the higher total deformation during the vulcanization reaction in these test methods. The strain amplitude used during the vulcanization in test S-L-I(160-0.50-20)-L-S is ten times higher than in the other tests, whereas in test I(160-0.05-60)-L-S, the sample was sheared for a much longer time (60 min instead of 20 min). These higher total deformation happened during the vulcanization, when the permanent network is already partially formed and the viscosity of the matrix is increased. Hence the reformation of the physical network structure is expected to be hindered by the covalent network already formed. This would result in a weaker physical network at the beginning of the LAOS strain amplitude test for the vulcanized sample.

The results for the sample of test I(180-0.05-20)-L-S with the higher vulcanization temperature (not shown in the graphs) are also in line with this explanation. They also display the onset of

nonlinear viscoelastic behavior at smaller strain amplitudes compared to the results for tests I(160-0.05-20)-L-S and S-L-I(160-0.05-20)-L-S even though the overall deformation is the same as in test I(160-0.05-20)-L-S (vulcanization for 20 min at $\gamma_0 = 0.05$). However, due to the higher temperature in the isothermal test, the covalent network structure is formed faster (see Fig. 6.23) and thus the physical network is sooner hindered in its reforming by the formed cross-links and thus weakened in the following LAOS strain amplitude test.

7. Evaluation of FT-Rheology for the quantification of fatigue in filled rubber materials

7.1. Theoretical background

There are two main types of mechanical failure in vulcanized rubbers. If the deformation of a rubber is continuously increased during a tensile test, the sample will rupture at a certain deformation, because the segments of the network are stretched as far as possible and the covalent bonds of the network will eventually break. The maximum deformation until the rubber material ruptures in such a test is called elongation at break and the corresponding load is the ultimate stress [77, Chapter 3.4.3]. The second type of failure in rubber materials is observed, when a deformation below the elongation at break is applied in a cyclic manner over a certain period of time [173]. This is the so called fatigue, the gradual destruction of rubber over time due to dynamic motions [174]. The number of cycles a rubber can withstand under a certain oscillatory deformation is called the fatigue life, N_f [174].

Fatigue is not a unique property of rubber materials, it is also known for other elastic solids like metals. The fatigue properties of metals are often displayed in Wöhler curves, in which the applied stress is plotted as function of the corresponding fatigue life [175, Chapter 4]. In Fig. 7.1, a typical Wöhler curve is depicted. At low stress, the investigated sample does not show any failure, hence the fatigue life N_f is infinite and there is a minimum stress, the fatigue limit σ_{\min} , needed that fatigue can be measured [175, Chapter 4]. Above σ_{\min} , N_f decreases with increasing σ and the relation between N_f and σ can often be described by a power law [175, Chapter 4].

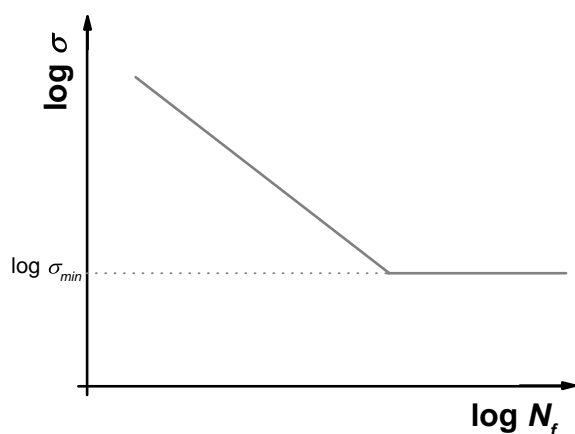


Figure 7.1.: Typical Wöhler curve. The applied stress σ is plotted as function of the corresponding fatigue life N_f , i.e. the number of cycles until failure. Below a certain stress, the fatigue limit σ_{\min} , the sample does not get destroyed and hence the fatigue life is infinite. For larger stresses, the fatigue life decreases and the stress as function of N_f can be described by a power law.

The reasoning behind this failure type in rubber is the formation of small cracks within the specimen or on its surface, which are either already present in the neat compound or are caused by the applied deformation [173]. These cracks grow over time until eventually the specimen ruptures. Rubbers are often used in applications, in which they have to withstand large static and dynamic strains or stresses [176], therefore, the fatigue behavior is an important property and was and still is the focus of many studies in the last decades [177]. The fatigue life is usually tested in uniaxial tension/compression under either controlled stress or controlled deformation conditions. For rubber, controlled deformations are preferred, because the instruments needed are simpler, the test conditions correspond better to the failure conditions in real life applications [77, Chapter 8] and the creep of the samples is circumvented [178]. Especially highly filled elastomers under large loads/deformations are prone to show a heat-build up [179], because the viscous energy is dissipated and the thermal conductivity is low.

For the theoretical treatment of rubber failure, two different approaches are used: the crack nucleation approach and the crack growth approach [176]. The crack nucleation approach is based on the investigation of the crack nucleation as a function of parameters like the strain, stress or strain energy density [176, 178, 180]. The second approach focuses on the growth of single cracks, for example in terms of the tearing energy, and thereby estimating the life time of the rubber [173, 176, 179]. An important parameter for the fatigue life is the R ratio (R), which is defined as the minimum load/deformation divided by the maximum load/deformation during a cycle [181]. The R ratio is illustrated in Fig. 7.2 for the example of non-relaxing tension experiments, for which R

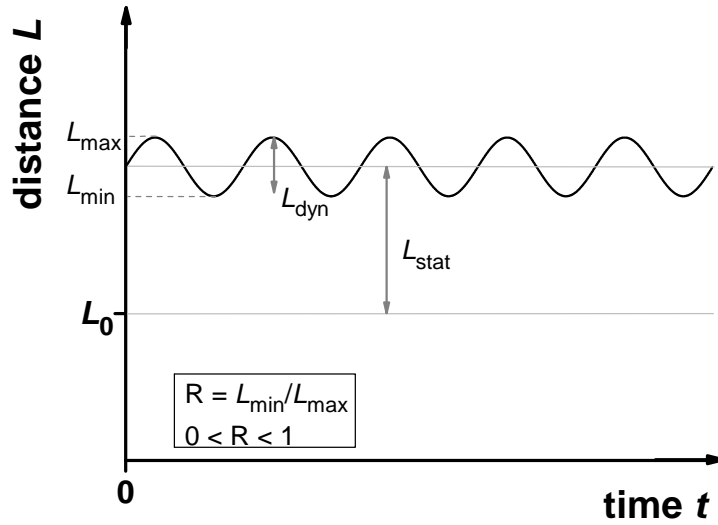


Figure 7.2.: Tension experiment. The R ratio is defined as the lowest distance used during the measurement L_{min} divided by the largest L_{max} . For a positive R ratio, the static deformation L_{stat} must be larger than the amplitude of the dynamic deformation L_{dyn} .

is between 0 and 1. For fully relaxing tension measurements ($L_{min} = 0$) R is 0 and for symmetric tension-compression cycles (no static load, $L_{min} = -L_{max}$) R is -1 [177]. Le Cam et al. [177, 182] showed in their work, that the R ratio has an effect on the kind of damage in filled natural rubber. They found that for negative R ratios (change between tension and compression) the dumbbell specimen ruptured due to a large straight external crack at the surface of the median section, whereas in specimen under non-relaxing tension (R ratio between 0 and 1), the crack formed at the surface in the median section is branched and additional cohesive internal cracks appeared below the metallic inserts where the sample was fixed. It was also reported in literature that increasing the minimum stress increases the fatigue life at constant strain amplitude by more than a factor of 10 for filled EPDM and SBR [183]. For negative R ratios, the fatigue crack growth is considerably increased, which reduced the fatigue life [179]. It was also reported that the frequency of the excitation does not have a significant influence on the fatigue life N_f , as long as the heat build-up is limited [179].

The initiation of cracks in rubbers has many origins. This includes cracks or defects already present in the compound before testing, such as uneven surfaces. The breakup of CB agglomerates, and cavitation close to the CB-polymer interface, when the adhesion between rubber and CB is broken, are further possible reasons for the formation of new cracks in the material [182]. During

a cyclic deformation of a sample, as soon as a defect is present in the material, the increased local stresses at its tip are supposed to result in the growing of the defect until eventually the material fails [184].

Kadar et al. [185] applied FT rheology on the investigation of fatigue phenomena in polypropylene and polymer-metal sandwich composites and could detect higher nonlinear contributions, which changed over time and could also be correlated to delamination processes in the sandwich composite during temperature sweep tests.

7.2. Samples

For the investigation of the fatigue life, four different series of vulcanized samples were used. They all consisted of the same basic recipe but different parameters were systematically changed. In the first series (five samples), the amount of accelerator (DCBS = *N,N*-dicyclohexyl-2-benzothiazole sulfenamide, Fig. 7.3) was varied between 0.75 phr and 1.75 phr. In the second series (nine samples),

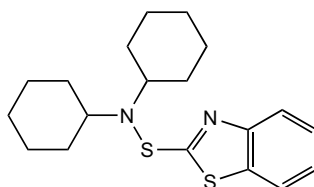


Figure 7.3.: Accelerator *N,N*-dicyclohexyl-2-benzothiazole sulfenamide (DCBS)

the matrix polymer was changed from 100 phr natural rubber (NR) to various mixtures of NR, SBR and butadiene rubber (BR). In the third series (five samples) different anti-aging additives were used and in the fourth series (13 samples) the amount of CB (grade N339) was changed from 0 phr to 60 phr. The recipe of the last series is the same as the one used in the previous sections for the shear rheological tests (see Chapter 6). All samples were received already vulcanized from Continental Reifen Deutschland in form of rectangular stripes with dimensions of approximately 50 mm·10 mm·2 mm.

7.3. Results

7.3.1. Tension measurements

In order to analyze the nonlinear rheological properties of the samples, all compounds were tested on the Gabo Eplexor 150N (Gabo Qualimeter Testanlagen GmbH, Ahlden, Germany). This is an instrument for dynamic mechanical thermal analysis (DMTA) with two separate motors and shown in Fig. 7.4.

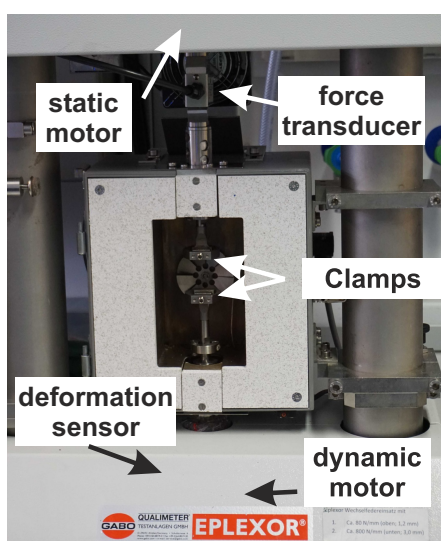


Figure 7.4.: Setup of the Gabo Eplexor DMTA machine. For the tension measurements, the geometries are clamps. The upper clamp is connected to the force transducer and the upper motor, which applies the static force/deformation. The lower clamp is connected to a displacement transducer (not visible) and the lower motor for the dynamic deformation/force.

The upper geometry is connected to the force transducer and the upper motor, which applies the static force or deformation. The lower geometry is connected to a deformation sensor for the dynamic movement, which is applied by the lower motor. For the nonlinear data analysis, the raw data of the dynamic deformation sensor and the force sensor were recorded with an external ADC card and analyzed with a Matlab code, based on the code developed by C. Eberl and M. Funk from the Institute of Applied Materials at the Karlsruhe Institute of Technology. The samples were measured in tension at room temperature with controlled deformation. Due to the sample holder (clamps) and the shape of the specimen (rectangular sheets), only positive R ratios were possible, i.e. a static deformation at least as large as the amplitude of the dynamic deformation is needed in order to prevent the bending of the specimen (Fig. 7.2).

The applied dynamic deformation was limited by the dynamic range of the deformation sensor, which was ± 2.5 mm. The length of the specimen between two clamps was typically 30 mm. Thus the maximum possible dynamic extension was usually $\varepsilon_0 = \pm 0.08$. As a consequence, the samples did not rupture during the measurements, as the fatigue life was too high at these dynamic deformations. This is illustrated in Fig. 7.5, where no change of Young's modulus is seen during the measurement time (10^5 s), which corresponds to a fatigue life larger than $5 \cdot 10^5$ cycles. The nonlinear data (Fig. 7.6) does also not show any sig-

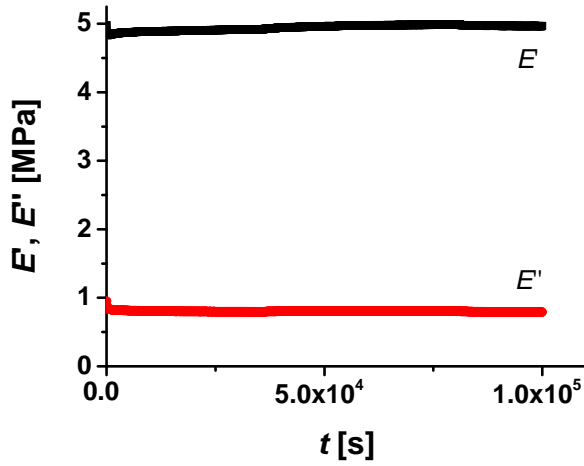


Figure 7.5.: Storage and loss Young's modulus (E' and E'' , respectively) as function of measurement time t for the sample filled with 40 phr N339 CB at a dynamic extension of $\varepsilon_0 = 0.12$ ($f = 5$ Hz, $T = 35$ °C, $\varepsilon_{stat} = 0.20$, Gabo Eplexor). The modulus did not change within the measurement time (10^5 s).

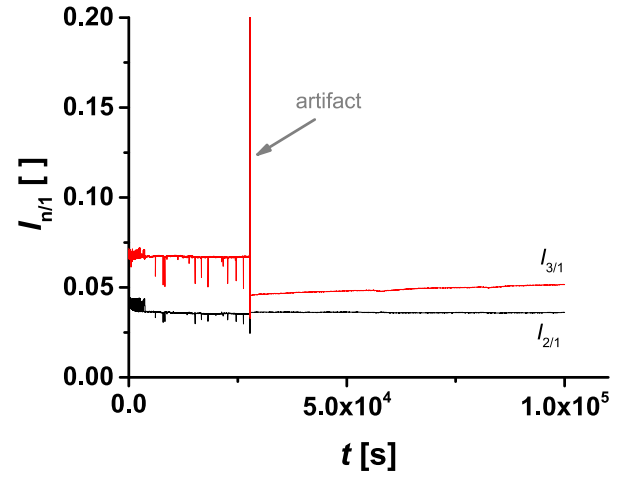


Figure 7.6.: Higher harmonic contributions ($I_{2/1}$, $I_{3/1}$) as function of measurement time t for the sample filled with 40 phr N339 CB at $\varepsilon_0 = 0.12$ ($f = 5$ Hz, $T = 35$ °C, $\varepsilon_{stat} = 0.20$, Gabo Eplexor). The nonlinear data do not show a significant change within the measurement time (10^5 s), only the odd higher harmonics are slightly increasing. The peak in $I_{3/1}$ marked with an arrow and the subsequent lower values of $I_{3/1}$ are most probably due to artifacts of the FT.

nificant change, only the odd harmonic $I_{3/1}$ is slightly increasing. One further observation of the fatigue measurements is that the even higher harmonic contribution $I_{2/1}$ is almost as high as the odd harmonic contribution $I_{3/1}$. The presence of even higher harmonic contributions may have several reasons. First, the strain excitation is not symmetric due to the applied static deformation ε_{stat} . Thus Eq. 2.14 (p. 10) has to be used in Hooke's law (Eq. 2.3, p. 6) instead of Eq. 2.15. Second, Hooke's law is not a good approximation of the rheological behavior of elastomers in tension. Instead, rubber materials are better described in tension by the Neo-Hookean law (Eq. 7.1).

$$\sigma = \frac{E_0}{3} \left(\lambda - \frac{1}{\lambda^2} \right) \quad (7.1)$$

In this equation E_0 is the Young's modulus of the elastomer at small deformations and λ is the deformation ratio $\lambda = \varepsilon_0 + 1$. Due to the quadratic term $1/\lambda^2$, the FT of the Neo-Hookean law displays odd and even harmonic contributions in the nonlinear viscoelastic regime. Third, if cracks would be present during the measurement, these cracks would most probably not be symmetrically oriented in the rubber material. Instead an asymmetric orientation is more probable and thus the

rheological behavior of the sample would be anisotropic under the applied deformation.

Due to the limited dynamic deformation possible on the Gabo Eplexor, the focus of the research was changed from the investigation of the fatigue life to the investigation of changes introduced by thermal aging into the samples. Therefore, the samples were measured for a short time (30 min) at $\nu_1 = 10$ Hz with a dynamic extension of $\varepsilon_0 = 0.03$ ($T = 25$ °C, $\varepsilon_{\text{stat}} = 0.20$). In a second test series another specimen of each sample was heated for 7 days at 70 °C in a drying oven without vacuum to induce thermal aging of the samples. These specimen were then measured under the same conditions as the samples without thermal aging.

Typical results of these tests are shown in Figs. 7.7 and 7.8 for the linear and nonlinear data of the samples with different amount of vulcanization accelerator DCBS. In both, $\tan \delta$ and the

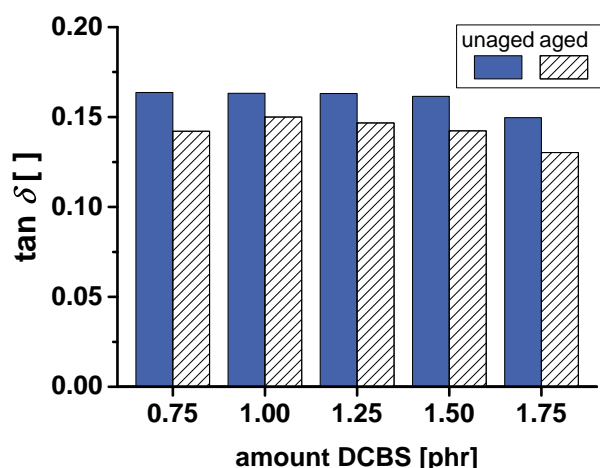


Figure 7.7.: Loss factor $\tan \delta$ after 10^3 s for the samples with different amount of DCBS at a dynamic extension of $\varepsilon_0 = 0.03$ with and without aging for 7 days at 70 °C ($\nu_1 = 10$ Hz, $T = 25$ °C, $\varepsilon_{\text{stat}} = 0.20$, Gabo Eplexor). For the aged samples $\tan \delta$ is 8% to 13% lower.

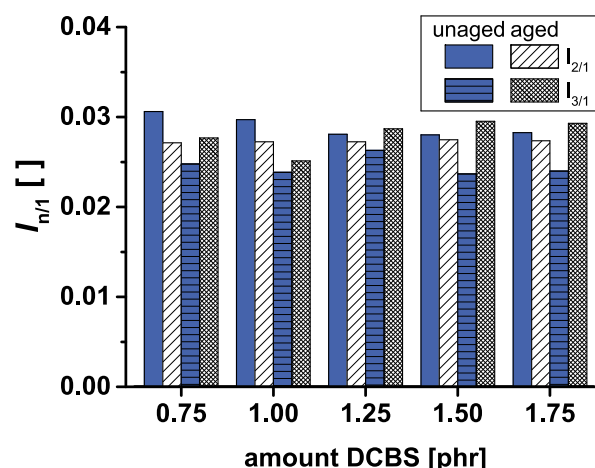


Figure 7.8.: Relative first higher harmonics ($I_{2/1}$, $I_{3/1}$) after 10^3 s for the samples with different amount of DCBS at a dynamic extension of $\varepsilon_0 = 0.03$ with and without aging for 7 days at 70 °C ($\nu_1 = 10$ Hz, $T = 25$ °C, $\varepsilon_{\text{stat}} = 0.20$, Gabo Eplexor). The aged samples show slightly larger values of $I_{3/1}$ and lower values for $I_{2/1}$.

relative higher harmonic contributions, no influence of the DCBS content is visible. The aging lead to a decrease of $\tan \delta$ by 8% to 13%, which could be explained by additional crosslinking caused by the possible reaction of oxygen with the remaining double bonds in diene rubbers during thermal aging. $I_{3/1}$ is increased up to 25% and $I_{2/1}$ slightly decreased ($\leq 10\%$) to the thermal aging. To estimate the error of a measurement in $\tan \delta$, two specimen of the sample with 1.25 phr DCBS were measured. The deviation of $\tan \delta$ was 1%. For all other test series, similar results were found, i.e.

a small decrease of $\tan \delta$ and a small increase of $I_{3/1}$ after thermal aging.

The quantification of the fatigue and aging behavior of CB filled elastomers by FT-Rheology with the Gabo Eplexor was not successful in this work. This had two main reasons. First, the possible dynamic deformations that can be applied on the instrument are below the fatigue limit of rubber materials and thus the fatigue life can not be determined. Second, the excitation of the instrument does also contain higher harmonic contributions. The magnitude of these higher harmonic contributions is in the range of those measured for the force response, as can be seen from Fig. 7.9. Hence the nonlinear results from the force response are largely influenced by the excitation signal.

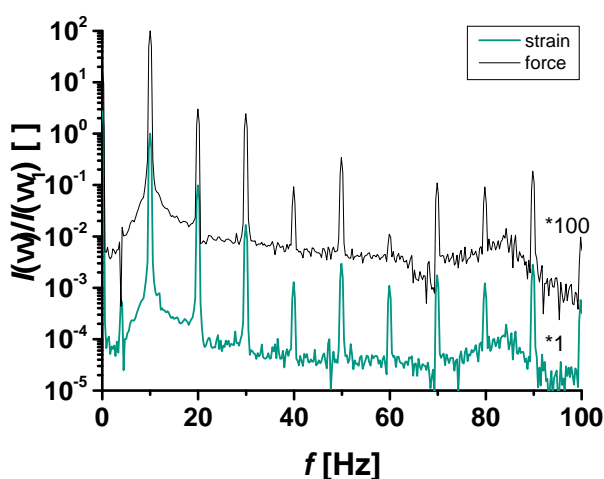


Figure 7.9.: FT magnitude spectra of the strain excitation and the force response (magnified by a factor of 100) for the sample with 0.75% DCBS without aging ($\varepsilon_0 = 0.03$, $\nu_1 = 10$ Hz, $T = 25$ °C, $\varepsilon_{\text{stat}} = 0.20$, Gabo Eplexor).

Additionally, the calculation of the higher harmonic contributions with the Matlab software is tedious and a high amount of data is produced. For one measurement of 28 h at a frequency of 10 Hz with a sampling rate of 200 point per cycle more than 2 GB raw data were saved.

7.3.2. Torsion measurements

Due to the limited deformations possible in the tension measurements on the Gabo Eplexor and the tedious data analysis, the sample with 45 phr N339 CB was also measured on the ARES G2. In contrast to the Eplexor, the ARES G2 is a shear rheometer not a DMTA. Therefore, the measurements were performed in torsion. In torsion, no static deformation is needed, hence the R ratio was 0. To further enhance the fatigue, the measurements were done at 120 °C under air to induce thermal aging.

In Figs. 7.10 and 7.11 the storage modulus and the higher harmonic contributions $I_{3/1}$ and $I_{2/1}$ are shown as function of the applied cycles for a strain amplitude of $\gamma_0 = 1$ for three specimens ($T = 120^\circ\text{C}$, air, $\omega_1/2\pi = 1$ Hz). The failure of the sample can be clearly seen by the sudden, large

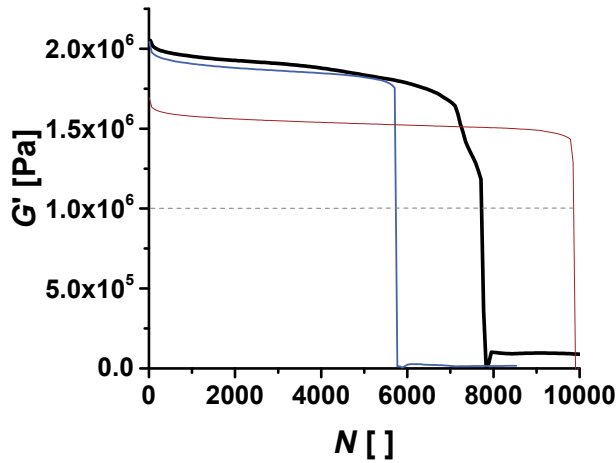


Figure 7.10.: Storage modulus of the sample with 45 phr N339 CB as function of cycles N measured in torsion on the ARES G2 ($T = 120^\circ\text{C}$, air, $\omega_1/2\pi = 1$ Hz, $\gamma_0 = 1$). The moduli suddenly decrease when the sample fails. The dashed line marks a modulus of 1 GPa, which was used to determine the fatigue life.

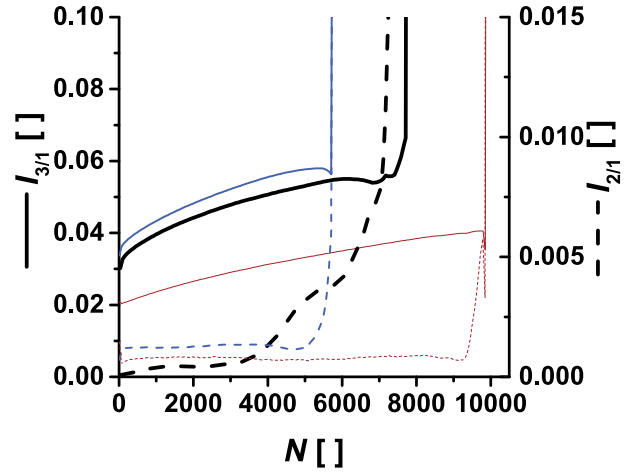


Figure 7.11.: Relative second (dashed lines) and third (full lines) higher harmonic contribution of the sample with 45 phr N339 CB as function of applied cycles N measured in torsion on the ARES G2 ($T = 120^\circ\text{C}$, air, $\omega_1/2\pi = 1$ Hz, $\gamma_0 = 1$). During the measurement $I_{3/1}$ is monotonically increasing until the sample fails and then $I_{3/1}$ increases rapidly. The even harmonic $I_{2/1}$ is almost constant until the sample ruptures and $I_{2/1}$ increases fast. Only for one of the samples $I_{2/1}$ increases already far before the sample ruptures.

drop of the storage modulus and an increase of the nonlinear contributions, respectively. This indicates the full rupture of the sample and the measured values after this point are either noise or artifacts from friction between the two separated parts of the specimens. The storage modulus is decreasing over time whereas $I_{3/1}$ is increasing. This both indicates a continuous destruction of the rubber structure before the specimens eventually break. The even harmonic contribution $I_{2/1}$ is more than a factor of 10 lower than $I_{3/1}$ and almost constant until the sample ruptures and the relative intensity of $I_{2/1}$ drastically increases. For one of the samples, $I_{2/1}$ already starts to increase long before the sample actually breaks, which might be an indication for the formation of cracks in the sample. These cracks would result in an anisotropy in the sample and thus explain the presence of even higher harmonics in the torsion experiment. The fatigue life N_f of the samples was determined by the time, at which the storage modulus dropped below a (arbitrarily assigned)

value of 1 GPa for all amplitudes used (see dashed line in Fig. 7.10). The fatigue life is shown in figure Fig. 7.12 as function of the strain amplitude (the axes in the plot are inverted compared to a Wöhler curve, see Fig. 7.1). A power law behavior between the applied deformation and the fatigue

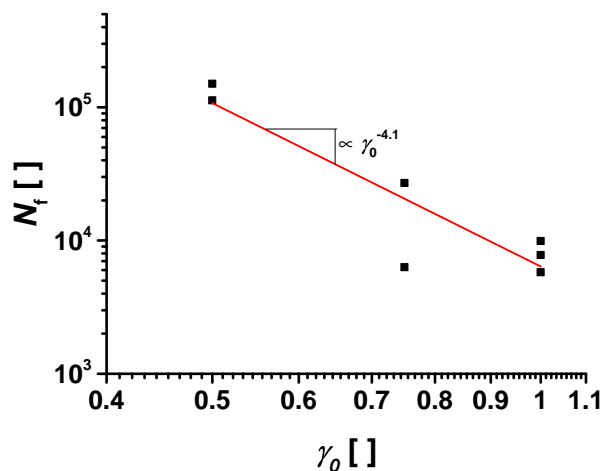


Figure 7.12.: Fatigue life of the sample with 45 phr N339 CB as function of the applied strain amplitude measured in torsion with the ARES G2 ($T = 120^\circ\text{C}$, air, $\omega_1/2\pi = 1$ Hz).

life with a scaling exponent of -4.1 ± 0.8 was found. To verify this finding, more measurements are needed to due to the large error in N_f . At $\gamma_0 = 0.75$ the fatigue life of the two specimen differs for example by a factor of 4.

The large error of N_f has at least two reasons. First, the samples used for $\gamma_0 = 0.75$ and 1 were cut manually with a scissor to shorten them. This was done in order to reduce the risk of damaging the motor during long term testing of the samples at high deformation rates. The absolute deformation of the motor applied for a certain strain is proportional to the length of the sample and hence shortened. The cutting on one hand introduces roughness to the surface of the specimen, which increases the nucleation of cracks, on the other hand the cutting was not perfectly horizontal which results in changes of the specimens width. The stress is concentrated at the point with the smallest width, so the samples with an uneven width are prone to earlier failure. The second reason for the high error is the difficulty in fixing the sample to the clamps. During the fixing it is most likely to slightly bend the sample, which can already destroy some CB agglomerates and thereby change the crack initiation behavior. Another problem with the system is the rectangular shape of the specimen. For these specimens the stress is concentrated at the edges to the clamps and indeed, all specimen broke close to one of the clamps. This problem could be avoided by using dumbbell shaped specimens or even better rotational symmetric dumbbell (also called diabolos or

dumbbell of revolution) specimen [177, 182] in the future.

Another possibility for future investigations of the fatigue life are time-dependent measurements of the samples in rheometers with a closed cavity (such as the V50 or the RPS 2000) under shear. Due to the closed geometry, edge effects on the fatigue life should be reduced and the stress should be distributed more equally in the specimen than compared to torsion experiments. In these instruments also high strain amplitudes $\gamma_0 > 1$ are feasible. If fatigue measurements are performed at reduced temperatures, close to the glass transition of the rubber polymer, the fatigue life should be drastically reduced, due to the lower mobility of the polymer and thus should be easier to measure.

8. Conclusion and Outlook

Rubbers are an important material class and are used in numerous applications. In most cases these rubbers are not used as raw polymers but many additives are needed to improve their properties. Especially the use of solid fillers for the enhancement of their mechanical behavior is a common feature in rubber technology. Such filled rubbers exhibit a complex and heterogeneous structure, which has a large impact on their processing behavior and the mechanics of the final product. They often show for example nonlinear viscoelastic behavior already at small strain amplitudes compared to thermoplastic polymer melts. This increases the need for sophisticated mechanical characterization techniques in order to determine their properties and eventually develop theoretical models.

Fourier transform rheology (FT-Rheology) is a method that was already used successfully to quantify the nonlinear viscoelasticity of other complex systems, where it was found that the interface in heterogeneous systems adds an important contribution to their mechanical characteristics. In the present work this method was applied to investigate two types of rubber materials, which are also largely influenced by their internal surfaces and are industrially important: carbon black (hereinafter: CB) filled rubber materials received from a collaboration with the tire industry (Continental Reifen Deutschland) and thermoplastic elastomers, which were also synthesized in this work by anionic polymerization.

Progress in the present thesis

Fourier Transform Rheology with closed gap rheometers

The closed and pressurized geometry of rubber rheometers allows for reproducible measurements of samples with high elasticity, like filled rubbers. As one of the first steps, the rubber rheometer

used in this study (V50) was compared with an open gap rheometer (ARES G2), which is typically used for characterizing soft matter under large amplitude oscillatory shear (LAOS). It was found that, for thermoplastic polymer melts, the measured intrinsic nonlinearity Q_0 was almost three times higher on the V50 than on the ARES G2. This is most probably due to additional nonlinear contributions in the rubber rheometer caused by secondary flows at the edges of the closed geometry and the different geometry design between the two instruments (cone-cone and cone-plate). With the V50, reproducible measurements of both linear and the nonlinear parameters are possible even at amplitudes of $\gamma_0 > 0.8$. This was not possible with the ARES G2, for which the standard deviation of the shear modulus increased at higher strain amplitudes.

Nonlinear results for various samples measured under LAOS with the V50 showed the presence of a pronounced peak in $I_{3/1}$ at small strain amplitudes ($0.01 < \gamma_0 < 0.1$). Different possible reasons for the occurrence of this peak were evaluated. The first hypothesis attributed the peak to nonlinear contributions generated by deforming interfaces as was already found for emulsions of Newtonian liquids. In filled elastomers these interfaces are also present due to phase separation between the rubber matrix and additives like processing oils or sulfur. This hypothesis was disproved when the peak was also seen in measurements on a homogeneous melt of linear polystyrene, where no interfaces were present in the sample. Results from the same polymer measured on the ARES G2 did not show this peak, thus the reason must be related to the rubber rheometer itself. The second possible reason for the peak was the presence of a thin oil film on the geometry surface caused by previous measurements of filled elastomers. However, this hypothesis was also proven false. Imperfections in the strain excitation in the V50 could also be an explanation, but it is unlikely because the strain signal did not show a significant higher harmonic contribution over the strain amplitude range where the peak appeared. After a modification of the instrument by the manufacturer, where different parts of the machine were changed, the peak position was then shifted to lower strain amplitudes. Thus the additional nonlinear contributions are apparently caused by one of the parts that was changed, which includes the new geometry design, cooling unit and the enhanced motor control.

In order to evaluate the sensitivity of the V50 in relation to other rubber rheometers, a series of CB filled emulsion SBR was measured under LAOS. The data measured on the V50 was compared

with data measured by Leblanc et al. on a RPA 2000. It was found that, for the samples with high CB concentrations, the lower sensitivity limit for measurements of $I_{3/1}$ was at the same strain amplitude ($\gamma_{0,SIS} = \gamma_{0,RPA} = 0.32$) for $\phi = 0.183$ for both instruments. However, for the samples without CB, the sensitivity limit of the V50 ($\gamma_{0,SIS} = 0.2$) was three times lower than the limit of the RPA 2000 ($\gamma_{0,RPA} = 0.6$).

Synthesis and rheological characterization of thermoplastic elastomers

Thermoplastic elastomers are a polymer class that combines the processing characteristics of thermoplastic polymers with the elastic properties of vulcanized rubbers. This is possible through the use of a phase-separated system. In this work, a poly(styrene-*b*-isoprene-*b*-styrene) triblock copolymer (SIS) was chosen as a model system for thermoplastic elastomers. Anionic polymerization was used for the synthesis to make polymers with defined molecular weight, known chemical constitution, low polydispersity and without additives. Three different synthetic routes were tested: the initiation of the polymerization with a difunctional initiator, the coupling of living diblock anions and sequential polymerization. The approach with a difunctional initiator offers access to polymers with symmetric endblock lengths in a two step process. For the synthesis of diene polymers with a high content of the 1,4-*cis* isomer, apolar solvents are needed. The use of apolar solvents results in a low reactivity of the initiator, which was based on diisopropenyl benzene in this work. As a consequence, this synthesis resulted in a mixture of products, initiated by mono-, di-, and polyfunctional species. The second approach, the coupling of living anions, was also not successful. The coupling reaction was not quantitative and a high amount of diblock polymer was present in the final product. From the different coupling agents used, 1,2-bis(chlorodimethylsilyl)ethane was the most effective one, however even with this agent less than half of the final polymer consisted of triblocks. The sequential polymerization needs three monomer addition steps, which increases the probability of termination reactions, but the solvent to be switched from toluene to cyclohexane and the reaction temperature to be increased allows for the styrene polymerization with the result that well defined triblock copolymers could be synthesized. Due to the small difference in molecular weight between the diblock and the triblock copolymer, standard SEC cannot fully separate both structures and thus the exact content of triblock in the final product could not be determined.

Two of the synthesized triblock copolymers and an industrial TPE were investigated to determine their nonlinear rheological properties. Prior to this mechanical characterization, the phase morphology of the different polymers was determined with small angle X-ray scattering. In the rheological measurements, large standard deviations in both the linear and the nonlinear data made it hard to draw conclusions from the obtained results. These deviations might originate from small differences in the orientation of the polymer phases caused by external forces during the alignment of the specimen or from slip effects. A striking feature of these results was that the relative third higher harmonic contribution $I_{3/1}$ was found to be independent of the applied frequency, in contrast to findings from other polymer melts reported in the literature.

Carbon black filled rubbers under LAOS

Carbon black is an important solid filler for rubber materials. Despite its use for more than one hundred years, the structure of CB filled rubber compounds and how this changes under external forces is still not fully understood. By using Fourier Transform analysis, the influence of important parameters, like the CB volume fraction ϕ and the type of the CB particles, on the nonlinear viscoelastic behavior of rubber formulations relevant to the tire industry was studied in the unvulcanized state, during the vulcanization process and on the cured material.

In the unvulcanized material the effect of the CB volume fraction and the CB type was studied in detail. Three different CB grades (N121, N339 and N660) with different specific surface areas and shape were used. A correlation between the size of the internal surface area and the nonlinear viscoelasticity was found. If the size of the CB-rubber interface is increased, $I_{3/1}$ increased, especially at medium amplitudes ($0.1 < \gamma_0 < 0.5$). At a strain amplitude of $\gamma_0 = 0.32$, which is the lower sensitivity limit for higher harmonic contributions for the rubber materials tested, $I_{3/1}$ increased by more than a factor of 10 when the volume fraction of N339 was increased to $\phi = 0.215$, whereas the absolute value of the complex modulus $|G^*|$ increased by only a factor of three at this strain amplitude. The increase depended also on the particle type. The larger the specific surface area of a single CB aggregate, the higher was the nonlinearity. The dependence of $I_{3/1}$ on ϕ could be modeled by a one parameter equation for each CB grade. This equation is analogous to the Krieger-Dougherty equation, which is used to describe the viscosity as a function of ϕ in disper-

sions. With this model, a critical filler volume fraction, the maximum packing fraction ϕ_m , was calculated. For $\phi = \phi_m$, the filler particles are packed as densely as possible in the rubber matrix and the nonlinear contribution contains a singularity. The value of ϕ_m is a function of the CB grade and a linear relationship between ϕ_m and the OAN (oil adsorption number) of the CB grade was found. As a consequence the influence of the filler grade on $I_{3/1}(\gamma_0 = 0.32)$ vanished when $I_{3/1}$ is plotted as a function of the product of OAN and ϕ . This product can be interpreted as a measure of the overall CB-rubber interfacial area in the compound. With increasing interfacial area, more interactions between the rubber and the CB were formed, which then contribute to the nonlinear viscoelastic behavior. A high impact of the additional three-dimensional filler-filler network at higher volume fractions on $I_{3/1}$ was found when the measurements were performed at different temperatures. Only at filler concentration above the percolation threshold ($\phi_c \approx 0.14$), was the temperature dependence of $I_{3/1}(\gamma_0 = 0.32)$ detected. A decrease in the measurement temperature from 80 °C to 40 °C resulted in a more than three times lower value of $I_{3/1}(\gamma_0 = 0.32)$ when a filler-filler network was present.

The investigation of the vulcanization process by FT-Rheology was limited by the sensitivity of the instrument. When low shear amplitudes ($\gamma_0 = 0.05$) were applied during cure, the detected nonlinear contribution was very noisy, whereas at higher strain amplitudes ($\gamma_0 = 0.5$), a peak in $I_{3/1}$ was found close to the time where the cure rate reached its maximum. However, the vulcanization process and especially the final properties of the rubber were influenced by this high strain amplitude. This could be shown in LAOS measurements on the samples after curing. The higher the strain amplitude applied during vulcanization, the lower was the strain amplitudes at the onset of nonlinear viscoelastic behavior. When a strain amplitude of $\gamma_0 = 0.5$ was used during vulcanization, this onset was already found at $\gamma_0 \approx 0.02$, whereas the onset was more than one decade higher ($\gamma_0 \approx 0.3$) when a strain amplitude of only $\gamma_0 = 0.05$ was applied during vulcanization and all other parameters were kept constant. At the onset of nonlinear viscoelasticity, the storage modulus G' started to decrease, $I_{3/1}$ increased by almost one decade and the loss modulus G'' first increased and then decreased at higher strain amplitudes, whereat the height of its maximum was almost constant.

FT-Rheology to quantify the fatigue of filled elastomers

In another project, the long term stability of vulcanized, CB filled rubber materials was investigated by FT-Rheology. First experiments were conducted in tension on a Gabo Eplexor. The limited range of the dynamic deformation (± 2.5 mm) did not allow for the determination of the fatigue life. The comparison of samples with and without thermal aging (7 days at 70°C) measured over 10^3 s with a dynamic deformation of ± 0.03 showed that the nonlinear contribution was higher for the aged samples. The significance of this difference is limited because the instrument also shows a nonlinear contribution to the excitation, which was the same order of magnitude as the nonlinear contribution of the force response. In a second approach, one of the vulcanized samples was also tested in torsion on the ARES G2, which allowed for much higher deformation amplitudes, up to $\gamma_0 = 1$. On this instrument it was possible to determine the fatigue life of a filled rubber material at three different strain amplitudes as the sample was simultaneously aged at 120°C in air. During the fatigue test, $I_{3/1}$ increased monotonically. At the same time the shear modulus decreased. Both changes indicate a continuous destruction of the sample until it eventually breaks. The time where the specimen ruptures was identified by a sudden drop in G' to 0 and an increase in $I_{3/1}$ and $I_{2/1}$ to 1.

Perspective

In this work it could be demonstrated that FT-Rheology is a useful method for investigating the rheological properties of heterogeneous rubber materials in the nonlinear viscoelastic regime. However, the limited sensitivity of the current instruments restricts the application of this method to strain amplitudes $\gamma_0 > 0.1$. The minimum nonlinear contribution to the torque signal that could be measured was $8 \cdot 10^{-4}$ N m. Further development in this field of technology will also widen the application area of FT-Rheology on these samples. They can enable the quantitative detection of higher harmonic contributions during the vulcanization process at strain amplitudes that have a smaller influence on the mechanical properties of the vulcanized product than the one used in the test described here ($\gamma_0 = 0.5$).

For the CB filled elastomers investigated up to now, only three different CB grades were tested. It was possible to correlate the nonlinear contribution $I_{3/1}$ of the filled compounds with the size

of the CB-polymer interface using the oil adsorption number OAN times the filler volume fraction ϕ . Yet, the relation might still be more complex. For example, the anisotropy of the particles should also have an influence on $I_{3/1}$ as the orientation of the particles might affect the nonlinear contribution. Thus more CB grades need to be investigated, especially those with similar specific surface areas but different structures, e.g. a comparison between the grades N330, N339, N351 and so on.

The use of FT-Rheology for the measurement of fatigue in the already vulcanized rubber materials was not practical in tension and torsion, even though a change in the nonlinear properties over time could be identified. The fatigue life of filled rubbers is too high for useful measurements at the allowable deformation rates. However, the investigation of samples with a lower fatigue life, like filled thermoplastic polymers or duromers, by FT-Rheology is an interesting perspective. The vulcanization of the rubber materials in a rheometer with closed geometry, such as the V50 or the RPA 2000, and the subsequent time-dependent measurement of the fatigue life in shear. An influence of thermal aging on the nonlinear viscoelastic properties of vulcanized rubbers could be seen, however quantification was limited by the restrictions in the dynamic deformation and the high nonlinear contributions in the strain excitation of the Gabo Eplexor itself. The use of another type of applied deformation (e.g. three-point bending, bending with cantilever) could improve the obtained results. For these deformation types, the thickness of the samples is the important parameter for the applied deformation and not the sample length, as in tension and torsion experiments. The rectangular specimens used in this work are also not optimal because the forces are unevenly distributed in the sample. As a consequence, the rupture was largely influenced by the clamping of the samples. The use of rotational symmetric dumbbell shaped specimens is more appropriate and could decrease the deviations in the measured fatigue life.

The nonlinear viscoelastic properties of the TPEs were only investigated in terms of the excitation frequency and the measurement temperature. After optimization of the synthesis in this work, the investigation of compositional effects on $I_{3/1}$ and other measures of nonlinear viscoelasticity can be done. A systematic variation of the styrene content over the whole range of possible morphologies, from a disordered state to a spherical, cylindrical, bicontinuous gyroidal and a lamellar structure would be the next step. Also comparison of the SIS triblock copolymers with poly(styrene-*b*-

isoprene) block copolymers with the same molecular features (molecular weight, styrene content) is an interesting future perspective. The in-situ observation of the phase morphology during the dynamic deformation with a Rheo-SAXS combination for example would also make sense. The reproducibility of the rheological measurements needs to be improved. The reproducibility was limited in this study by the high T_{ODT} of the samples and slippage of the samples. The slippage may be reduced by using rubber rheometers with a closed geometry. At the moment these instruments need a sample volume of approximately 4 cm^3 , which is too high for samples synthesized with anionic polymerization in our laboratory. Instruments with smaller geometries would be very useful. The problem with the T_{ODT} can be circumvented by the choice of a different polymer combination where the T_{ODT} is lower, but which still can be used as thermoplastic elastomers.

For the synthesis of the copolymers, the optimization of the polymer characterization can help to further improve the yield of the triblock copolymer. With the current SEC techniques readily available it is hard to quantify the ratio of di- and triblocks in the compound. This is especially problematic in the sequential approach, where the difference in molecular weight between the two components is very small (only 10% in the systems used in this study), and with the difunctional initiator. In the latter, the functionality of the initiator is hard to determine. The cleavage of the polyisoprene blocks with H_2O_2 in the presence of osmium tetroxide and the subsequent investigation of the remaining polystyrene blocks could be one possibility [132]. Also use of the SEC-IR coupling [186] with a highsensitive quantum cascade laser as the IR source might improve the results. The tracking of the polymerization reaction by in-situ spectroscopic methods may also help to understand the progression of the polymerization process and help to enhance the triblock copolymer content.

Bibliography

- [1] C. Goodyear, Improvement in India-Rubber Fabrics, US-patent 3633, **1844**.
- [2] J. L. White, *Int. Polym. Process.* **1996**, *11*, 4.
- [3] J. L. Leblanc, *Rubber Chem. Technol.* **2010**, *83*, 65–96.
- [4] J. L. Leblanc, J.-F. Pilard, E. Pianhanuruk, I. Campistron, J.-Y. Buzare, *J. Appl. Polym. Sci.* **2011**, *119*, 3058–3071.
- [5] ASTM D2000-12, Standard Classification System for Rubber Products in Automotive Applications, ASTM International, West Conshohocken, PA, **2012**.
- [6] F. Röthemeyer, F. Sommer, *Kautschuk-Technologie: Werkstoffe – Verarbeitung – Produkte*, 3rd ed., Carl Hanser Verlag, München, **2013**.
- [7] International Rubber Study Group (IRSG), http://www.rubberstudy.com/documents/WebSiteData_Aug2015.pdf (visited on 12/08/2015).
- [8] E. Abraham, B. M. Cherian, P. A. Elbi, L. A. Pothen, S. Thomas in *Recent Developments in Polymer Recycling*, (Eds.: A. Fainleib, O. Grigoryeva), Transworld Research Network, **2011**, Chapter 2. Recent advances in the recycling of rubber waste, pp. 47–100.
- [9] G. Kraus in *Advances in Polymer Science, Vol. 8*, (Eds.: H.-J. Cantow, G. Dall’Asta, J. D. Ferry, H. Fujita, W. Kern, G. Natta, S. Okamura, C. G. Overberger, W. Prins, G. V. Schulz, A. J. Staverman, J. K. Stille, H. A. Stuart), Springer, Berlin, **1971**, pp. 155–237.
- [10] J. L. Leblanc, *Filled Polymers - Science and Industrial Applications*, CRC Press, Boca Raton, FL, **2010**.
- [11] Y. Merkel, J. Diani, M. Brieu, P. Gilormini, J. Caillard, *J. Appl. Polym. Sci.* **2012**, *123*, 1153–1161.

-
- [12] J. L. Leblanc, M. Putman, E. Pianhanuruk, *J. Appl. Polym. Sci.* **2011**, *121*, 1096–1117.
- [13] J. L. White, *Rubber Chem. Technol.* **2009**, *82*, 131–148.
- [14] H. Ambacher, M. Strauß, H.-G. Kilian, S. Wolff, *KGK Kautsch. Gummi Kunstst.* **1991**, *44*, 1111–1118.
- [15] S. S. Sternstein, S. Amanuel, M. L. Shofner, *Rubber Chem. Technol.* **2010**, *83*, 181–198.
- [16] A. M. Randall, C. G. Robertson, *J. Appl. Polym. Sci.* **2014**, *131*, 40818 (1–10).
- [17] D. Berkemeier, A. Limper, M. Rimker, O. Klockmann, H. Keuter, R. H. Schuster, *Mixing of Rubber Compounds*, (Ed.: A. Limper), Carl Hanser Verlag, Munich, **2012**.
- [18] *Current Topics in Elastomers Research*, (Ed.: A. K. Bhowmick), CRC Press, Boca Raton, **2008**.
- [19] A. E. Atabani, I. A. Badruddin, S. Mekhilef, S. A. S., *Renewable Sustainable Energy Rev.* **2011**, *15*, 4586–4610.
- [20] C. R. Bradley, A. Delaval, *Tire Sci. Technol.* **2013**, *41*, 2–20.
- [21] R. Figuli, L. Schwab, J. Lacayo-Pineda, H. Deckmann, M. Wilhelm, *KGK Kautsch. Gummi Kunstst.* **2016**, *69*.
- [22] K. Hyun, M. Wilhelm, C. O. Klein, K. S. Cho, J. G. Nam, K. H. Ahn, S. J. Lee, R. H. Ewoldt, G. H. McKinley, *Prog. Polym. Sci.* **2011**, *36*, 1697–1753.
- [23] K. Reinheimer, M. Grosso, F. Hetzel, J. Kübel, M. Wilhelm, *J. Colloid Interf. Sci.* **2012**, *380*, 201–212.
- [24] D. Ahirwal, H. Palza, G. Schlatter, M. Wilhelm, *Korea-Aust. Rheol. J.* **2014**, *26*, 319–326.
- [25] M. Kempf, D. Ahirwal, M. Cziep, M. Wilhelm, *Macromolecules* **2013**, *46*, 4978–4994.
- [26] J. L. Leblanc, A. Mongruel, *Prog. Rubber Plast. Technol.* **2001**, *17*, 162–185.
- [27] J. L. Leblanc, *J. Appl. Polym. Sci.* **2003**, *89*, 1101–1115.
- [28] J. L. Leblanc, *J. Appl. Polym. Sci.* **2008**, *109*, 1271–1293.
- [29] J. L. Leblanc, *J. Appl. Polym. Sci.* **2012**, *126*, 408–422.
- [30] J. L. Leblanc, *J. Appl. Polym. Sci.* **2006**, *100*, 5102–5118.

- [31] G. Holden, E. T. Bishop, N. R. Legge, *J. Polym. Sci. Part C* **1966**, *26*, 37–57.
- [32] R. J. Spontak, N. P. Patel, *Curr. Opin. Colloid Interface Sci.* **2000**, *5*, 334–341.
- [33] H. A. Barnes, *A handbook of elementary rheology*, University of Wales, Institute of Non-Newtonian Fluid Mechanics, Aberystwyth, **2000**.
- [34] J. M. Dealy, R. G. Larson, *Structure and Rheology of Molten Polymers*, Hanser, Munich, **2006**.
- [35] C. W. Macosko, *Rheology: principles, measurements, and applications*, Wiley-VCH, New York, **1994**.
- [36] A. Y. Malkin, *Rheology Fundamentals*, ChemTec Publishing, Toronto, **1994**.
- [37] T. G. Mezger, *The Rheology Handbook*, 2nd Ed., Vincentz Network, **2006**.
- [38] D. Merger, M. Wilhelm, *Rheol. Acta* **2014**, *53*, 621–634.
- [39] M. H. Wagner, V. H. Rolon-Garrido, K. Hyun, M. Wilhelm, *J. Rheol.* **2011**, *55*, 495–516.
- [40] K. Hyun, S. H. Kim, K. H. Ahn, S. J. Lee, *J. Non-Newtonian Fluid Mech.* **2002**, *107*, 51–65.
- [41] G. Heinrich, M. Klueppel, *Filled elastomers drug delivery systems*, (Ed.: M. Arora), Springer, Berlin, **2002**, pp. 1–44.
- [42] M. Wilhelm, D. Maring, H. W. Spiess, *Rheol. Acta* **1998**, *37*, 399–405.
- [43] C. O. Klein, H. W. Spiess, A. Calin, C. Balan, M. Wilhelm, *Macromolecules* **2007**, *40*, 4250–4259.
- [44] K. S. Cho, K. Hyun, K. H. Ahn, S. J. Lee, *J. Rheol.* **2005**, *49*, 747–758.
- [45] R. H. Ewoldt, A. E. Hosoi, G. H. McKinley, *AIP Conf. Proc.* **2008**, *1027*, 1135.
- [46] M. Wilhelm, *Macromol. Mater. Eng.* **2002**, *287*, 83–105.
- [47] T. Doetsch, M. Pollard, M. Wilhelm, *J. Phys. Condens. Matter* **2003**, *15*, 923–931.
- [48] T. Neidhoefer, S. Sioula, N. Hadjichristidis, M. Wilhelm, *Macromol. Rapid Commun.* **2004**, *25*, 1921–1926.
- [49] D. van Dusschoten, M. Wilhelm, *Rheol. Acta* **2001**, *40*, 395–399.
- [50] C.-H. Bi, D. Li, L.-J. Wang, Y. Wang, B. Adhikari, *Carbohydr. Polym.* **2013**, *92*, 1151–1158.

-
- [51] M. Wilhelm, K. Reinheimer, J. Kübel, *Z. Phys. Chem.* **2012**, *226*, 547–567.
- [52] F. Renou, J. Stellbrink, G. Petekidis, *J. Rheol.* **2010**, *54*, 1219–1242.
- [53] K. Hyun, M. Wilhelm, *Macromolecules* **2009**, *42*, 411–422.
- [54] J. L. Leblanc, *Prog. Polym. Sci.* **2002**, *27*, 627–687.
- [55] J. Fröhlich, W. Niedermeier, H.-D. Luginsland, *Compos. Part A Appl. Sci. Manuf.* **2005**, *36*, 449–460.
- [56] *Carbon black*, 2nd rev. & exp. Ed., (Eds.: J.-B. Donnet, R. C. Bansal, M.-J. Wang), Marcel Dekker, New York, NY, **1993**.
- [57] A. Y. Watson, P. A. Valberg, *AIHA J.* **2001**, *62*, 218–228.
- [58] G. Collin, M. Zander, *Chem. Ing. Tech.* **1991**, *63*, 539.
- [59] I. Morozov, B. Lauke, G. Heinrich, *Comput. Mater. Sci.* **2010**, *47*, 817–825.
- [60] T. A. Witten, M. Rubinstein, R. H. Colby, *J. Phys. II* **1993**, *3*, 367–383.
- [61] ASTM D6556-14, Standard Test Method for Carbon Black — Total and External Surface Area by Nitrogen Adsorption, ASTM International, West Conshohocken, PA, **2010**.
- [62] ASTM D1510-13, Standard Test Method for Carbon Black — Iodine Adsorption Number, ASTM International, West Conshohocken, PA, **2013**.
- [63] ASTM D2414-14, Standard Test Method for Carbon Black – Oil Adsorption Number (OAN), ASTM International, West Conshohocken, PA, **2014**.
- [64] ASTM D3493-14, Standard Test Method for Carbon Black – Oil Adsorption Number of Compressed Sample (COAN), ASTM International, West Conshohocken, PA, **2014**.
- [65] ASTM D1765-14, Standard Classification System for Carbon Blacks Used in Rubber Products, ASTM International, West Conshohocken, PA, **2014**.
- [66] ASTM International, Glossary of Terms relating to Rubber and Rubber-like Materials, ASTM Special Technical Publication No. 184, **1956**.
- [67] A. Mostafa, A. Abouel-Kasem, M. R. Bayoumi, M. G. El-Sebaie, *J. Test. Eval.* **2010**, *38*, 347–359.

- [68] F. Saeed, A. Ansarifar, R. J. Ellis, Y. Haile-Meskel, M. S. Irfan, *J. Appl. Polym. Sci.* **2012**, *123*, 1518–1529.
- [69] C. Wortmann, F. Dettmer, F. Steiner, *Chem. Unserer Zeit* **2013**, *47*, 300–309.
- [70] E. Masnada, S. Merabia, M. Couty, J.-L. Barrat, *Soft Matter* **2013**, *9*, 10532–10544.
- [71] L. Karásek, B. Meissner, S. Asai, M. Sumita, *Polym. J.* **1996**, *28*, 121–126.
- [72] A. K. Kota, B. H. Cipriano, M. K. Duesterberg, A. L. Gershon, D. Powell, S. R. Raghavan, H. A. Bruck, *Macromolecules* **2007**, *40*, 7400–7406.
- [73] M. Sahimi, *Applications of Percolation Theory*, Taylor & Francis, London, **1994**.
- [74] M. Sumita, K. Sakata, S. Asai, K. Miyasaka, H. Nakagawa, *Polym. Bull.* **1991**, *25*, 265–271.
- [75] P. Pötschke, M. Abdel-Goad, S. Pegel, D. Jehnichen, J. E. Mark, D. Zhou, G. Heinrich, *J. Macromol. Sci. Part A: Pure Appl. Chem.* **2009**, *47*, 12–19.
- [76] F. Du, R. C. Scogna, W. Zhou, S. Brand, J. E. Fischer, K. I. Winey, *Macromolecules* **2004**, *37*, 9048–9055.
- [77] J. T. Baumann, *Fatigue, stress, and strain of rubber components: a guide for design engineers*, Carl Hanser Verlag, Munich, **2011**.
- [78] *Non-Linear Viscoelasticity of Rubber Composites and Nanocomposites*, (Eds.: D. Ponnamma, S. Thomas), Springer, **2014**.
- [79] E. Guth, O. Gold, *Phys. Rev.* **1938**, *53*, 322.
- [80] A. Y. Malkin, A. I. Isayev, *Rheology: Concepts, Methods and Applications*, ChemTec Publishing, Toronto, **2006**.
- [81] E. Guth, *J. Appl. Phys.* **1945**, *16*, 20–25.
- [82] L. Mullins, N. R. Tobin, *J. Appl. Polym. Sci.* **1965**, *9*, 2993–3009.
- [83] G. B. Ouyang, *KGK Kautsch. Gummi Kunstst.* **2006**, *59*, 332–343.
- [84] F. Sosson, L. Belec, J.-F. Chailan, P. Carriere, A. Crespy, *J. Appl. Polym. Sci.* **2010**, *117*, 2715–2723.
- [85] S. Merabia, P. Sotta, D. R. Long, *Macromolecules* **2008**, *41*, 8252–8266.

-
- [86] A. R. Payne, *J. Appl. Polym. Sci.* **1962**, *6*, 57–63.
- [87] A. R. Payne, R. E. Whittaker, *Rubber Chem. Technol.* **1971**, *44*, 440–478.
- [88] M. I. Aranguren, E. Mora, J. V. Degroot, C. W. Macosko, *J. Rheol.* **1992**, *36*, 1165–1182.
- [89] J. Diani, B. Fayolle, P. Gilormini, *Eur. Polym. J.* **2009**, *45*, 601–612.
- [90] L. Mullins, *Rubber Chem. Technol.* **1969**, *42*, 339–362.
- [91] S. Merabia, P. Sotta, D. R. Long, *J. Polym. Sci. Part B: Polym. Phys.* **2010**, *48*, 1495–1508.
- [92] A. Papon, S. Merabia, L. Guy, F. Lequeux, H. Montes, P. Sotta, D. R. Long, *Macromolecules* **2012**, *45*, 2891–2904.
- [93] C. M. Roland, *J. Rheol.* **1990**, *34*, 25–34.
- [94] J. L. Leblanc, *J. Appl. Polym. Sci.* **2006**, *101*, 3638–3651.
- [95] J. L. Leblanc, *J. Appl. Polym. Sci.* **2005**, *95*, 90–106.
- [96] J. L. Leblanc, *Rheol. Acta* **2006**, *46*, 1013–1027.
- [97] J. L. Leblanc, G. Nijman, *J. Appl. Polym. Sci.* **2009**, *112*, 1128–1141.
- [98] M. Myhre, S. Saiwari, W. Dierkes, J. Noordermeer, *Rubber Chem. Technol.* **2012**, *85*, 408–449.
- [99] K. E. Kear, *Developments in Thermoplastic Elastomers*, Rapra Technology, Shropshire, UK, **2003**.
- [100] Y. Chen, C. Xu, Y. Cao, X. Cao, *Polym. Test.* **2012**, *31*, 728–736.
- [101] J. Oderkerk, G. Groenickx, *Polymer* **2002**, *43*, 2219–2228.
- [102] J. L. Adams, W. M. Graessley, R. A. Register, *Macromolecules* **1994**, *27*, 6026–6032.
- [103] F. S. Bates, G. H. Fredrickson, *Annu. Rev. Phys. Chem.* **1990**, *41*, 525–557.
- [104] N. Hadjichristidis, S. Pispas, G. Floudas, *Block Copolymers*, Wiley Interscience, **2003**.
- [105] V. Abetz, P. F. Simon in *Advances in Polymer Science, Vol. 189*, (Ed.: V. Abetz), Springer–Verlag, Berlin, **2005**, pp. 125–212.
- [106] G. H. Fredrickson, F. S. Bates, *Annu. Rev. Mater. Sci.* **1996**, *26*, 501–550.

- [107] J. He, K. Knoll, G. McKee, *Macromolecules* **2004**, *37*, 4399–4405.
- [108] M. W. Matsen, F. S. Bates, *Macromolecules* **1996**, *29*, 1091–1098.
- [109] B. Debbaut, H. Burhin, *J. Rheol.* **2002**, *46*, 1155–1176.
- [110] J. L. White, M. H. Han, N. Nakajima, R. Brzoskowski, *J. Rheol.* **1991**, *35*, 167–189.
- [111] S. Montes, J. L. White, N. Nakajima, F. C. Weissert, K. Min, *Rubber Chem. Technol.* **1988**, *61*, 698–716.
- [112] Y. Chen, C. Xu, X. Cao, *Polym. Compos.* **2015**, *36*, 623–629.
- [113] J. S. Dick, H. A. Pawlowski, *J. Elas. Plas.* **1995**, *27*, 11–38.
- [114] L. Hilliou, D. van Dusschoten, M. Wilhelm, H. Burhin, E. R. Rodger, *Rubber Chem. Technol.* **2004**, *77*, 192–200.
- [115] T. Neidhoefer, PhD thesis, Johannes Gutenberg-University of Mainz, Mainz, **2003**.
- [116] Scarabaeus GmbH, <http://www.scarabaeus-gmbh.de/produkte/rheometer/sis-v-reihe/> (visited on 12/30/2015).
- [117] TA Instruments, <http://www.tainstruments.com/pdf/brochure/BROCH-ARESG2-2014-EN.pdf> (visited on 12/30/2015).
- [118] Alpha Technologies, <http://www.alpha-technologies.com/rpa2000-rubber-process-analyzer.aspx> (visited on 12/30/2015).
- [119] M. Abbasi, N. R. Ebrahimi, M. Wilhelm, *J. Rheol.* **2013**, *57*, 1693–1714.
- [120] B. Jurkowski, B. an Jurkowska, *J. Macromol. Sci. Part B: Phys.* **1998**, *37*, 135–142.
- [121] L. Schwab, Master thesis, Karlsruher Institut für Technologie, Karlsruhe, Germany, **2011**.
- [122] C. D. Han, D. M. Baek, J. K. Kim, *Polymer* **1992**, *33*, 294–305.
- [123] D.-J. Kim, H.-J. Kim, G. H. Yoon, *Int. J. Adhes. Adhes.* **2005**, *25*, 288–295.
- [124] D. H. Haddleton, A. V. G. Muir, S. N. Richards in *Macromolecular Design of Polymeric Materials*, (Eds.: K. Hatada, T. Kitayama, O. Vogl), Marcel Dekker, New York, **1997**, Chapter 8.
- [125] T. Hashimoto, Y. Ijichi, L. J. Fetters, *J. Chem. Phys.* **1988**, *89*, 2463–2472.

-
- [126] M. Szwarc, *Nature* **1956**, *178*, 1168–1169.
- [127] P. Guyot, J. C. Favier, H. Uytterhoeven, M. Fontanille, P. Sigwalt, *Polymer* **1981**, *22*, 1724–1728.
- [128] *Anionic Polymerization*, (Eds.: N. Hadjichristidis, A. Hirao), Springer Japan, Tokyo, **2015**.
- [129] G. Odian, *Principles of polymerization*, 4th, Wiley Interscience, **2004**.
- [130] M. Morton, *Anionic polymerization: principles and practice*, Academic Press Inc., New York, **1983**.
- [131] C. Elschenbroich, *Organometallics*, 6., Teubner Verlag, Wiesbaden, **2008**.
- [132] Y. S. Yu, R. Jérôme, R. Fayt, P. Teyssié, *Macromolecules* **1994**, *27*, 5957–5963.
- [133] Z. Lu, H. Xu, Y. Li, Y. Hu, *J. Appl. Polym. Sci.* **2006**, *100*, 1395–1402.
- [134] T. Nugay, S. Kucukyavuz, *Polym. Int.* **1992**, *29*, 195–199.
- [135] L. J. Fetters, M. Morton, *Macromolecules* **1969**, *2*, 453–458.
- [136] R. Matmour, A. S. More, p. P. Wadgaonkar, Y. Gnanou, *J. Am. Chem. Soc.* **2006**, *128*, 8158–8159.
- [137] G. Beinert, P. Lutz, E. Franta, P. Rempp, *Makromol. Chem.* **1978**, *179*, 551–555.
- [138] L. H. Tung, G. Y.-S. Lo, *Macromolecules* **1994**, *27*, 1680–1684.
- [139] Y. S. Yu, P. Dubois, R. Jérôme, P. Teyssié, *Macromolecules* **1996**, *29*, 1753–1761.
- [140] Y. S. Yu, P. Dubois, P. Teyssié, R. Jérôme, *Macromolecules* **1997**, *30*, 7356–7362.
- [141] M. Hillmyer, *Curr. Opin. Solid State Mater. Sci.* **1999**, *4*, 559–564.
- [142] A. L. Gatzke, *J. Polym. Sci. Part A: Polym. Chem.* **1969**, *7*, 2281–2292.
- [143] *Polymer Data Handbook*, (Ed.: J. E. Mark), Oxford University Press, Oxford, UK, **1999**.
- [144] I. W. Hamley, *The Physics of Block Copolymers*, Oxford University Press, **1998**.
- [145] N. Stribeck, *X-Ray Scattering of Soft Matter*, Springer, **2007**.
- [146] N. Kasai, M. Kakudo, *X-Ray Diffraction by Macromolecules*, Springer, **2005**.
- [147] *Small Angle X-ray Scattering*, (Eds.: O. Glatter, O. Kratky), Academic Press Inc., New York, NY, **1982**.

- [148] I. W. Hamley, V. Castelletto, *Prog. Polym. Sci.* **2004**, *29*, 909–948.
- [149] R. J. Angelo, R. M. Ikeda, M. L. Wallach, *Polymer* **1965**, *6*, 141–156.
- [150] Y. Zhang, U. Wiesner, *Macromol. Chem. Phys.* **1998**, *199*, 1771–1784.
- [151] I. Alig, G. Floudas, A. Avgeropoulos, N. Hadjichristidis, *Macromolecules* **1997**, *30*, 5004–5011.
- [152] C. D. Han, D. M. Baek, J. K. Kim, *Macromolecules* **1990**, *23*, 561–570.
- [153] T. Dollase, R. Graf, A. Heuer, H. W. Spiess, *Macromolecules* **2001**, *34*, 298–309.
- [154] R. Prabhu, R. Klitkou, G. A. Medvedev, J. M. Caruthers, *J. Polym. Sci. Part B: Polym. Phys.* **2013**, *51*, 687–697.
- [155] T. Meins, N. Dingenouts, J. Kübel, M. Wilhelm, *Macromolecules* **2012**, *45*, 7206–7219.
- [156] T. Schweizer, *Rheol. Acta* **2002**, *41*, 337–344.
- [157] L. Schwab, N. Hojdis, L. Lacayo-Pineda, M. Wilhelm, *Macromol. Mater. Eng.* **accepted**, DOI 10.1002/mame.201500356.
- [158] S. Höfl, F. Kremer, H. W. Spiess, M. Wilhelm, S. Kahle, *Polymer* **2006**, *47*, 7282–7288.
- [159] I. Balberg, *Carbon* **2002**, *40*, 139–143.
- [160] K. Hilarius, D. Lellinger, I. Alig, T. Villmov, S. Pegel, P. Pötschke, *Polymer* **2013**, *54*, 5865–5874.
- [161] Institut für Arbeitsschutz der Deutschen Gesetzlichen Unfallversicherung, GESTIS–Stoffdatenbank, www.dguv.de/ifa/stoffdatenbank (visited on 01/04/2016).
- [162] ASTM D6204-12, Standard Test Method for Rubber – Measurement of Unvulcanized Rheological Properties Using Rotorless Shear Rheometers, ASTM International, West Conshohocken, PA, **2012**.
- [163] J. Léopoldès, C. Barrès, J. L. Leblanc, P. Georget, *J. Appl. Polym. Sci.* **2004**, *91*, 577–588.
- [164] I. M. Krieger, T. J. Dougherty, *Trans. Soc. Rheol.* **1959**, *3*, 137–152.
- [165] Z. Soua, O. Larue, E. Vorobiev, J.-L. Lanoisellé, *Colloids Surf. A: Physicochem. Eng. Aspects* **2006**, *274*, 1–10.

-
- [166] A. Kasgoz, D. Akin, A. I. Ayten, A. Durmus, *Compos. Part B Eng.* **2014**, *66*, 126–135.
- [167] S. Ata, K. Kobashi, M. Yumura, K. Hata, *Nano Lett.* **2012**, *12*, 2710–2716.
- [168] K. Akutagawa, K. Yamaguchi, A. Yamamoto, H. Hesguri, *Rubber Chem. Technol.* **2008**, *81*, 182–189.
- [169] G. C. Vebber, C. N. Pereira, *J. Appl. Polym. Sci.* **2015**, *132*, 41929.
- [170] A. N. Gent, *J. Polym. Sci. Part C: Symposium* **1974**, *48*, 1–17.
- [171] J. L. Leblanc, *J. Appl. Polym. Sci.* **2006**, *101*, 1140–1150.
- [172] Z. H. Li, J. Zhang, S. J. Chen, *eXPRESS Polym. Lett.* **2008**, *2*, 695–704.
- [173] F. Stadlbauer, T. Koch, F. Planitzer, W. Fidi, V.-M. Archodoulaki, *Polymer Testing* **2013**, *32*, 1045–1051.
- [174] S. M. Cadwell, R. A. Merrill, C. M. Sloman, F. L. Yost, *Ind. Eng. Chem.* **1940**, *12*, 19–23.
- [175] Y.-L. Lee, M. E. Barkey, H. Kang, *Metal Fatigue Analysis Handbook*, Butterworth-Heinemann, Oxford, UK, **2012**.
- [176] W. V. Mars, A. Fatemi, *Int. J. Fatigue* **2002**, *24*, 949–961.
- [177] J.-B. Le Cam, B. Huneau, E. Verron, *Fatigue Fract. Engng. Mater. Struct.* **2008**, *31*, 1031–1038.
- [178] W.-B. Shangguan, X.-L. Wang, J.-X. Deng, S. Rakheja, X.-Y. Pan, B. Yu, *Mater. Des.* **2014**, *58*, 65–73.
- [179] F. Stadlbauer, T. Koch, V.-M. Archodoulaki, F. Planitzer, W. Fidi, A. Holzner, *Materials* **2013**, *6*, 5502–5516.
- [180] X.-L. Wang, W.-B. Shengguan, S. Rakheja, W.-C. Li, B. Yu, *Fatigue Fract. Eng. Mater. Struct.* **2014**, *37*, 50–61.
- [181] W. V. Mars, A. Fatemi, *Rubber Chem. Technol.* **2003**, *76*, 1241–1258.
- [182] J.-B. Le Cam, B. Huneau, E. Verron, *Int. J. Fatigue* **2013**, *52*, 82–94.
- [183] F. Abraham, T. Alsuth, S. Jerrams, *Mater. Des.* **2005**, *26*, 239–245.

- [184] H. Zhang, A. K. Scholz, J. de Crevoisier, D. Berghezan, T. Narayanan, E. J. Kramer, C. Creton, *J. Polym. Sci. Part B: Polym. Phys.* **2015**, *53*, 422–429.
- [185] R. Kádár, M. Wilhelm, I. Vittorias, A. Mulone in *The 15th International Conference on Deformation, Yield and Fracture of Polymers - Book of Abstracts*, **2014**, pp. 431–434.
- [186] T. F. Beskers, T. Hofe, M. Wilhelm, *Polym. Chem.* **2015**, *6*, 128–142.
- [187] LyondellBasell, Technical data sheet Lupolen 3721 C, **2015**.

Appendix

A. Experimental part

A.1. Anionic polymerization

Anionic polymerization is very sensitive to impurities in the reaction system. Even small traces of oxygen, argon or chemicals with acidic protons have to be avoided as they are able to terminate the reaction.

A.1.1. Reactants and solvents

Styrene (Acros, 99%) was degassed by at least three consecutive freeze-thaw cycles. Afterwards it was stirred for at least 8 h over calcium hydride (CaH_2 , Acros, 93%). Then it was distilled into an evacuated flask with dibutylmagnesium (Aldrich, 1 M in hexane), in which the solvent was evaporated prior to the distillation of styrene. The styrene was stirred for at least 8 h at room temperature, before it was distilled into an empty flask.

Isoprene (Acros, 98%) was stirred over dried *n*-butyl lithium (Aldrich, 2.5 M in hexane) for 30 min, then distilled under reduced pressure into a second flask with dried *n*-butyl lithium and stirred for 30 min. During the stirring, the flask was cooled with an ice bath to prevent the polymerization of isoprene. Finally the isoprene was distilled into an empty flask.

Tetrahydrofuran (THF, Carl Roth 99.5%) was boiled under reflux with CaH_2 for several days. After distillation it was boiled under reflux with sodium and benzophenone until the mixture turned purple. The THF was distilled and stored in a flask with sodium and benzophenone, which was directly connected to the vacuum line.

Toluene (Carl Roth, 99.5%) was boiled under reflux with CaH_2 for several days. After distillation it was stored in a flask with either living polystyrene anions or a mixture of *n*-butyl lithium and diphenylethylene, which was directly connected to the vacuum line.

Cyclohexane (Carl Roth, 99.5 %) was directly given into a flask with *n*-butyl lithium and diphenylethylene, which was connected to the vacuum line.

Dichlorodimethylsilane (Acros, 99 %) was stirred over CaH₂ for at least one day at room temperature and then distilled into an empty flask and dissolved in toluene.

1,2-Bis(chlorodimethylsilyl)ethane (VWR, 90 %) was stirred twice over CaH₂ for 1 h at elevated temperatures (50 °C to 70 °C) and, after distillation into an empty flask, THF was added.

1,5-Dibromopentane (VWR) was washed with concentrated HCl, NaHCO₃-solution and distilled water. Then it was dried over CaCl₂ (20 h) and P₄O₁₀ (3 h). Eventually it was distilled in a flask with 3 Å molecular sieve and dissolved in THF.

Diacetyl benzene (Acros) was stirred over CaH₂ for 6 h at room temperature and then distilled into an empty flask and dissolved in THF.

1,3-Diisopropenyl benzene (Aldrich, 97 %) was stirred over dibutylmagnesium for 6 h, then distilled in an empty flask and dissolved in toluene.

Sec-butyl lithium (Aldrich, 1.4 M in cyclohexane) and methanol (Carl Roth, 99 %) was used as received.

A.1.2. Synthesis of poly(styrene-*b*-isoprene-*b*-styrene) triblock copolymers

For the anionic polymerization high-vacuum techniques and Argon s inert gas were used to prevent termination reactions caused by impurities. All glassware was heated using a heat-gun with 600 °C under vacuum and after cooling the glassware was flooded with Argon. This was repeated thrice. The reaction flask was connected to the vacuum line by glass joints. All glassware was equipped with PTFE stopcocks. The solvent (either toluene or cyclohexane) was directly distilled into the reaction flask from the containers. Then either the first monomer was added with a syringe followed by the addition of the *sec*-butyl lithium (also with a syringe) or the other way round. For the difunctional initiator, diisopropenyl benzene and *sec*-butyl lithium were added to the pure solvent and stirred for a while, sometimes at slightly elevated temperatures (up to 60 °C), before the first monomer was added. After the complete reaction of the first monomer (at least 2 h for styrene and overnight for isoprene), a sample of the reaction solution was taken with a syringe under Argon counter flow and pured into methanol degassed by at least three freeze-thaw cycles. The second monomer was

then added to the reaction solution with a syringe. After its complete reaction another sample was taken like before. For the coupling of the dianions a solution of the coupling agent in THF or toluene was added with a syringe. For the sequential method, the monomer of the third block (styrene) was added with a syringe. For all methods the reaction was terminated by the addition of a small amount of degassed methanol. Then the polymer was precipitated in methanol.

All polymers with isoprene blocks were dissolved in THF and di-*tert*-butyl phenol (Acros, 98 %) was added as a stabilizer (approximately 0.1 wt%) to prevent aging of the samples. The solvent was then removed under reduced pressure at $T \leq 70$ °C.

A.2. Instrumentation

¹H-NMR spectroscopy

For the ¹H-NMR spectroscopy a Bruker DRX 500 and a Bruker Avance III Microbay 400 MHz were used. If not further specified deuterated chloroform (Deutero, 99.8 %) was used as a solvent. Spectra were obtained at 500 MHz on the DRX 500 or at 400 MHz on the Avance III. Typically 256 or 512 scans were used.

Size exclusion chromatography

For the size exclusion chromatography (SEC) an instrument consisting of an Agilent 1100 pump, two SDV Lux 8 · 300 mm columns (10^3 Å and 10^5 Å) and a 8 · 15 mm column was used. It was equipped with an Agilent 1200 differential refractive index (DRI) and UV Detector ($\lambda = 254$ nm), a WGE Dr. Bures ETA-2010 viscometer and a PSS SLD 7000 MALLS detector. For this study only the DRI and the UV detector were used. THF (Scharlau, GPC-grade) was used as a solvent and the measurements were performed at 35 °C at a flow rate of 1 mL min⁻¹.

Dielectric measurements

The AC-conductivity of the samples was measured at 60 °C with an Alpha Single Unit Analyzer (Novocontrol Technologies, Montabaur, Germany) connected to a home-made dielectric geometry (diameter of 13 mm) built into an ARES LS rheometer (TA Instruments) over a frequency range from 10⁻² Hz to 10⁶ Hz.[158] The DC-conductivity $|\sigma_{DC}|$ was approximated by $|\sigma_0|$, i.e. the mean

value of AC-conductivity measurements between 10^{-1} Hz and 10^{-2} Hz. For all samples a specimen was measured three times.

Rheological measurements

For the rheological measurements three different instruments were used.

For most of the samples a SIS V50 rubber rheometer with closed and pressurized geometry with a cone-cone shape and grooved surfaces from Scarabaeus GmbH, Wetzlar (Germany) (now part of TA Instruments, New Castle, DE, USA) was used.

An ARES G2 rotational rheometer from TA Instruments was used as well. Different geometries were used, mostly plate-plate and cone-plate ($\alpha = 0.1$ rad) geometries with a diameter of 13 mm made from Invar were used. Also a plate-partitioned plate geometry (LAOS-geometry) with a plate geometry (diameter of 13 mm, Invar) mounted to the lower fixture (motor) and a plate geometry (diameter 8 mm or 10 mm, stainless steel) was mounted to the upper fixture (torque transducer). For the torsion experiments a torsion rectangular fixture was used. For the temperature control a forced convective oven was used.

Additionally, measurements on the RPA 2000 rubber rheometer (Alpha Technologies, Akron, Ohio) with closed and pressurized geometry with a cone-cone shape and grooved surfaces was used by Prof. J. L. Leblanc [12] from the university Pierre et Marie Curie in Paris, France.

The technical data of the three shear rheometers is given in Table 3.2.

For the tension measurements a GABO Eplexor 150N from Gabo Qualimeter Testanlagen GmbH, Ahlden, Germany, now part of Netzsch-Gerätebau GmbH, Selb, Germany was used. Depending on the measurement conditions a torque transducer with a maximum torque of either 25 N, 150 N or 1500 N was used. For the FT-Analysis, the raw data of the force and the deformation sensor were captured on an external ADC card with a LabVIEW routine.

Small angle X-ray scattering

For small angle X-ray scattering measurements, a S3-Micro instrument from Hecus X-ray systems, Graz Austria equipped with a point microfocus source and a 2D CCD-detector from Photonic Science, was used.

Dynamic scanning calorimetry

For the investigation of the glass transition temperatures of the polymers with dynamic scanning calorimetry, a DSC30 from Mettler-Toledo (Beaumont Leys, UK) was used. For the SIS triblock copolymers, a heating rate of 10 K min^{-1} was applied. The temperature was increased from room temperature to $150 \text{ }^\circ\text{C}$, then decreased to $-150 \text{ }^\circ\text{C}$ and then increased to $150 \text{ }^\circ\text{C}$. Only the result for the second heating run are interpreted. For the CB filled S-SBR a heating rate of 20 K min^{-1} was used. The temperature was increased from $-100 \text{ }^\circ\text{C}$ to $200 \text{ }^\circ\text{C}$, then decreased to $-100 \text{ }^\circ\text{C}$ and then increased to $200 \text{ }^\circ\text{C}$.

B. Samples and analytical results

B.1. Commercial thermoplastic polymers

For the investigation on the capabilities of the rubber rheometer for FT-Rheology, several commercial polymers were used: PS-1, PE-1, SIS-I and S-SBR. The samples SIS-I and S-SBR were used also for further investigations and their properties are listed in Appendix B.2 and Appendix B.3.

PS-1 is a linear polystyrene homopolymer from BASF, Ludwigshafen, Germany. It was synthesized by anionic polymerization and therefore has a narrow polydispersity ($PDI = 1.34$). The weight averaged molecular weight is $M_w = 292 \text{ kg mol}^{-1}$ (Fig. B.1).

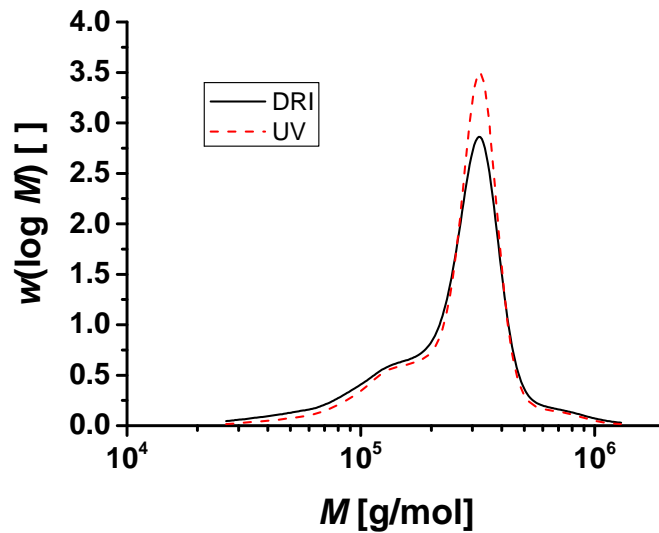


Figure B.1.: Molecular weight distribution of the linear polystyrene PS-1 (solvent: THF), the molecular weight is $M_w = 292 \text{ kg mol}^{-1}$ and $PDI = 1.34$.

PE-1 is a polyethylene copolymerized with hexene, sold under the trade name Lupolen[®] 3721 C by LyondellBasell. The polymer has a density of $\rho = 0.937 \text{ g cm}^{-3}$, a melting point of 127°C and contains antioxidants [187].

B.2. Thermoplastic elastomers

In Chapter 4, the anionic synthesis of poly(styrene-*b*-isoprene-*b*-styrene) (SIS) block copolymers was described. In Chapter 5, two of these polymers, SIS-S2 and SIS-S3, were further characterized by rheology, together with an industrial SIS sample, SIS-I. In the following the analytic data of the different polymers mentioned in this study is given.

The molecular weight distribution was measured by size exclusion chromatography. For the polystyrene homopolymers, a calibration based on narrow PS standards, for the di- and triblock copolymers, a calibration based on PI standards was used. For all samples, the signal of the DRI detector was evaluated.

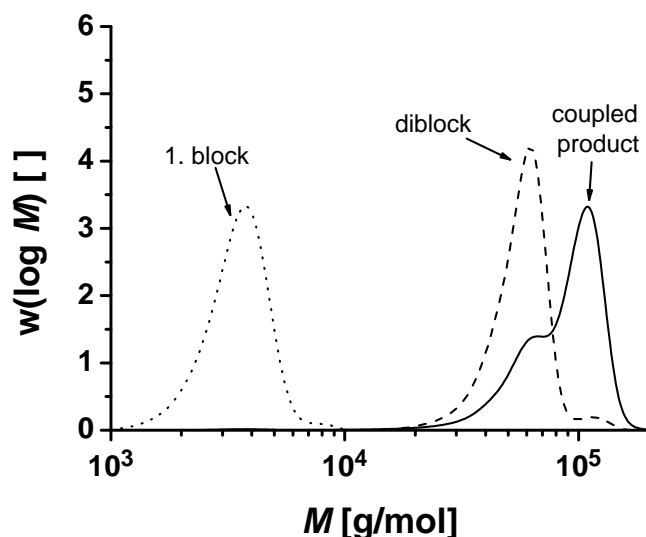


Figure B.2.: Molecular weight distribution of the samples taken from SIS-C3, which was synthesized by the coupling of two diblock anions with 1,2-bis(chlorodimethylsilyl)ethane, after each step. After the first step (dotted line) a single low molecular weight peak indicates the formation of a polystyrene with $M_w = 3.6 \text{ kg mol}^{-1}$ and a PDI of 1.10. The peak is shifted to higher molecular weights ($M_w = 58.5 \text{ kg mol}^{-1}$, PDI = 1.09) after the diblock is formed (dashed line). Due to oxygen contaminations during the sample withdrawal, another small peak at twice this molecular weight is detected. In the final product (full line) the peak with double the molecular weight of the diblock ($M_w = 107 \text{ kg mol}^{-1}$) is pronounced, but the coupling reaction was not quantitative as can be seen by the remaining diblock peak. The integral ratio of triblock in the product is 65% (solvent: THF).

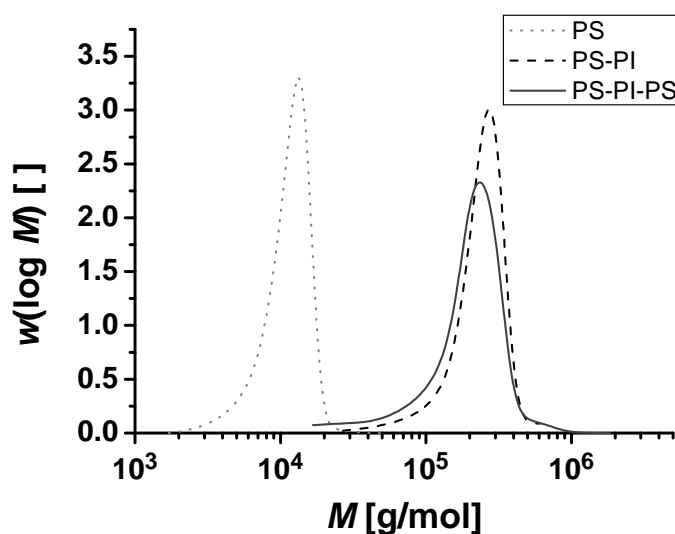


Figure B.3.: Molecular weight distribution of the samples taken from SIS-S1, which was synthesized by the sequential addition of styrene, isoprene and styrene. After the first step (PS homopolymer, dotted line) a single low molecular weight peak indicates the formation of a polystyrene with $M_w = 11.7 \text{ kg mol}^{-1}$ and a PDI of 1.16. The peak is shifted to higher molecular weights ($M_w = 246 \text{ kg mol}^{-1}$, PDI = 1.22) after the diblock is formed (dashed line). Due to oxygen contaminations during the sample withdrawal, another small peak at twice this molecular weight is detected. In the final product (full line) the peak is a little bit lower ($M_w = 221 \text{ kg mol}^{-1}$), due to the increase of the PDI (1.49). Thus the addition of the third block did not work (solvent: THF).

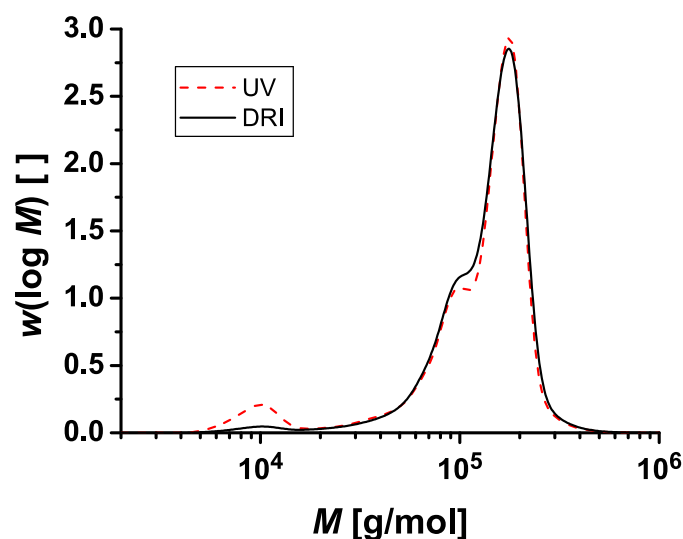


Figure B.4.: Molecular weight distribution of the industrial SIS sample SIS-I. The polymer has weight averaged molecular weight of $M_w = 147 \text{ kg mol}^{-1}$ and a of PDI = 1.44 (solvent: THF).

The composition of the different poly(styrene-*b*-isoprene) (SI) and poly(styrene-*b*-isoprene-*b*-styrene) (SIS) block copolymers was investigated by $^1\text{H-NMR}$ spectroscopy. Polyisoprene (PI) has four different possible isomers (Fig. B.5): 1,4-*cis*-, 1,4-*trans*-, 1,2- and 3,4-PI.

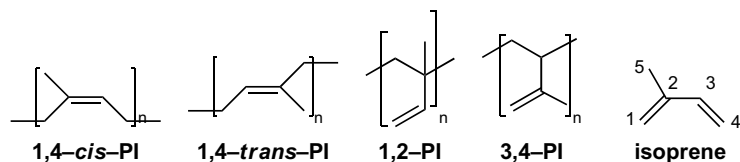


Figure B.5.: Possible isomers of polyisoprene and the monomer isoprene.

The mole fraction of each isomer and styrene in the final products were calculated from the following characteristic peaks (Table B.1).

Table B.1.: Composition of the different SI and SIS polymers used in this study for the rheological measurements as determined by $^1\text{H-NMR}$ spectroscopy (400 MHz, solvent = CDCl_3 , 512 scans).

| Sample | | synthetic method | styrene | | 1,4-PI | 3,4-PI |
|--------|-----------------------|------------------|---------|--------|--------|--------|
| | | | [mol%] | [vol%] | [mol%] | [mol%] |
| SIS-I | triblock ^a | industrial | 10.6 | 17.4 | 83.0 | 6.3 |
| SIS-S2 | diblock ^b | sequential | 4.3 | 7.3 | 89.7 | 5.9 |
| SIS-S2 | triblock ^c | sequential | 9.3 | 16.0 | 83.3 | 7.4 |
| SIS-S3 | diblock ^b | sequential | 7.4 | 12.4 | 87.4 | 5.1 |
| SIS-S3 | triblock ^c | sequential | 12.6 | 20.3 | 82.4 | 5.0 |

^a industrial SIS, Kraton D1161PT from Kraton Polymers Belgium sprl

^b PS-PI diblock before second styrene addition

^c final SIS triblock

For styrene, the peak of the aromatic protons in ortho position (integral value was always fixed to 2, $\delta = 6.9$ ppm to 6.2 ppm), for 1,4-PI, the peak of the vinyl proton ($\delta = 5.2$ ppm) and for 3,4-PI, the peak of the two vinyl protons ($\delta = 4.7$ ppm) was used. For the 1,2-PI, a characteristic peak is expected at $\delta = 5.7$ ppm for the vinyl protons. This peak was not present in any of the samples investigated, which is typical for PI synthesized by anionic polymerization in apolar solvents. The determination of the 1,4-*cis*-PI to 1,4-*trans*-PI ration is hard to calculate, because both isomers have their characteristic peaks (of the $-\text{CH}_3$ protons) at similar chemical shifts ($\delta = 1.6$ ppm and 1.5 ppm)

and hence overlap. Additional peaks of the PS and the 3,4-PI are also found in this region. Therefore the ratio between the 1,4-*cis*-PI to 1,4-*trans*-PI was not calculated.

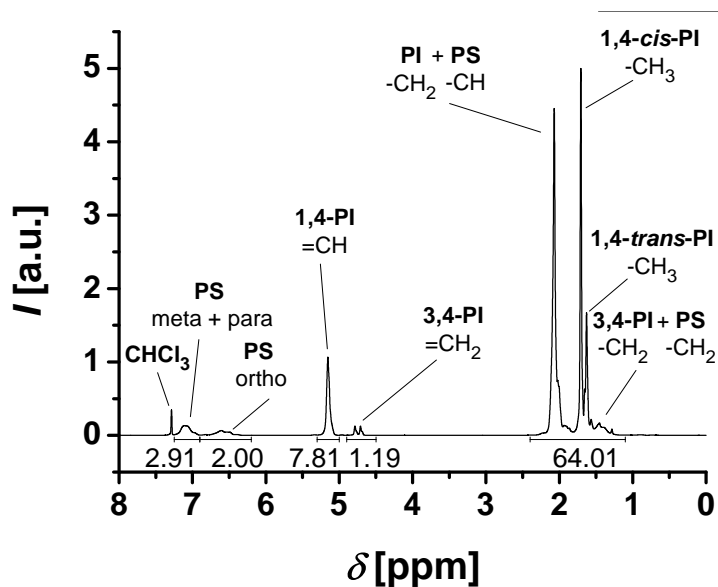


Figure B.6.: ^1H -NMR spectra of the industrial SIS-I (Kraton) (in deuterated chloroform at 400 MHz, 512 scans).

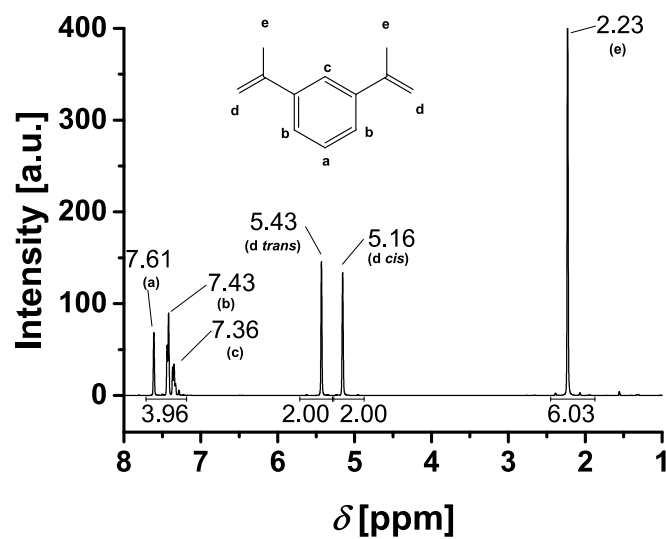


Figure B.7.: ^1H -NMR of diisopropenyl benzene **9** (in deuterated chloroform, 400 MHz, 1024 scans).

The phase morphology of the three samples used for the rheological characterization was investigated by small angle X-ray scattering. The results for sample SIS-S2 and SIS-S3 are given in Figs. B.8 and B.9, for SIS-I in Fig. 5.1.

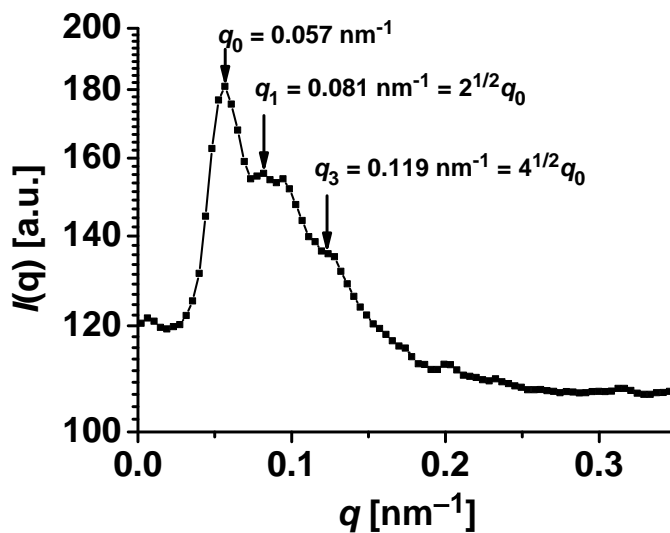


Figure B.8.: SAXS pattern of the synthesized sample SIS-S3 (measurement time: 10 s, no shearing).

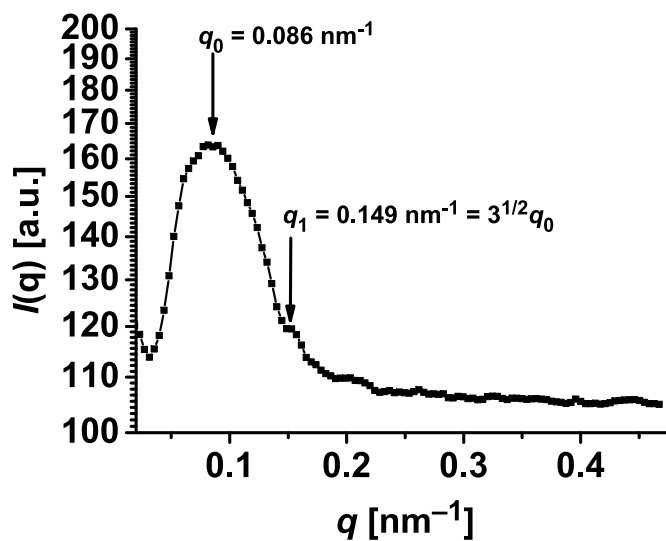


Figure B.9.: SAXS pattern of the synthesized sample SIS-S3 (measurement time: 10 s, no shearing).

B.3. Unvulcanized, carbon black filled S-SBR

The samples of this series were all prepared by Continental Reifen Deutschland. The matrix material is a solution polymerized styrene butadiene rubber (Nipol NS210, Zeon) with a molecular weight $M_w = 398 \text{ kg mol}^{-1}$ (Fig. B.10, PS calibration, DRI detector), a PDI of 1.83, 54.3 mol% 1,4 PB, 29.9 mol% 1,2 PB and 15.8 mol% ($\hat{=}$ 29.3 vol%) PS (Fig. B.11, $\rho_{1,2-PB} = 0.90 \text{ g cm}^{-3}$, $\rho_{1,4-PB} = 0.92 \text{ g cm}^{-3}$, $\rho_{PS} = 1.05 \text{ g cm}^{-3}$ [143]). The structural properties of the CB used are given in Table 6.1. Additionally, transmission electron microscope images of the different particles are shown in Fig. 6.1.

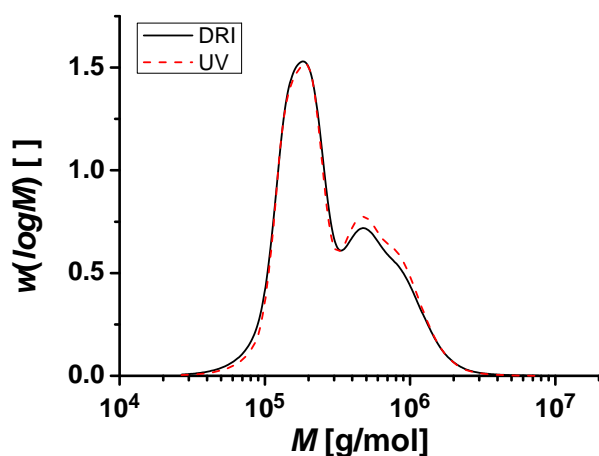


Figure B.10.: Molecular weight distribution of pure S-SBR calculated with a PS calibration for both UV- and DRI-detector (Solvent: THF).

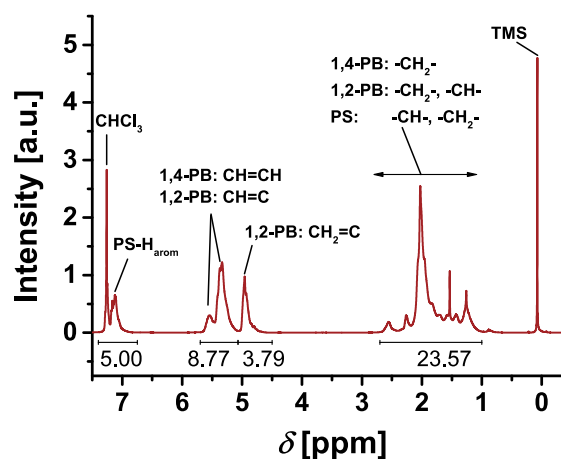


Figure B.11.: ^1H -NMR spectra of pure S-SBR (in deuterated chloroform at 400 MHz, 512 scans).

B.4. Vulcanized, carbon black filled S-SBR for fatigue measurements

The samples for the measurements of vulcanized rubber in tension and torsion (Chapter 7) were made by Continental Reifen Deutschland. The samples were received already vulcanized in form of rectangular specimen with approximately the following dimensions: 50 mm · 10 mm · 2 mm.

The samples were divided in four different series. In the first series (13 samples) the amount of CB was varied between 0 phr to 60 phr of the N339 grade. These samples correspond to those used unvulcanized in shear rheology (Appendix B.3). In the second series (5 samples), the amount of the vulcanization accelerator DCBS (= *N,N*-dicyclohexyl-2-benzothiazole sulfenamide) was varied

between 0.75 phr to 1.75 phr. For the third series (9 samples) the matrix polymer composition was varied from 100 phr natural rubber (NR) down to 70 phr NR and different amounts of butadiene rubber (BR) and styrene butadiene rubber (SBR). Finally, in the fourth series (5 samples) different anti-aging additives were included.

B.5. Unvulcanized, carbon black filled E-SBR

These samples were used in the comparison of the V50 rubber rheometer with the RPA 2000. They were prepared by Prof. Leblanc (Paris) and used in a previous publication [12]. The chemical structure of some of the additives is given in Fig. B.12.

Table B.2.: Detailed recipe of the samples with emulsion SBR from Leblanc et al. [12]. The samples were prepared by Prof. Leblanc (Paris).

| Ingredient [†] | function | density [g/cm ³] | amount [phr] [#] |
|-------------------------|----------------|---------------------------------|------------------------------|
| SBR | rubber matrix | 0.93 | 100.0 |
| Napthenic oil | processing oil | 0.98 | 5.0 |
| Zinc oxide | activator | 5.57 | 5.0 |
| Stearic acid | activator | 0.92 | 3.0 |
| TMQ | stabilizer | 1.08 | 2.0 |
| IPPD | stabilizer | 1.17 | 1.0 |
| Carbon black | filler | 1.86 | 0–50.0 |

[†] SBR: styrene butadiene rubber, emulsion polymerized

TMQ: 2,2,4-Trimethyl-1,2-dihydroquinoline

IPPD: *N*-Isopropyl-*N'*-phenyl-*p*-phenylenediamine

[#] parts per hundred parts of rubber by weight

The matrix polymer is an emulsion polymerized styrene-butadiene rubber (E-SBR) with a molecular weight (weight averaged) of 750.4 kg mol⁻¹ and a PDI of 6.5 (Fig. B.13). The high polydispersity is due to the radical polymerization used.

The chemical composition of the E-SBR was determined by ¹H-NMR spectroscopy (Fig. B.14).

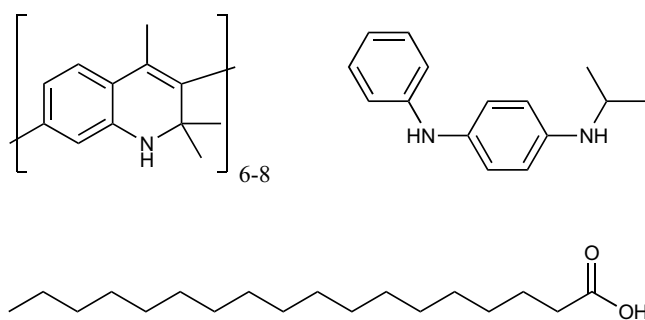


Figure B.12.: Chemical structure of 2,2,4-trimethyl-1,2-dihydroquinoline (TMQ, top left), *N*-isopropyl-*N'*-phenyl-*p*-phenylenediamine (IPPD, top right) and stearic acid (bottom) used as additives in the compounds made by Prof. Leblanc.

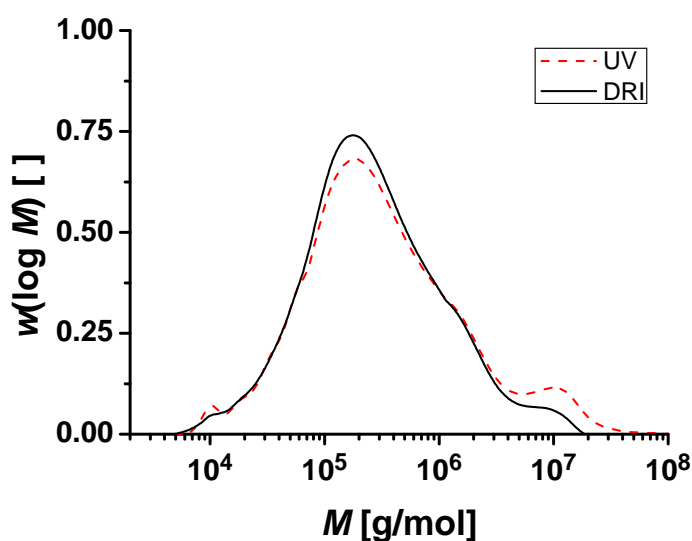


Figure B.13.: Molecular weight distribution of the raw E-SBR used as matrix polymer by Leblanc et al.. The data is calculated by a PS calibration (solvent: THF, DRI).

Due to the pronounced peak of chloroform in the aromatic region, the integral of the CHCl_3 was subtracted from the total integral of the aromatic region in order to estimate the styrene content. The E-SBR contains 17.3 mol% styrene, which corresponds to 28.7 wt%. The content of 1,4- polybutadiene is 69.5 mol% and of 1,2-polybutadiene 13.3 mol%. The integral of the aliphatic region is too high (81.80 instead of 27.8), which is probably due to different additives still present in the matrix. The polymer was received as black compound.

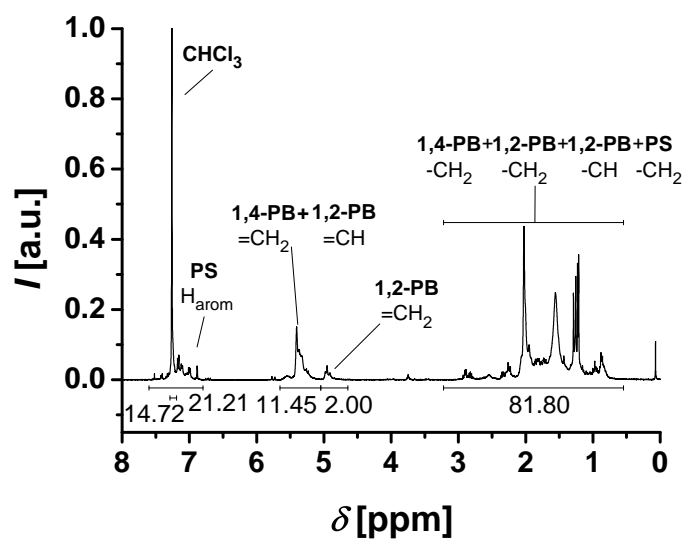


Figure B.14.: $^1\text{H-NMR}$ spectra of pure E-SBR (in deuterated chloroform at 400 MHz, 256 scans).

Publications

Publikationen

R. Figuli, L. Schwab, J. Lacayo-Pineda, H. Deckmann, M. Wilhelm, Combined Dielectric (DEA) and Dynamical Mechanical Thermal Analysis (DMTA) in Compression Mode, *KGK Kautsch. Gummi Kunstst.* **2016**, 69.

L. Schwab, N. Hojdis, J. Lacayo-Pineda, M. Wilhelm, Fourier–Transform Rheology of Unvulcanized, Carbon Black Filled Styrene Butadiene Rubber, *Macromol. Mater. Eng.* **2016**, accepted.

L. Schwab, N. Hojdis, J. Lacayo-Pineda, M. Wilhelm, Untersuchung der nichtlinearen mechanischen Eigenschaften von unvulkanisiertem, rußgefülltem SBR mit Hilfe von Fourier-Transformations Rheologie, to be submitted to *GAK, Gummi, Fasern, Kunstst.* **2016**.

Konferenzbesuche

- AERC2014 L. Schwab, J. L. Leblanc, M. Wilhelm, *Nonlinear Behavior of Heterogeneous Elastomer Samples Investigated by Means of Fourier-Transform Rheology*, Annual European Rheology Conference **2014**, Karlsruhe.
- BPG2015 L. Schwab, J. L. Leblanc, M. Wilhelm, *Fourier-Transform-Rheology of Unvulcanized, Carbon Black Filled SBR*, Annual Meeting of the Belgian Polymer Group **2015**, Houffalize, Belgien.
- DKT2015 L. Schwab, N. Hojdis, J. Lacayo-Pineda, M. Wilhelm, *Investigation of Non-linear Properties of Unvulcanized, Carbon Black Filled SBR by Means of Fourier-Transform Rheology*, Deutsche Kautschuk Tagung, **2015**, Nürnberg.
- IEC2015 L. Schwab, M. Wilhelm, *Fourier-Transform Rheology of Complex, Heterogeneous Rubber Materials*, International Elastomer Conference, **2015**, Cleveland, OH.